A PHASE PORTRAIT APPROACH TO VEHICLE STABILIZATION AND ENVELOPE CONTROL

A DISSERTATION
SUBMITTED TO THE DEPARTMENT OF MECHANICAL ENGINEERING
AND THE COMMITTEE ON GRADUATE STUDIES
OF STANFORD UNIVERSITY
IN PARTIAL FULFILLMENT OF THE REQUIREMENTS
FOR THE DEGREE OF
DOCTOR OF PHILOSOPHY

Carrie G. Bobier

August 2012

I certify that I have read this dissertation and that, in my opinion, it is fully adequate in scope and quality as a dissertation for the degree of Doctor of Philosophy.

(J. Christian Gerdes) Principal Adviser

I certify that I have read this dissertation and that, in my opinion, it is fully adequate in scope and quality as a dissertation for the degree of Doctor of Philosophy.

(Stephen M. Rock)

I certify that I have read this dissertation and that, in my opinion, it is fully adequate in scope and quality as a dissertation for the degree of Doctor of Philosophy.

(Mark R. Cutkosky)

Approved for the University Committee on Graduate Studies

This dissertation is dedicated to my family and my labmates.

Abstract

Loss of control accidents, which lead to thousands of deaths every year in America alone, are often caused by a miscalculated action of the driver or a sudden change in the road surface. Recent years have seen several technologies arise in an attempt to decrease accident rates, one of which is Electronic Stability Control. While ESC is effective at stabilizing the vehicle, it functions without full knowledge of the vehicle states or tire-road coefficient of friction. As more sensors become available and control objectives become more complicated, car designers will need to implement a more holistic control scheme like aircraft envelope control, which integrates multiple sensors and actuators to keep the vehicle within a safe operating regime.

This dissertation outlines two initial building blocks for a full vehicle control system. The first, called Vehicle Envelope Control, stabilizes the car by keeping it within a safe region of the yaw rate-sideslip state space. An analysis of the yaw acceleration isoclines in the yaw rate-sideslip phase plane allows for determination of an envelope boundary that is consistent with the natural system dynamics. The chosen boundary is defined by the yaw acceleration nullcline at the maximum steering angle that results in open loop stable dynamics, and the lines of maximum rear slip angle, which prevent rear tire saturation. The envelope boundaries are enforced by an attractive controller defined by the distance of the vehicle states from the safe boundary. An inner boundary proportional controller provides a soft landing at the yaw rate boundaries by limiting the driver's steering angle to the maximum stable steering angle as the vehicle approaches the boundary. To prove the effectiveness of the controller, Stanford's steer-by-wire vehicle, P1, performs several maneuvers during which the controller must activate to stabilize the car.

The second building block for the full-vehicle control system involves determining and implementing the mechanical changes necessary to enhance estimation of tire-road coefficient of friction and peak lateral tire force. The ability to estimate friction reliably allows for real-time updates to the envelope boundaries, relaxing them as the friction increases, and constraining them as the friction decreases. Isolating the aligning moment, the portion of steer-axis reaction torque from lateral tire forces, gives information on friction; however, there are typically several other torques felt about the steering axis that must be estimated and subtracted out before the aligning moment can be determined. The suggested suspension design eliminates contributions from these other torques, so that the aligning moment is measured directly.

Acknowledgements

After spending ten years at Stanford, so many people have contributed to my success on the road to obtaining a doctorate. Starting as an undergraduate, I was lucky to get to know my advisor, Chris Gerdes, while investigating steering system designs for the Stanford solar car. He was generous enough to let me work in the Dynamic Design Lab starting my junior year, and has been a committed advisor through all three of my degrees. Under his guidance I have gained confidence, and learned an immeasurable amount about vehicles, controls, and life in general. His enthusiasm is infectious, and has made my time in the DDL so exciting that it will be hard to leave the lab behind.

I would also like to thank the members of my defense committee. Professor Marco Pavone graciously accepted the position as chair of my committee. Sven Beiker has been a constant source of advice throughout my time at Stanford, and more recently has been a great asset as the Executive Director at the Center for Automotive Research at Stanford by managing the space where we keep our test vehicles. Steve Rock was the professor who taught my first classes in classical control, which helped convinced me to continue on to the Ph.D. program as a means to enhance my background in controls. Finally, although I never had classes with Mark Cutkosky, I did have a lot of interaction with his lab next door to the DDL. I have to give a special thanks to Professors Rock and Cutkosky as members of my reading committee; their comments have been invaluable.

My time at Stanford would not be as enjoyable without the members of the DDL. My labmates have been incredibly smart and hard-working, with older students always ready to lend a hand to the younger lab members. I probably asked Shad Laws, Chris Gadda, Josh Switkes, Judy Hsu, Nihkil Ravi, Matt Roelle, and Kirstin Talvala thousands of questions over the years. Shad was especially valuable to me as a mentor during my undergraduate work on P1's suspension. Greg Shaver has been a great source of advice on life after graduation, and is always ready to socialize when we meet up at conferences. The lab members closest in class year to me – Craig Beal, Adam Jungkunz, Hsien Hsin Liao, Rami Hindiyeh, Mick Kritayakirana, Holly Butterfield, and Hyungchai Park – have contributed to so many fun memories, late nights of homework problem solving, and unrivaled camaraderie. Craig in particular has been a constant companion, throughout the years of designing and building X1, and up through the testing of our controllers on P1. The rest of the X1 team, which has included so many amazing people over the years (Preston, Jon, Dave, Allegra, Aaron, and Ross especially), hold a special place in my heart. To the younger members of the DDL, thank you for providing new spunk to the lab, and remember to be great mentors as you become senior members in turn.

Craig Milroy and Sheri Sheppard have also been great advisors over the years. Craig oversaw all of the mechanical design work on X1, and contributed greatly to the improvement of my machining and design skills. He is always willing to provide advice, and has more knowledge about building things than anyone else I have worked with. Sheri was not only my undergraduate advisor at Stanford, but has been a great role model as the organizer of the Mechanical Engineering Women's Group. Sheri has helped me gain insight into myself and what I want from life.

My experience at Stanford would have been much more difficult if not for the efforts of Jennifer Rahn and Denise Curti, our lab admins. Their patience in fulfilling reimbursements, ordering car parts, and planning conferences is insurmountable.

Without the support from my sponsors at NISSAN MOTOR Co., Ltd. my doctoral research may have been quite different. I would like to especially thank Yoshitaka Deguchi, Takuro Matsuda, Shinichiro Joe, and Susumu Fujita for their interest in envelope control and the completion of X1. Shinichiro was kind enough to show me around Tokyo and the Nissan research center near Yokohama, which was a special treat. The Ford Foundation was also instrumental in the initial design and development of X1.

Although I did not get to study abroad as an undergraduate, I was able to spend one quarter in China during my Ph.D.. I made a lifelong friend in Ruina Dang, my exchange partner. We spent a lot of time working together, but also spent so many days sightseeing in San Francisco and Beijing. She was indispensable as a tour guide for Beijing, Tsinghua University, and Chinese daily life. The other students in her lab were nothing but kind, and very excited to help me practice speaking Mandarin while they practiced speaking English. I must also extend thanks to Professor Li Keqiang, who allowed me to visit his lab for three months, and made sure I was comfortable in the cold Beijing winter.

Finally, I want to thank my family and friends who have so patiently waited for me to finally graduate and leave Stanford for the next stage of my career. I could not have succeeded without the support of my mom, who always told me I could accomplish my goals, no matter how difficult. I hope that I have also paved the way for my younger sisters, so they can see their own possibilities. My new husband, Roger, has also been a great source of support for the nearly eight years of our relationship. Whenever my research or classes became too difficult, he was there to remind me that I could solve the problem. All of the hard work that goes into a doctorate degree would have been significantly more challenging without his encouragement.

Contents

List of Tables

List of Figures

Chapter 1

Introduction

1.1 Motivation

To Americans, the automobile represents freedom and fulfillment of the American dream. Eight of ten people in the United States owned registered automobiles as of 2008, compared to only six of ten in Germany and Japan [15]. The infrastructure of cities and highways in the United States has been dictated by the success of the automobile, so much so that rail travel has become dwarfed in comparison to other nations; in 2008, only 10 billion passenger-km were traveled by rail in the USA, compared to 256 billion in Japan. In contrast, 8 trillion passenger-km were traveled by road vehicles in the USA during 2007 [14].

The ubiquity of the automobile in America, and its presence throughout the rest of the world, does not come without a price. In 2009 alone, 33,808 people died from motor vehicle accidents in the United States. Furthermore, nearly 1% of the American population was injured in a vehicle crash during 2009, and almost 4 million accidents resulted in property damage [38]. These crashes are often caused by a miscalculated action of the driver or a sudden and unexpected change in road conditions. The average driver, while having a good mental model of vehicle dynamics under normal operating conditions, has difficulty controlling vehicles at the limits of handling [51]. This is especially true for unknown environmental conditions, where a sudden change in friction or a collision avoidance maneuver may initiate an unexpected, unstable vehicle response; the average driver will not be able to recover control.

As staggering as these fatality statistics may seem, the newest automotive developments have begun to decrease the number of accidents in the United States. Technologies such as Antilock Braking Systems (ABS), Electronic Stability Control (ESC), and Traction Control Systems (TCS) utilize drive and braking torques to prevent loss of grip between the tires and the road. These technologies correct driver errors while improving the handling of the vehicle. While ABS has become ubiquitous in modern vehicles, ESC and TCS systems are only recently gaining momentum. The National Highway Traffic Safety Administration (NHTSA) has found that Electronic Stability Control systems already reduce single vehicle car crashes by 36%, fatal rollover crashes by 70%, and fatal multi-vehicle crashes by 19%, as of 2007 [13]. These favorable results have led to the requirement that all new 2012 model year vehicles must be equipped with an ESC system [1].

In order to further reduce the number of fatalities and injuries caused by vehicle accidents, new sensing capabilities must be introduced to gain a more complete view of the vehicle dynamics and the surrounding environment. An ideal, full vehicle control system would have knowledge of the vehicle states, the position of the vehicle on the road and in respect to any obstacles, the nature of the tire-road interface at each wheel, and the driver's intention. Current sensing capabilities account for some of the quantities in each of these categories, but not enough of any category to give a full picture of the vehicle's motion through the environment. The combination of data currently available gives good information on the longitudinal dynamics of the car and on driver intent, but does not give a full picture of the lateral dynamics, tire forces, and the environment. Accurate and cheap estimates of these desired quantities are not available in passenger cars today; however, recent work has shown that the quantities of sideslip and peak tire force can be obtained in real-time using electric power steering torque measurements [28].

As solutions for these sensing problems become mainstream, the best safety performance will be gained by redesigning the car to be mechanically and computationally compatible with an overarching and expandable control scheme. Aircraft, for example, utilize a holistic control approach that integrates multiple sensors and actuators to keep the aircraft within a safe operating regime or envelope [56]. Using aircraft as a model, envelope control can be extended to automotive systems, resulting in easily expandable, non-intrusive controllers. For example, vehicle stability can be ensured by limiting the vehicle's motion states to a portion of the state space; this framework is then easily extended to environmental envelope control, where the vehicle stays within a lane boundary and away from cliffs, or tire envelope control, which limits the longitudinal and lateral force development at each wheel. These control structures may further benefit from a mechanical redesign of portions of the car to enhance the functionality of new sensors and actuators. This dissertation introduces two preliminary building blocks of a vehicle designed for control: the planar stabilization of the vehicle using Vehicle Envelope Control, and the mechanical changes necessary to enhance estimation of tire-road coefficient of friction and peak lateral tire force.

1.2 The Need for Vehicle Stabilization

Understanding the vehicle's limitations is the key to implementing Vehicle Envelope Control, which should allow the driver to push up to, but not past the limits. In a dynamic sense, the vehicle is limited by the availability of force at each tire. Tire force is produced in one of two ways: longitudinal tire force is caused by braking or accelerating the vehicle, and lateral tire force is generated during cornering (steering). The vehicle responds to changes in tire force through the dynamics of the vehicle states. The planar stability of the vehicle is captured well by two states: yaw rate r, the angular velocity about the vehicle's vertical (z) axis, and sideslip β, the difference in angle between the vehicle heading and velocity V. These states and axes are illustrated in Figure 1.1.

When the combination of lateral and longitudinal forces on the front wheels exceeds the maximum available force, the resulting inability to produce more force is known as limit understeer. In a limit understeering situation, the vehicle can no longer track the driver's steering command as it increases, and will follow a path of larger radius than the driver intends. Conversely, saturation of force on the rear tires leads to limit oversteer. A vehicle in limit oversteer turns more than the driver

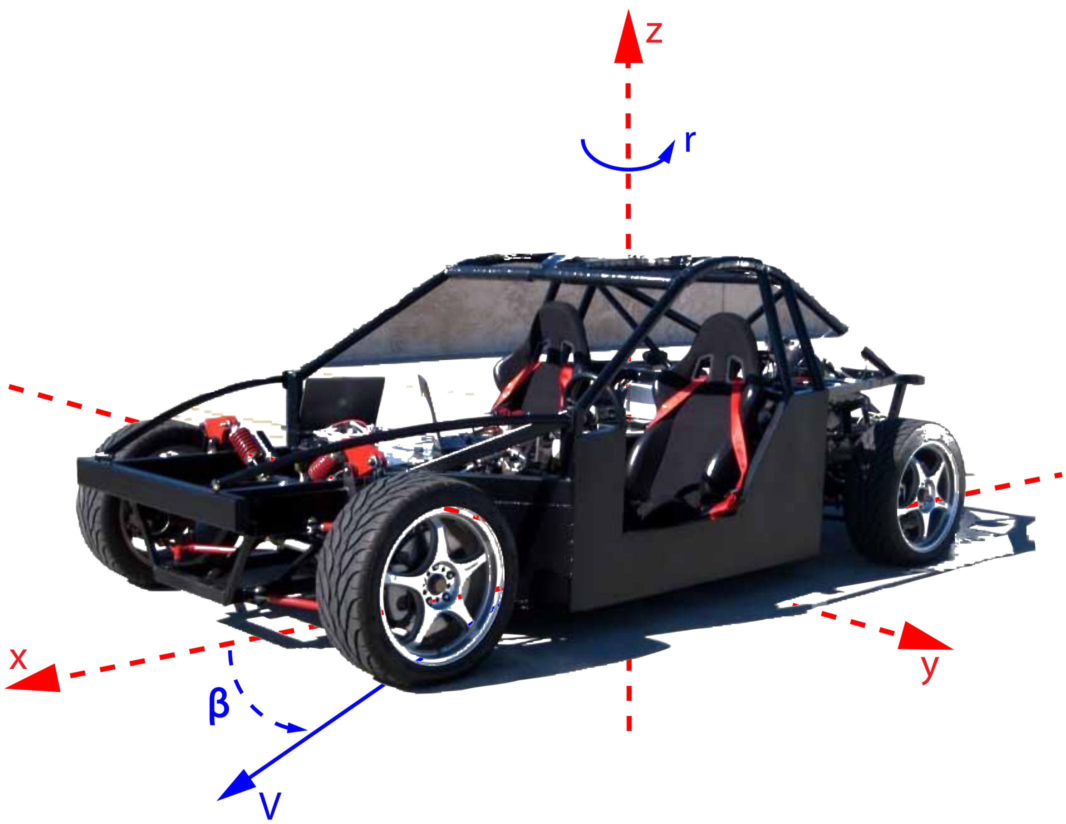

Figure 1.1: *An Overview of the Planar Vehicle States and Axes*

intends, usually resulting in a spin.

Instability is related to, but not defined by, the saturation of rear tire force. When considering vehicle states of yaw rate and sideslip angle, instability can take two forms. At high steering angles (the value of which is defined by the vehicle speed and tire friction coefficient) the vehicle motion is defined by globally unstable dynamics, with state growth mostly limited to the sideslip angle. Smaller steering angles result in a region of stability for yaw rate and sideslip, with instability occurring at values of high yaw rate and high, oppositely-signed sideslip angles. These regions of instability are also regions of rear tire saturation; however, large regions of the state-space in which the rear tires are saturated remain stable. A well-implemented stabilization system should keep the vehicle in the stable regions of the state space, while also maintaining the traction of each wheel as necessary.

Another aspect of vehicle stability is its effect on the driver. Racecar drivers are known for their ability to perceive the limits of handling and to control the car just within those limits. In contrast, the average driver can typically predict vehicle behavior under normal, linear operating conditions, but is less successful at controlling the car near the limits. In the absence of stability control, the mismatch between the average driver's mental model and the behavior of the vehicle at the limits of handling can lead to situations in which the driver loses control.

1.3 A History of Vehicle Stabilization Systems

The first production vehicle stability control system was developed as a joint venture between Mercedes-Benz and Robert Bosch GmbH in the mid 1990's [51]. Bosch's Vehicle Dynamic Control (VDC) system, like other ESC systems in production today, is similar to the technology behind Antilock Braking Systems. ABS allows each wheel to release the brake electronically and individually, regulating the pressure in each brake cylinder to prevent the occurrence of wheel lockup. ABS, by retaining grip at each tire, decreases stopping distances on most surfaces and allows the driver to steer while braking heavily.

With the development of ABS came the realization that a system could not only monitor and limit the longitudinal slip at each wheel, but could also provide a controlled yaw moment – in addition to that produced by steering – by applying the brake on one wheel alone. While this trait is undesirable when trying to brake hard in a straight line, it is incredibly useful in influencing the yaw dynamics of the vehicle for stability. Current production stability systems have two main modes of operation. First, if the front tires begin to saturate and enter a limit understeer condition, the system will see that the yaw rate is lower than expected. In this case, the rear inside wheel should brake, providing a moment on the car that increases the yaw rate. On the other hand, if the rear tires begin to saturate (limit oversteer), the yaw rate will be higher than expected, and the system will apply a moment to decrease the yaw rate by braking the outside front wheel. Figure 1.2 illustrates these two scenarios. The act of braking also serves to decrease the speed of the vehicle, which is useful from a stability standpoint, but can be undesirable for performance. More recently, torque vectoring systems have been added to distribute drive torques to each wheel, improving the total system performance [35].

The original Bosch system, like many of the subsequent production systems, utilizes a small number of sensors to implement stability control. van Zanten et al. enumerated the quantities sensed by the Bosch VDC in 1996: the driver's steering angle, braking pressure, and requested engine torque, yaw rate, lateral acceleration, wheel speeds, and actual engine torque [52]. The fundamental nature of these signals to stability control has been echoed in the development of systems at other companies, such as Ford and BMW [49] [34]. Few subsequent additions have been made in production to this sensor suite due to the unavailability of affordable sensors for other desired quantities like sideslip angle or friction coefficient.

Research in the private and academic sectors on stability control has been vast over the past fifteen years. Manning and Crolla released a comprehensive review of sixty-eight leading papers on lateral stability control in 2007 [36]. Their survey carefully chose the most practical research studies, whose validated approaches proved the worth of their contributions. The research under their review is divided into three sections: yaw rate control, sideslip control, and combined yaw rate and sideslip control.

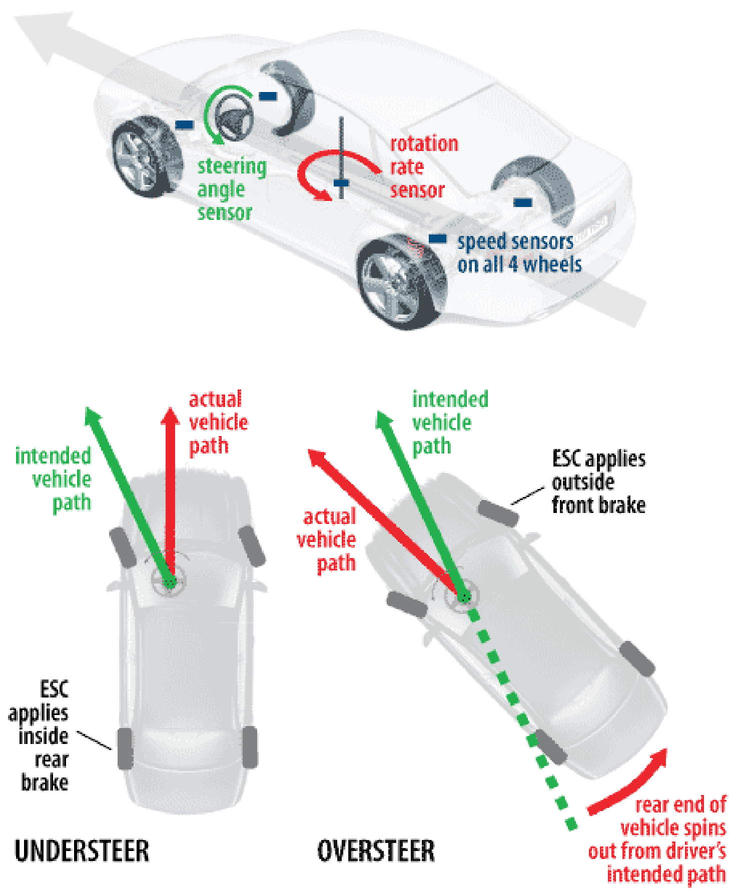

Figure 1.2: *Electronic Stability Control Functionality [19]*

Many of the research studies on yaw rate control utilize electronic steering as an input to influence the lateral dynamics during limit handling, mostly to prevent the reduction in speed that occurs during a production ESC's brake application. Kramer and Hackl's Active Front Steering (AFS) augments the driver's commanded steering angle to follow an ideal yaw rate from a 2DOF vehicle model [31]. Ackermann et al. use both AFS and Active Rear Steering (ARS) to decouple the yaw rate and lateral acceleration, resulting in a lateral acceleration profile that reflects the driver's steering command [3]. Several more recent studies, such as that of Benine-Neto et al., implement controllers to achieve improved limit handling by following similar, but more complex, strategies to track a desired yaw rate trajectory [8]. Manning and Crolla's critique of these controllers lies in their subjective claims to enhance the lateral performance under normal driving conditions as well as at the limits. Additionally, trajectory following at low lateral load requires more continuous control effort than intervention during limit maneuvers alone.

Sideslip controllers often attempt to minimize the sideslip entirely by following a model at steady state with zero sideslip [57, 46]; these controllers assume that the vehicle is always functioning in steady state, so dynamic maneuvers do not follow the model well. Improvements can be made by including information on both sideslip rate and sideslip in feedback, as shown in the phase plane work of Inagaki [29]. A large drawback to studies based on sideslip control has been the lack of an affordable method with which to measure or estimate sideslip angle accurately. Additionally, sideslip angle is more difficult to control than yaw rate: it is influenced only indirectly through the yaw dynamics for braking inputs, while the relationship between steering inputs and sideslip angle is non-minimum phase.

Systems of combined yaw rate and sideslip control offer the most comprehensive view of the lateral dynamics. They especially hold promise in the event that sideslip and friction estimation can be implemented well in production vehicles. Some controllers work under a cascaded scheme in which a sideslip error is identified and a target yaw rate is calculated to reduce it [61]; other controllers utilize multiple actuators (like four wheel steering) to control yaw rate and sideslip more independently [53, 22]. While several of the studies for combined control show promise, Manning and Crolla point out that most of them lack either experimental validation or in-depth theoretical analysis of the control algorithm. There is also little discussion of how to easily add additional actuators or control objectives (for example rollover control) in an integrated fashion. Increasing the functionality by adding new, separate controllers can lead to actuator fighting, lack of transparency, and ineffectiveness of the overall system. Even a well-integrated system can lack transparency if overcomplicated, or care is not taken to ensure the controller will act within the driver's expectations.

1.3.1 Vehicle Stabilization Using a Sliding Surface

In looking for a specific control technique for Vehicle Envelope Control, sliding surface control stands out as a well-known method in which the control algorithm places no restrictions on the complexity of the envelope shape. In past research, sliding control has been chosen for vehicle stabilization algorithms due to its robustness in the face of uncertainty in the tire dynamics. Several studies utilize sliding control to track a reference on either yaw rate or sideslip angle. For example, Abe et al. use sliding surface control to track a linear reference model in order to stabilize sideslip angle [2]. Abe's experimental results show an ability to stabilize the vehicle with this technique, but also highlight a difficulty in precisely tracking sideslip through steering inputs. Cho et al. use a linear bicycle model to track a desired yaw rate using sliding mode control to negate uncertainty in the tire dynamics; this is completed within a larger coordinated chassis control system [11].

Several studies exist that utilize sliding surfaces to track a combination of yaw rate and sideslip. In some cases, especially those using overactuated systems, each state is tracked separately. Wang and Longoria present successful simulations of a redundantly actuated vehicle with four wheel steering, braking, and drive, where a desired value for each state (yaw rate, lateral speed, and longitudinal speed) is tracked on a separate sliding surface [55]. The desired lateral speed is set to zero to minimize sideslip angle; however, the desired values for yaw rate and longitudinal speed are not stated. In the work of Yoshioka et al. of Mazda, the sliding surface for sideslip error is nested within a sliding surface controlling yaw rate error by defining the desired yaw rate in terms of the desired sideslip rate and the sideslip manifold value [61]. In Yoshioka's application, the controller is only activated when the state errors deviate past a threshold value, at which point the ABS system applies a calculated yaw moment. The simulations associated with the study show that the sliding mode application offers more robustness than PD control in the face of a changed yaw inertia, while experimental tests validate the controller's ability to stabilize different vehicles on varying surfaces.

Yoshioka's nested sliding surfaces are similar to another grouping of studies that utilize surfaces of combined yaw rate and sideslip errors. Hong et al. use sliding surface control to track a reference yaw rate (from a lookup table of the full vehicle model) and zero sideslip using the direct yaw moment method, where the sliding surface is a linear combination of the state errors [24]. This controller stabilizes a double-lane change maneuver under slippery road conditions with hardware-in-the-loop simulations, although the resulting states are oscillatory. Finally, Uematsu and Gerdes compare several sliding surfaces for stabilizing the vehicle: a linear combination of sideslip and sideslip rate; the error in yaw rate from nominal; a surface that minimizes sideslip; a surface that tracks yaw rate and minimizes sideslip [50]. Their simulation work suggests that the controllers using a sliding surface comprised of combined vehicle states stabilize the vehicle more successfully than those using only yaw rate or sideslip alone.

With the exception of Yoshioka's, the above-mentioned controllers are constantly controlling the vehicle along the sliding surface, even in circumstances when stability is not an issue. In many cases, the sideslip angle is controlled to zero at all times, which prevents instability but forces the car to operate differently, using a large amount of control authority for little gain when limiting the sideslip to small values would suffice. This type of constant state tracking is also susceptible to influence by deviations from the desired model in the instance of parameter and state uncertainty.

1.4 Envelope Control

The idea of an operating envelope, the basis of aircraft envelope control, is a concept that can be applied to a wide range of control problems. In aviation, this entails keeping the aircraft within a safe region of the state space through control, allowing the pilot to maneuver up to the safe limits without risking instability. A wide variety and number of limitations exist for different aircraft, including restrictions on angle of attack, pitch, bank angle, and speed [56]. In the aircraft industry, there are two competing envelope protection paradigms: Airbus designers chose to institute hard limitations on the aircraft's envelope, which the pilot is unable to override; Boeing, on the other hand, has given precedence to the pilot's judgment, and allows the pilot to circumvent the envelope protection by applying more force on the yoke [54, 39]. In both cases, the pilot is afforded uninhibited operation within the safe regime, and is only limited upon approaching and passing the edges of the safe envelope.

Using aircraft for inspiration, envelope control can also be applied to automotive systems. For example, vehicle stability can be ensured by limiting the vehicle's motion states to a safe portion of the state space. This framework is then easily extended to environmental vehicle control, which includes keeping the vehicle within a lane boundary or away from a cliff, and avoiding obstacles. Unlike aircraft, however, passenger cars must maintain low production costs, limiting the sensing capabilities and thus the control capabilities. For planar vehicle stabilization alone, measurements of speed, yaw rate, sideslip angle, and tire-road friction capacity are necessary to define a safe envelope for all operating regimes. Until recently, sideslip angle and friction coefficients have been difficult and expensive to estimate; however, work by Hsu has shown that the quantities of sideslip and peak tire force can be obtained in real-time using steer-by-wire or electric power steering torque measurements [26]. Because measurements of these quantities are increasingly possible to obtain, the stabilization of passenger vehicles through envelope control is now a reachable goal. Recent work in vehicle envelope control has endeavored to begin defining potential envelope characteristics and controller structures. The choice of stable envelope is not obvious, and can be defined by several quantities: state limits, tire friction limits, or equilibrium point locations, to name a few. The following sections detail examples that utilize different envelope paradigms.

1.4.1 Slip Angle Envelope

Controlling the individual tire forces to remain within their maximum theoretical limits can prevent each wheel from saturating and losing grip. In 2009, Hsu and Gerdes presented early work defining an envelope that limited the front and rear tire slip angles [27]. The envelope was enforced through steer-by-wire using a proportional-integral control law on slip angle as it exceeded a maximum value. The real value in this work is not the control algorithm, which is simple but effective, but the proof-of-concept of the accompanying friction estimation scheme. Additionally, limiting either slip angle without careful consideration of the implications can be too restrictive, eliminating regions of stable dynamics.

1.4.2 Vehicle States in the Phase Plane

Because vehicle lateral stability is well captured by a two-state model, the phase plane is an ideal visual medium through which to design an envelope. A phase portrait illustrates a system's dynamics graphically by plotting its states against one another. For example, if given two states, x and y, and their dynamic equations, every point in the $x - y$ plane of the phase portrait would indicate the direction and magnitude of the derivatives $\dot{x}$ and $\dot{y}$. A phase portrait reveals the location and type of equilibrium points, as well as regions of stability and instability; this is especially useful for nonlinear system analysis.

Previous vehicle work in the phase plane has focused on two sets of states: sideslip and sideslip rate, or sideslip and yaw rate. The stable region of the $\beta - \dot{\beta}$ state space has been explored by Inagaki et al. [29] and Hoffman et al. [23]. Inagaki's stability analysis incorporates these states due the nearly constant location of the equilibria on the $\dot{\beta} = 0$ line. Figure 1.3 shows the phase plane representation of the sideslip and sideslip rate dynamics at zero steering; the shaded regions indicate unstable dynamics, which lie outside the two saddle equilibria. The stable region changes with steering

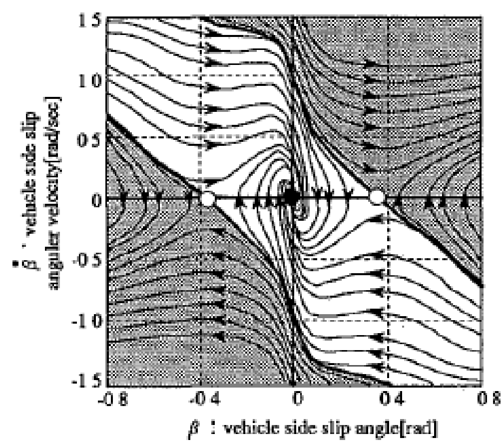

Figure 1.3: *Stable Region in the Sideslip-Sideslip Rate Phase Plane for Zero Degrees of Steering [29]*

angle, largely shifting along the sideslip rate axis. Inagaki utilizes this information to define a safe area of vehicle operation within the stable regions of the phase plane for use with a vehicle stabilization scheme. Hoffman uses the $\beta - \dot{\beta}$ plane to verify the stability and controllability criteria of the Milliken Moment Method.

While the sideslip and sideslip rate phase portraits are convenient in terms of equilibrium point location, neither state is typically measured in current production systems. Analyses that include yaw rate instead of sideslip rate are useful due to the ease of measurement and intuition regarding yaw rate. Yaw rate is also easier to influence with typical control actuators – brakes, traction, and steering – and is generally the first state to grow towards instability. Although the $\beta - r$ plane has not been discussed as often in the literature as the $\beta - \dot{\beta}$ plane, it has also been used to influence stabilization system design. For example, Ono et al. exploit the knowledge of a bifurcation in the $\beta - r$ equilibria to develop a controller that compensates for a growing nonlinearity in the tire force near the limits [41]. Ono's control scheme globally stabilizes the vehicle in the phase plane and in time domain simulations. Klomp utilizes $\beta - r$ phase plane analysis to analyze a stability margin based on yaw acceleration and sideslip rate for early indication of instability in Electronic Stability Control (ESC) systems [30].

Sideslip and Sideslip Rate Envelope

Although not explicitly called envelope control, several researchers make use of Inagaki's phase plane analysis of sideslip and sideslip rate in order to bound the vehicle motion within a strip of the phase plane. Yasui et al. implement a brake-based controller that intervenes as the vehicle exits the sideslip limits defined by Inagaki [59]. The vehicle states of sideslip and sideslip rate are estimated using the traditional production ESC sensor suite. The control algorithm is not discussed in any detail; however, experimental results suggest that the controller is able to stabilize the vehicle during a slalom test on pavement.

Smakman's integrated brake and wheel load (active suspension) controller also intervenes upon nearing Inagaki's defined stable limits [47, 48]. A PD control law calculates the required yaw moment to return the vehicle to the safe region, with inner-loop proportional control on the longitudinal wheel slip. The stable limits are defined only according to an analysis of the system at zero steer angle; the change in dynamics associated with other steering angles is ignored. His simulations suggest a stable response for several maneuvers, where the applied braking by the controller significantly decreases the speed of the vehicle (up to 50%) while attempting to maintain stability. No experimental data is provided.

He et al. present a variation on Smakman's controller [22]. Instead of braking, a Variable Torque Distribution controller applies a yaw moment to return the vehicle to Inagaki's stable limits. The yaw moment is determined by a simple proportional control law based on the distance of the current states to the boundary. This controller is integrated with an active front and rear steering system that tracks a desired yaw moment at low levels of demand. The simulation results for the controller are positive, and lack the speed decreases seen in Smakman's control scheme due to the difference in actuators. Again, however, no experimental data is provided.

The most advanced system designed in the sideslip-sideslip rate state space comes from Chung and Yi [12]. Their proposed safe area is closed, unlike Inagaki's boundaries. The corners of the envelope are defined by the positions of the saddle equilibria along the sideslip axis and two intersection points along the sideslip rate axis (these points are not mathematically defined in the paper). The boundary adapts to changes in steering angle and speed. Although the envelope boundary is defined by the sideslip and sideslip rate, the sliding mode control input is based on sideslip and the yaw rate error over the maximum steady state yaw rate. There is no analysis of the controller in the sideslip-yaw rate phase plane, so the repercussions of this mixture between boundary and control variables are unclear. The controller is tested using a virtual test track driving simulator, where the results show stability during a lane change maneuver; however, the yaw response seems to become quite oscillatory during the intervention.

Yaw Rate and Sideslip Envelope

In his 2011 work, Beal chooses a state based envelope that keeps the vehicle within the bounds of the maximum steady state yaw rate and maximum rear slip angle (cast in terms of sideslip). He introduces a mathematically complex control scheme utilizing the predictive capabilities of Model Predictive Control to foresee an impending boundary departure and correct the vehicle's trajectory preemptively using steer-by-wire [7, 6]. Beal's controller improves on Hsu's work by devising a proactive control scheme that provides a smooth vehicle response near the boundaries, and he successfully simplifies the problem enough to achieve real-time computation and control. However, using more complicated models or envelope boundaries under a Model Predictive Control scheme can become severely computationally intensive, and thus unable to run on modern automotive computers. This thesis presents a similar boundary to that of Beal, but augments the boundary in two ways: first, to more closely resemble the natural dynamics of the vehicle and thus feel less intrusive to the driver; second, to interface smoothly with a computationally simple control scheme.

1.5 Friction Estimation

One of the main difficulties for current stabilization systems is the lack of accurate road friction information. With the rise of Electric Power Steering and Active Steering in many of today's production vehicles, several estimation techniques have taken advantage of the data these systems provide. By measuring the current or torque from the EPS system, the overall steering torque and aligning moment (the portion from lateral forces on the tire) become available. Aligning moment gives an early indication that the vehicle is reaching the limits of handling by beginning to decrease when the tires reach approximately half of their force capacity, allowing for the identification of friction well before tire saturation. Yasui et al. use the EPS torque and current to estimate aligning moment for determining the Lateral Grip Margin, an indicator of tire saturation [58]. They then apply this information to vary the steering ratio, effectively restricting the driver's steering commands upon nearing the limits of handling. Friction values, however, are not directly estimated with this technique. More recent efforts utilize the aligning moment to obtain a direct estimate of friction or peak lateral tire force. Hsu, Laws, and Gerdes have developed a nonlinear observer to estimate slip angle, peak force, and friction coefficient from an estimate of pneumatic trail, the moment arm associated with aligning moment [28]. The estimator is validated experimentally on pavement and a variable friction gravel surface, and is confirmed to function well during periods of lateral excitation. Ahn, Peng, and Tseng have developed a similar robust nonlinear observer that utilizes aligning torque measurements (along with other readily available measurements like yaw rate and lateral acceleration) to estimate slip angle and friction coefficient. These estimates are combined with a longitudinal friction estimator in order to ensure high fidelity estimation during both lateral and longitudinal excitation [4, 5].

One of the early results for aligning moment based friction estimation accurately captures the difficulties in its measurement. In 1997, Pasterkamp and Pacejka trained a static MLP neural network to estimate friction and slip angles from measurements of longitudinal force, lateral force, and aligning moment using a combination of production and non-production sensors, such as load cells in the tierod and strain gauges at the kingpin axle [44]. They note that "the complex kinematics of the suspension mechanism complicate in particular the determination of the [aligning moment] from the measured signals." Even when using measurements from a standard EPS system, the aligning moment must be separated out from other contributing torques about the steering axis, including the torques from longitudinal and normal tire forces. Determining how the suspension kinematics change with steering angle (and ideally suspension travel) allows for the estimation and subtraction of the unneeded torque contributions; however, this subtraction can add uncertainty to the aligning torque measurement.

Laws et al. introduce a suspension and steering design concept to enhance the controllability and observability of the vehicle states [32]. The suspension geometry is designed in such a way as to physically negate the unwanted contributions to the measured steering torque from longitudinal and normal tire forces, resulting in a more direct measurement of aligning moment. Expanding upon the design for controllability suggested by Laws, this thesis proposes a suspension geometry that is ideal for use with lateral friction estimation. The suspension design fits within the paradigm of current production suspensions, choosing specific geometrical parameters from the typical ranges found in industry. A physical incarnation of the system proves that the geometry is feasible in terms of packaging and succeeds in eliminating the unwanted torque contributions. Additionally, the work presented in this thesis illustrates the desirability of a small, constant mechanical trail (in contrast to Laws' suggestion of a large trail to support the use of a lower actuator gain) to enhance the estimation of pneumatic trail and thus friction.

1.6 Thesis Contributions

This thesis builds upon the preceding work detailed in this chapter to make several contributions to the development of an integrated, symbiotic suspension and controller design for Vehicle Envelope Control. The work presented in this thesis serves as a foundation for the future development of multi-state envelope control schemes.

1.6.1 Defined a Stability Envelope Using Yaw Acceleration Isoclines

Choosing a state envelope within which to keep a vehicle is not straightforward; many envelopes can fulfill different requirements based on driver feel, dynamic response, or driver capability. This thesis presents a stability envelope that coincides well with the open loop yaw rate dynamics, given that a high yaw rate is the first indicator of impending instability. An envelope that complements the open loop dynamics leads to a softer landing on the boundary and better driver feel, while also allowing the vehicle to perform at its natural limits. The yaw acceleration nullcline, given at the maximum stable steering angle for a given speed and friction, results in a boundary that naturally follows the system dynamics in the yaw direction. The sideslip limits are defined by the maximum rear slip angle, in order to avoid rear tire saturation.

1.6.2 Developed a Computationally Simple Vehicle Envelope Controller for Planar Stabilization

The controller presented in this thesis is inspired by the stable surfaces found in Sliding Surface Control that are defined by linear combinations of the state errors. For the purposes of Envelope Control in this thesis, the control law is defined by the distance of the vehicle states from the closest point on the safe envelope, constraining the states to a first order dynamic system upon exiting the safe state boundaries. This setup allows for the development of arbitrary envelopes without restriction from the controller.

Even with carefully chosen boundaries, any difference between the open loop trajectory and that specified by the controller will be felt by the driver as the envelope control activates. In order to ensure a smooth landing at the yaw rate boundary, the addition of some control within the envelope is suggested. Because the sideslip boundaries are rarely reached first in practice, inner boundary control leading up to the yaw rate limits is sufficient. Ideally, the inner boundary control should have little effect on the driver's safe inputs, or on state trajectories well inside the boundaries. This thesis presents a simple proportional control law that activates as the yaw rate becomes large to smoothly reduce the driver's steering angle to the maximum stable steering angle at that speed. This addition greatly mitigates rough interventions from the envelope controller, and also compensates for delays in the actuators.

1.6.3 Designed and Built a Suspension to Isolate the Portion of Steer-axis Reaction Torque Related to Sensing the Tire Force Limits

Friction estimation is a difficult problem in vehicle control, but one that is necessary to solve for envelope control implementation. In order to make the estimation problem more tractable, this thesis presents a suspension design that isolates the measurement of aligning moment through clever geometry. By decreasing the kingpin angle and scrub radius to zero, the portions of steer-axis reaction torque caused by longitudinal and normal tire forces are nullified, leaving only the aligning moment from lateral tire forces. A constant and predictable mechanical trail, guaranteed by the zeroed kingpin angle, aids in the prediction of pneumatic trail from the aligning moment measurement. The suggested suspension geometry and parameters are not outside the conventional ranges seen in current production vehicles.

1.7 Dissertation Outline

Chapter 2: Vehicle Models and Testbeds

This chapter details the vehicle and tire models used throughout the thesis. The two-state bicycle model, which represents the lateral stability characteristics of the vehicle well, provides the basis for a dynamic analysis, as well as the envelope controller design. The Fiala tire model outlined by Pacejka captures the nonlinear vehicle behavior at the limits of handling [42]. Chapter 2 also introduces the steer-by-wire test vehicles, P1 and X1, which perform all of the presented experimental tests.

Chapter 3: Open Loop Vehicle Dynamics

The foundation of vehicle envelope control rests on a thorough understanding of the open loop vehicle dynamics and stability characteristics. Chapter 3 presents a detailed analysis of the yaw rate and sideslip dynamics in the phase plane. The phase plane provides a convenient medium through which to easily visualize the dynamics as they change with steering, friction, and speed. Additionally, the importance of the yaw acceleration isoclines is explored in relation to the movement of equilibria in the phase plane. The position of the isoclines influences the chosen boundary for envelope control in Chapter 4. Lastly, Chapter 3 illustrates the available trajectories in the phase plane given a specified control input (steering or braking).

Chapter 4: Vehicle Envelope Control

Chapter 4 describes the process of designing an envelope that resonates with an attractive envelope control scheme. Due to its coincidence with the open loop dynamics, the yaw acceleration nullcline associated with the maximum stable steering angle bounds the yaw rate. The sideslip limits are defined by the maximum rear slip angle in order to avoid rear tire saturation. A soft landing at the boundary is insured with an inner-boundary proportional control law that limits the steering angle to the maximum angle resulting in open loop stable dynamics. Finally, the complete envelope control design is experimentally verified on the P1 testbed.

Chapter 5: Suspension Design for Chassis Control

While tire-road friction is a difficult quantity to estimate, it is essential for the development of envelope control and related chassis control systems. Chapter 5 gives insight into the suspension design process, detailing how specific choices regarding suspension geometry can influence the measurement of aligning moment and the estimation of friction through the elimination of bump steer, scrub radius torque, and jacking torque.

Chapter 6: Conclusion

The work in this thesis leads to a variety of possible future studies. Expansion of the safe driving envelope to include other quantities, like the position of the vehicle in the environment and in relation to other objects, would further increase the performance and awareness of the total vehicle safety system. Likewise, considering the effects of additional actuators to the system, like controllable braking, could increase the controller's adaptability in various driving scenarios. Finally, it will be important to consider effective ways in which to communicate the controller's actions to the driver, especially as the safety system becomes more complicated.

Chapter 2

Vehicle Models and Testbeds

2.1 Choosing an Appropriate Vehicle Model

Although control algorithms can be designed around an empirical model of the system with good results, the benefit to designing around a physical model is a heightened level of understanding and intuition in terms of the controller's effect on the system dynamics. An appropriate choice of model should simplify the dynamics to an extent that the critical modes are captured. Consequences of using an overly complex model include lack of physical intuition and increased computation time (this is especially relevant for real-time control systems). For the design of a vehicle stabilization system in particular, a useful model should be of a high enough fidelity to capture the motion of the vehicle related to lateral stability.

In the most general sense, a vehicle is capable of motion with six degrees of freedom: three translational components and three rotational components. The translational degrees of freedom are defined along the vehicle's longitudinal, lateral, and vertical axes. Pitch is rotation about the lateral axis, roll is rotation about the longitudinal axis, and yaw is rotation about the vertical axis. While the most complicated vehicle models contain tens of states that describe not only these six degrees of freedom of the vehicle body, but also states like individual wheel rotation, such complexity is often unnecessary.

Lateral vehicle stability considers the motion of the chassis in the ground plane,

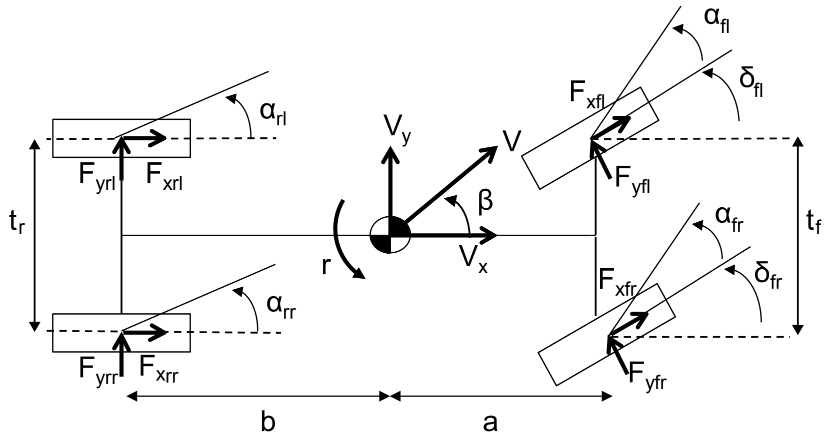

Figure 2.1: *The Planar Vehicle Model*

where instability manifests as the vehicle spinning. Because of the nature of this motion, the logical choice of model should capture the planar vehicle states, including the lateral and longitudinal velocities and the rotational speed about the vertical axis (known as the yaw rate). Inclusion of the roll dynamics, while important especially in considering the roll stability of the vehicle, is unnecessary to capture the general motion of the vehicle through the plane as long as the vehicle is well damped, or if steering inputs at frequencies close to the roll mode are avoided [10].

Figure 2.1 shows the relevant vehicle states and parameters for a planar model. The vehicle motion states consist of the yaw rate (r), longitudinal velocity (V_x), lateral velocity (V_y), and sideslip angle (β). The sideslip angle is the angle between the velocity and heading of the vehicle, given by Equation 2.1. Similarly, a slip angle (α) exists at each tire, denoting the difference in angle between the direction of the tire centerline and the tire velocity. The longitudinal forces acting on each tire are called F_{xii}, where ii denotes the specific wheel on which the force is acting; similarly, the lateral forces are F_{yii}. The vehicle size parameters are defined as the distance from the CG to the front axle a, distance from the CG to the rear axle b, and front and rear track widths t_f and t_r. The vehicle mass is m, and the yaw inertia is I_z.

$$\beta = \arctan \frac{V_y}{V_x} \tag{2.1}$$

Since sideslip and lateral velocity are related, the planar vehicle model results in three vehicle state equations for the yaw rate, sideslip, and longitudinal velocity, found by balancing the lateral forces, longitudinal forces, and moments about the vertical axis.

$$\begin{aligned}
I_z\dot{r} &= \frac{t_f}{2}(-F_{xfl}\cos(\delta_{fl}) + F_{xfr}\cos(\delta_{fr}) + F_{yfl}\sin(\delta_{fl}) - F_{yfr}\sin(\delta_{fr})) \\
&+ a(F_{xfl}\sin(\delta_{fl}) + F_{xfr}\sin(\delta_{fr}) + F_{yfl}\cos(\delta_{fl}) + F_{yfr}\cos(\delta_{fr})) \\
&+ \frac{t_r}{2}(-F_{xrl} + F_{xrr}) - b(F_{yrl} + F_{yrr}) \qquad (2.2a) \\
\dot{\beta} &= \frac{F_{yfl}\cos(\delta_{fl}) + F_{yfr}\cos(\delta_{fr}) + F_{xfl}\sin(\delta_{fl}) + F_{xfr}\sin(\delta_{fr}) + F_{yrl} + F_{yrr}}{mV_x} - r \qquad (2.2b) \\
\dot{V}_x &= \frac{F_{xfl}\cos(\delta_{fl}) + F_{xfr}\cos(\delta_{fr}) - F_{yfl}\sin(\delta_{fl}) - F_{yfr}\sin(\delta_{fr}) + F_{xrl} + F_{xrr}}{m} + rV_y \qquad (2.2c)
\end{aligned}$$

2.1.1 Planar Bicycle Model

Further simplifications to the planar vehicle model above can reduce the computational complexity of the model without substantially diminishing its accuracy. Under typical driving conditions, for example, the left and right tire slip angles are very similar. This fact allows the left and right tires on each axle to be modeled as one lumped tire, with one slip angle, one steering angle, and one set of forces acting on its center. This simplification gives the planar bicycle model its name. Lateral load transfer is generally ignored when using the bicycle model, because the effects of load transfer are captured in the experimentally determined tire parameters for each axle.

The maximum steering angles for the test vehicles in this thesis (and most production vehicles) are small enough to allow for small angle approximations. This allows the sideslip rate equation to be written without influence from longitudinal tire forces.

Lastly, reducing the order of the model by assuming a constant longitudinal velocity results in a two-state model, useful from the perspective of visualizing the

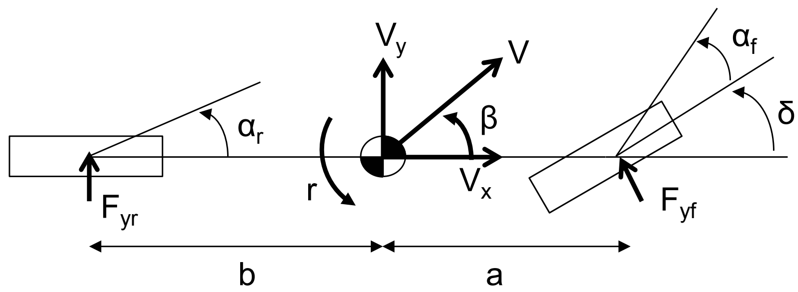

Figure 2.2: *The Planar Bicycle Model*

dynamics. The influence of braking and drive forces can be addressed in a simple manner – for example, by including a static weight transfer model, or limiting the lateral force capabilities based on the estimated longitudinal force.

The following differential equations define the bicycle model used throughout this thesis. Solving a moment balance around the vertical (z) axis of the vehicle results in an equation for the yaw rate; solving a force balance in the lateral direction results in the sideslip equation. Figure 2.2 illustrates the model; comparison with Figure 2.1 shows the simplifications between the full planar model and the simplified bicycle model.

$$\dot{r} = \frac{1}{I_z}(aF_{yf} - bF_{yr}) \tag{2.3a}$$

$$\dot{\beta} = \frac{1}{mV_x}(F_{yf} + F_{yr}) - r \tag{2.3b}$$

From kinematics, the slip angles of the front and rear tires are defined as follows:

$$\alpha_f = \arctan(\beta + \frac{ar}{V_x}) - \delta \tag{2.4}$$

$$\alpha_r = \arctan(\beta - \frac{br}{V_x}) \tag{2.5}$$

2.2 Tire Models

The models of vehicle motion described in the previous section are defined in terms of tire forces. The tire is the medium through which the environment and vehicle interact, so a representative tire model is arguably more important than a complicated vehicle model. This is especially true as the vehicle operates near the limits of handling, because nonlinearities in the vehicle dynamics arise from saturation of the tire force. Two main types of tire models exist today: empirically based models, which fit a tire curve (slip angle versus force) to experimental data; and physical models, which use physical parameters of the tire to generate a tire curve. The most common empirical model is called the Magic Tire Formula, developed by Hans Pacejka [43]. The Magic Tire Formula is capable of matching experimental data extremely well, but does not offer a physical explanation to the meaning of its empirical parameters. Finite element models, on the other hand, are physical models, typically representing complex vibration within the tire. FEA models are often too complicated for use in vehicle dynamics analysis; however, recent work by Gipser has striven to simplify finite element models for use with full-vehicle simulation software [21]. Finally, brush models commonly represent the tire as a rigid ring surrounded by a deformable brush. These models are generally simple, utilizing physically based parameters that convey information to the user; the Dugoff and Fiala models are common examples [17, 42]. This thesis utilizes a brush tire model due to its simplicity and physical basis.

The deformation of the tire contact patch in the lateral and longitudinal directions results in the generation of tire force. When a lateral force (F_y) is applied to a tire, the resulting angle of deformation in the contact patch is called the tire slip angle, defined by the difference in angle between the longitudinal tire centerline and the velocity of the tire. At low values of slip angle, the lateral force is nearly linearly related to slip angle; however, the lateral force gradually saturates with increasing slip angle until reaching its maximum (see Figure 2.3). The saturation of tire force is due to a transition between gripping and sliding, illustrated in Figure 2.4. The distribution of weight through the contact patch is roughly parabolic, with the available force limited by friction. As the lateral force increases, the resultant point of force application

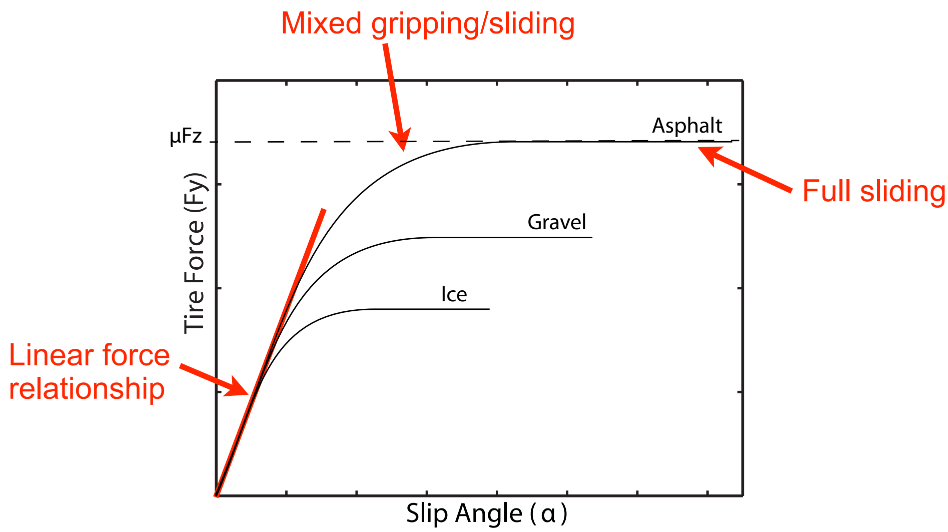

Figure 2.3: *Lateral Tire Curves for Various Driving Surfaces*

moves forward though the contact patch. The distance between the point of force application and the center of the contact patch is known as the pneumatic trail (t_p). The force is distributed linearly from the front of the contact patch towards the rear, with larger forces occurring at the the rear. As the force increases, the friction limit is reached at an earlier point on the contact patch, and the rear portion of the tire beyond this point is saturated and begins to slide. When the maximum force is reached, the tire is completely saturated and sliding, and the pneumatic trail is zero.

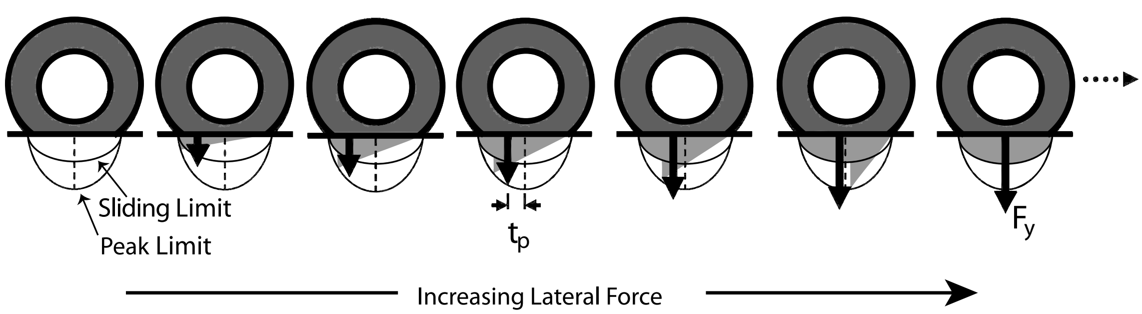

Figure 2.4: *The Evolution of Lateral Force Against the Friction Limit*

Longitudinal slip is a relation between the longitudinal velocity of the vehicle (V_x) and that of the individual wheel, given by Equation 2.6, where R is the radius of the tire, and ω is the rotational velocity of the wheel. Braking results in a positive value of slip, with wheel lockup occurring at a slip value of negative one. The tire curve for slip versus longitudinal force is the same shape as that of lateral force versus slip angle.

$$\kappa = \frac{R\omega - V_x}{V_x} \tag{2.6}$$

The amount of force available to each tire (F_{max}) is defined by the value of the tire-road peak coefficient of friction (μ), the sliding friction of the driving surface (μ_s), and the normal force on the tire (F_z); however, when the tire is completely saturated, the total force is limited to $F_{max,slide}$:

$$q_\mu = \left(1 - \frac{2\mu_s}{3\mu}\right)^{-1} \tag{2.7}$$

$$F_{max} = \mu F_z \left(-q_\mu + \frac{q_\mu^2}{3}\left(2 - \frac{\mu_s}{\mu}\right) - \frac{q_\mu^3}{9}\left(1 - \frac{2\mu_s}{3\mu}\right)\right) \tag{2.8}$$

$$F_{max,slide} = \mu_s F_z \tag{2.9}$$

2.2.1 The Linear Tire Model

The simplest tire model used in vehicle dynamics assumes a linear relationship between the tire's slip angle and its lateral force, given by Equation 2.11, where the cornering stiffness of the tire (a measure of the tire's ability to resist deformation) is denoted by C_α. This model is capable of successfully capturing the vehicle dynamics for maneuvers in the linear region of handling, where the contact patch is still largely unsaturated.

$$F_y = -C_\alpha \alpha \tag{2.10}$$

A similar model describing the relation between slip and longitudinal force can be used for modeling cases with heavy braking or drive inputs; in this case, the longitudinal tire stiffness is denoted by C_x.

$$F_x = C_x \frac{\kappa}{1+\kappa} \tag{2.11}$$

Because issues of vehicle stability are relevant only as the tires saturate, the linear tire model is not appropriate for the topics discussed in this thesis, and is not used unless specifically noted.

2.2.2 The Lateral Brush Tire Model

The linear tire model captures the development of tire force at low levels of slip angle, but in reality the tire force gradually saturates with increasing slip angle. To reliably calculate the relation between slip angle and lateral force as the tire saturates, a more complicated model is necessary. The family of brush tire models describes the tire as a rigid carcass, with small, deformable brush elements connecting the carcass to the road. This thesis uses a variant of the Fiala nonlinear brush tire model, assuming a parabolic force distribution, as laid out by Pacejka [42]. For this analysis, F_z is the normal force for a given tire, α_{sl} is the slip angle corresponding to peak tire force, δ is the steering angle, g is the gravitational constant, μ is the estimated peak friction of the driving surface, and μ_s is the estimated sliding friction:

$$F_{zf} = \frac{mgb}{(a+b)} \tag{2.12}$$

$$F_{zr} = \frac{mga}{(a+b)} \tag{2.13}$$

$$F_y = \begin{cases} -C_\alpha \tan\alpha + \frac{C_\alpha^2}{3\mu F_z}(2 - \frac{\mu_s}{\mu}) \mid \tan\alpha \mid \tan\alpha - \frac{C_\alpha^3}{27\mu^2 F_z^2}\tan^3\alpha(1 - \frac{2\mu_s}{3\mu}) & |\alpha| < \alpha_{sl} \\ -\mu_s F_z \mathrm{sgn}\ \alpha & |\alpha| \geq \alpha_{sl} \end{cases} \tag{2.14}$$

$$\alpha_{sl} = \arctan\frac{3\mu F_z}{C_\alpha} \tag{2.15}$$

The work in this thesis assumes that the peak and sliding coefficients of friction are equal for simplicity. The experiments in this thesis are driven on a gravel surface, on which the two friction coefficients are similar enough to be within the noise levels of the measured data.

Except where noted, in this thesis the longitudinal tire forces are taken into account during experiments through a mapping of accelerator pedal angle to rear wheel torque (there is no measurement of the force from the mechanical brakes). With an estimate of the longitudinal tire force on the rear axle (F_{xr}), the maximum available rear lateral force determines the peak of the lateral tire curve for the Fiala model:

$$F_{yr,max} = \sqrt{(\mu F_{zr})^2 - F_{xr}^2} \tag{2.16}$$

This maximum effectively derates the available lateral tire force when calculating the control input, so even though the longitudinal dynamics are not included in the model, the controller can still account for the loss of lateral capability during braking and drive.

2.2.3 The Coupled Force Brush Tire Model

In cases where it is necessary to include the effects of braking and drive force at a higher level of fidelity, a coupled force brush tire model is appropriate. In this model, the longitudinal and lateral forces are coupled, with overall tire force limited by μF_z. Sliding occurs when the combined values of lateral and longitudinal deformation exceed the available friction. The lateral and longitudinal components of the combined force are defined as follows:

$$f = \sqrt{C_x^2 \left(\frac{\kappa}{1+\kappa}\right)^2 + C_\alpha^2 \left(\frac{\tan\alpha}{1+\kappa}\right)^2} \tag{2.17}$$

$$F = \begin{cases} f - \frac{1}{3\mu F_z} f^2 + \frac{1}{27\mu^2 F_z^2} f^3 & f \le 3\mu F_z \\ \mu F_z & f > 3\mu F_z \end{cases} \tag{2.18}$$

$$F_x = \frac{C_x \kappa}{f(1+\kappa)} F \tag{2.19}$$

$$F_y = \frac{C_\alpha \tan\alpha}{(1+\kappa)} F \tag{2.20}$$

Coupling of the tire forces is illustrated graphically in Figure 2.5. Plot(a) shows the achievable lateral and longitudinal forces for constant values of lateral slip, Plot(b) shows the same for constant values of longitudinal slip, and Plot(c) shows the combination of the two. The friction circle denotes the limits of force generation for a tire: for combinations of lateral and longitudinal force that lie inside the circle, force is available; for those outside the circle, the tire is completely saturated. The positive longitudinal force is generally further limited by the capabilities of the car's engine.

2.3 P1 Test Vehicle

The Stanford P1 by-wire research vehicle, shown in Figure 2.6, is one of the Dynamic Design Laboratory's experimental testbeds. The vehicle is equipped with a dual-antenna Global Positioning System (GPS) and inertial sensors (INS), wheelspeed sensors, and load cell sensors at the steering tierods and toe links. The main control input on the vehicle is independent front wheel steer-by-wire, realized through two brushed servo motors attached to harmonic drives; the harmonic drives provide very high gear ratios (160 : 1) with almost no backlash. The front wheels can steer under computer control at frequencies of more than 8Hz, almost three times the bandwidth of a human driver. P1's steering system is described in detail by Laws and Gerdes [33]. Lastly, P1 is equipped with independent rear wheel electric drive and regenerative braking.

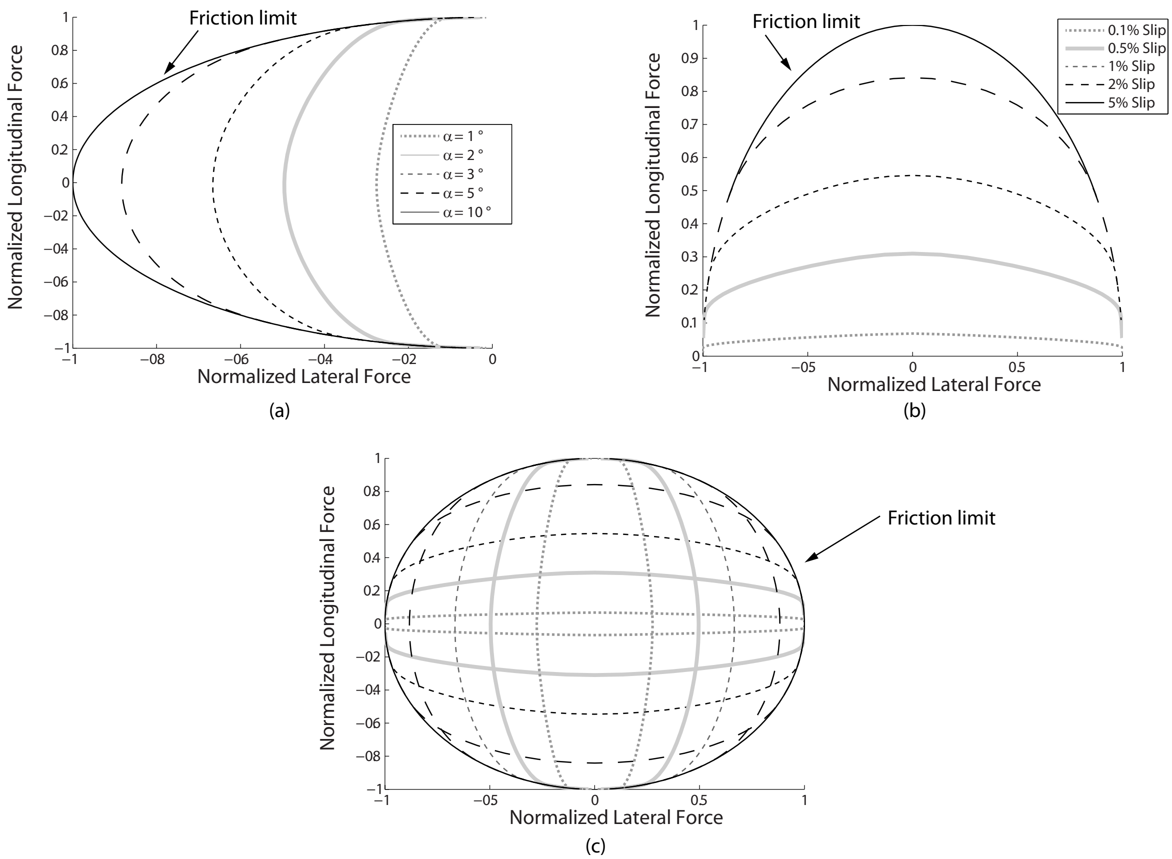

Figure 2.5: *Friction Circle Illustrating (a) Slip Angles, (b) Longitudinal Slip, and (c) Coupled Tire Forces*

Figure 2.6: *Stanford P1 Steer-by-Wire Research Testbed*

P1's xPC-based computer system receives and records sensor data at a 500Hz update rate. The vehicle states (yaw rate and sideslip angle), as well as the velocity and heading angle are obtained through sensor fusion. Bevly [9] and Rossetter [45] detail the integration of INS with dual-antenna GPS measurements of velocity and attitude to obtain a high fidelity estimate of sideslip angle.

Table 2.1 gives the relevant parameters for the vehicle. P1 has characteristics similar to a sports sedan, with the exception of a lower yaw moment of inertia.

Table 2.1: P1 Vehicle Parameters

Parameter		*P1*	
Mass	m	1725	kg
Yaw inertia	I_z	1300	kgm^2
Distance from CG to front axle	a	1.35	m
Distance from CG to rear axle	b	1.15	m
Front cornering stiffness	$C_{\alpha f}$	75	kN/rad
Rear cornering stiffness	$C_{\alpha r}$	135	kN/rad

Figure 2.7: *Stanford X1 Modular Research Testbed*

2.4 X1 Test Vehicle

X1, shown in Figure 2.7, is the Dynamic Design Laboratory's third generation steer-by-wire testbed. While X1 has the same sensor suite as P1, X1 is equipped with independent rear wheel steer-by-wire as well as independent front wheel steer-by-wire. X1's drive system consists of one electric motor that connects to both rear wheels through an open differential.

X1 features a modular chassis concept, developed so that the car is easily modifiable in a research setting. Mechanically, the front and rear sections of the vehicle are easily removed and replaced if a new combination of steering, suspension, and drive is desired. Currently, X1 uses a dSPACE MicroAutoBox as its main computer, recording data at a rate of 500Hz. This computer is responsible for chassis control, control of the steer-by-wire system, and sensor I/O.

Table 2.2 gives the relevant parameters for the vehicle. X1 and P1 have fairly similar weights and weight distribution (slightly rear biased), and both have very low yaw moments of inertia compared to typical passenger vehicles. Both vehicles lack large engines and body panels that add substantially to the yaw inertia. Furthermore, P1's batteries lie in a flat plane under the driver and passenger seats, and X1's batteries are positioned in a narrow row down the centerline of the car. Both battery configurations result in small yaw inertias. For the tests in this thesis, both cars also use the same brand and type of tires (Kumho Ecsta ASX), but in different sizes: X1 uses size 235/40R18 and P1 uses 225/50R16.

Table 2.2: X1 Vehicle Parameters

Parameter		*X1*	
Mass	m	1823	kg
Yaw inertia	I_z	2000	kgm^2
Distance from CG to front axle	a	1.54	m
Distance from CG to rear axle	b	1.21	m
Front cornering stiffness	$C_{\alpha f}$	115	kN/rad
Rear cornering stiffness	$C_{\alpha r}$	155	kN/rad

Chapter 3

Open Loop Vehicle Dynamics

3.1 The Vehicle in the Phase Plane

In order to determine an envelope for safe vehicle operation, it is necessary to understand the dynamics of the vehicle in the state space. For aircraft, the safe flight envelope is defined by limitations on the states; the same method can be applied here to road vehicles. The analysis in this chapter will show that vehicle stability characteristics are well captured with the two-state bicycle model, which accurately depicts nonlinear system properties like movement and bifurcation of the equilibria. Because of the low model order, it is convenient to use a phase plane analysis to better understand the yaw rate and sideslip dynamics. In understanding the dynamics–where the equilibria lie and how they change with varying inputs and speed–we can choose envelope boundaries that correspond to natural boundaries of the dynamics.

3.1.1 The Effect of Steering

The most dramatic changes in the phase portrait come from steering. Figure 3.1 shows the open loop $\beta - r$ dynamics of P1 at $10m/s$ and $\mu = 0.55$ for several steering angles. These plots use the planar bicycle model and lateral brush tire model to illustrate the dynamics for a vehicle that is neutral at the limits of handling (the same coefficient of friction is assumed at both axles). In the cases of $0°$, $5°$, and $10°$

of steering, there is one stable equilibrium point. In each of these cases, two saddle equilibria also exist; these points denote the yaw rate and sideslip angle that would arise from a right or left-handed drift sustained at the given steering angle. The saddle equilibria lie on the line of maximum steady state yaw rate, given by Equation 3.1. All combinations of yaw rate and sideslip, where the sideslip is larger in magnitude than the saddle equilibria sideslip, and the yaw rate lies above the maximum steady state yaw rate, result in open loop instability.

$$r_{max,ss} = \frac{\mu g}{V_x} \tag{3.1}$$

In the case of 15° of steering, a stable equilibrium point does not exist for the given vehicle parameters. One unstable equilibrium exists on the line of maximum steady state yaw rate. The unstable trajectories surrounding this equilibrium correspond to the vehicle spinning out. A saddle equilibrium also exists, which corresponds to a right-handed drift with a countersteer of 15°.

As the steer angle grows from 0° to 15°, the stable equilibrium moves from $(0, 0)$ towards the left-handed drift equilibrium until the two equilibria converge and a bifurcation occurs. This results in the unstable equilibrium that is seen at 15° of steering. The drift equilibria also move with the steering angle: in a left hand turn, the left-handed drift equilibrium will move towards zero sideslip; the right-handed drift equilibrium will move away from zero sideslip.

3.1.2 Changes with Speed and Friction

While steering causes the shape of the vehicle trajectories to change in the phase plane, variations in speed and friction result in qualitatively similar portraits for a given steering angle as long as a stable equilibrium exists. From Equation 3.1, it is apparent that the line of maximum steady state yaw rate increases with both increasing friction and decreasing speed; therefore, lower friction and higher speed more easily lead to instability due to a reduction in size of the stable region.

Figure 3.2 shows the phase portraits for P1 at 0° of steering, a friction coefficient of 0.55, and varying speeds. As the speed increases from 5m/s to 15m/s the positions

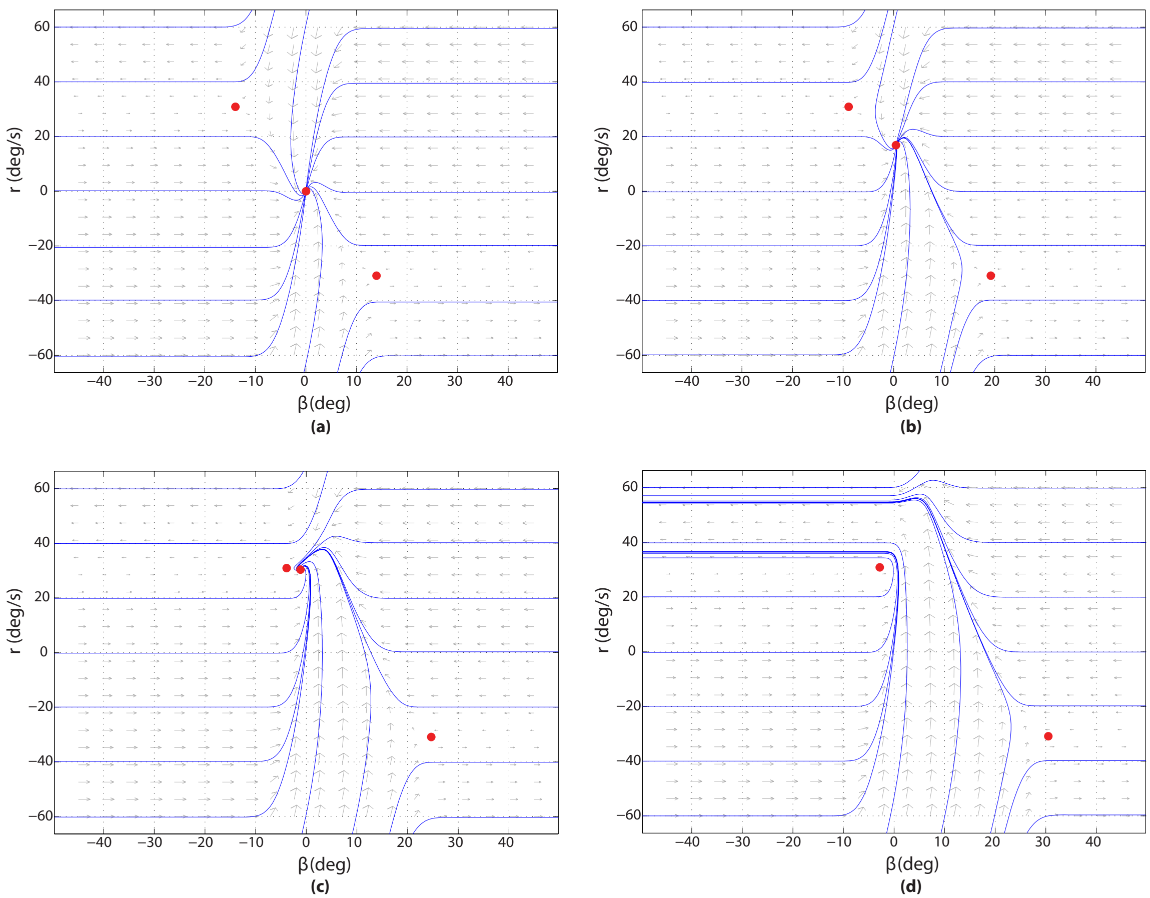

Figure 3.1: *Open Loop Dynamics at $\mu = 0.55$, $V = 10m/s$, and (a) 0° (b) 5° (c) 10° (d) 15° of Steering*

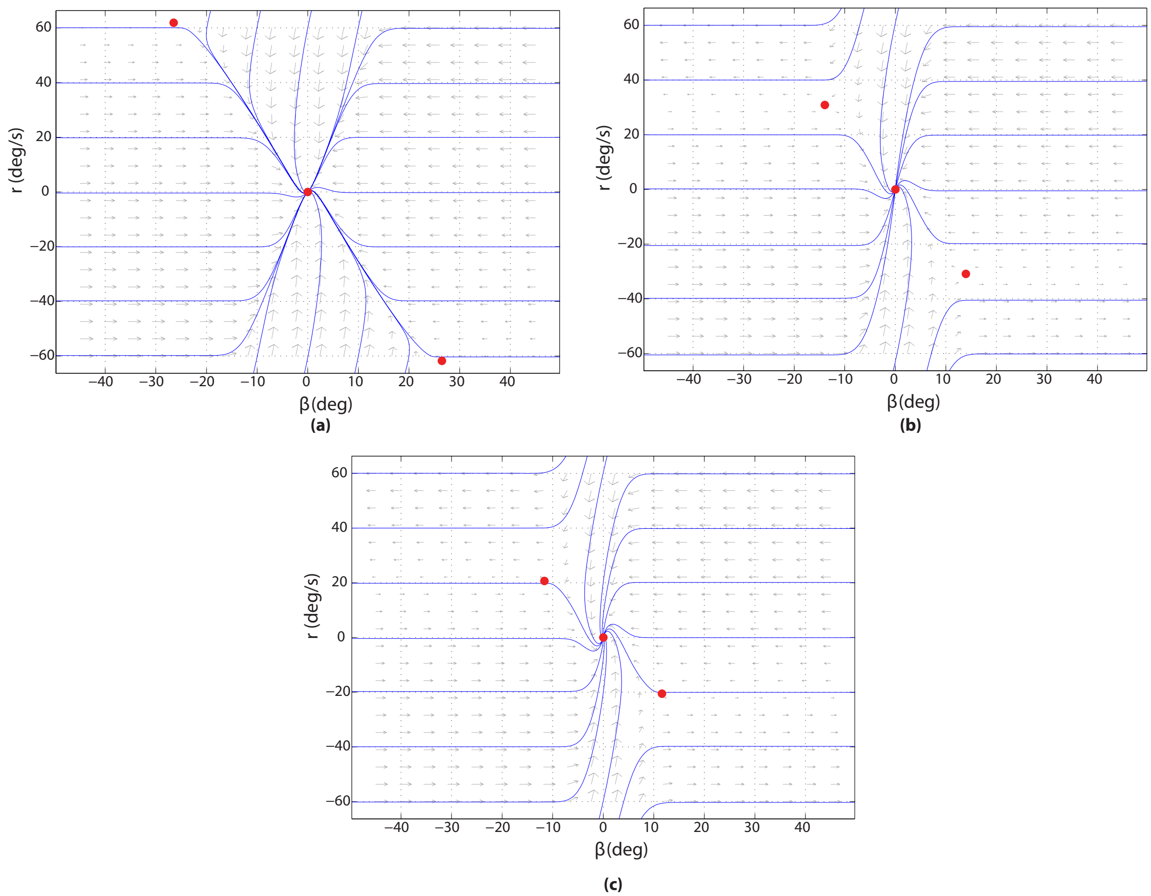

Figure 3.2: *Open Loop Dynamics at μ = 0.55, δ = 0°, and a Speed of (a) 5 m/s (b) 10 m/s (c) 15 m/s*

of the saddle equilibria change drastically due to the decreased maximum steady state yaw rate. At higher speeds, the steering angle at which the stable equilibrium bifurcates decreases.

Figure 3.3 shows the phase portraits for P1 at 0° of steering, a speed of 10m/s, and varying friction coefficients. As the friction increases from 0.45 to 0.65 the positions of the saddle equilibria change due to an increasing maximum steady state yaw rate. For higher friction coefficients, the steering angle at which the stable equilibrium bifurcates increases. These changes in equilibrium position as a result of changing friction motivate the desire for onboard friction estimation. Without knowledge of

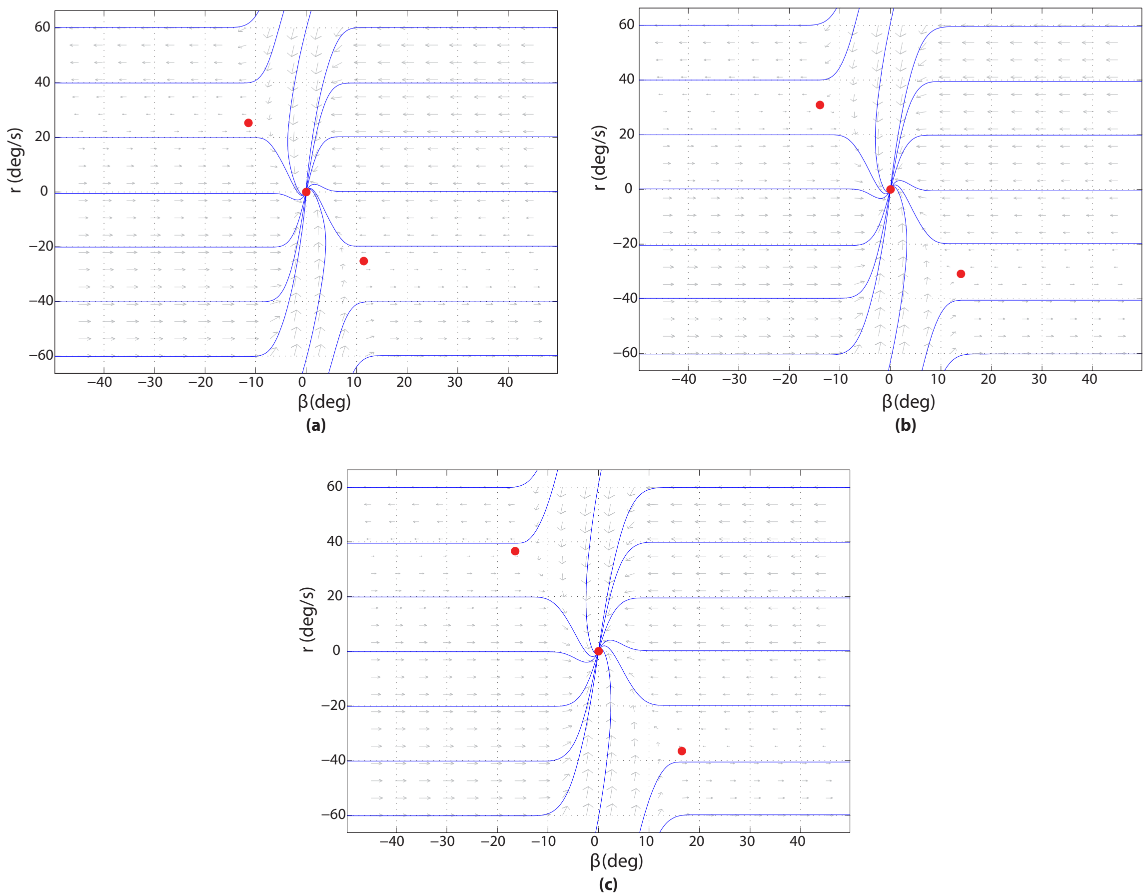

Figure 3.3: *Open Loop Dynamics at* $V = 10m/s$, δ=$0°$, *and (a)* $\mu = 0.45$ *(b)* $\mu = 0.55$ *(c)* $\mu = 0.65$

friction coefficient, the safe region of the phase plane is more difficult to determine precisely and early.

3.2 Isocline and Nullcline Geometry

3.2.1 The Yaw Acceleration Isoclines

The movement of the equilibria described in the previous section is determined by the $\dot{r}$ isocline geometry. The isoclines of a state derivative are defined as lines on a phase portrait where that state derivative is a constant value; nullclines are lines of value zero. Figure 3.4 shows the yaw acceleration isocline geometry for P1 at 10m/s, $\mu = 0.55$, and varying steer angle: the dotted lines in the figure denote several isoclines of yaw acceleration. Additionally, the horizontal black lines indicate the maximum/minimum steady state yaw rate; the positively sloped black lines are determined by the maximum/minimum rear slip angles; the negatively sloped black lines are determined by the maximum/minimum front slip angles. The relevant equations for these lines are as follows, where α_{sl} is the slip angle corresponding to peak tire force, given in Equation 2.15:

$$r_{max,ss} = \frac{\mu g}{V_x} \tag{3.2}$$

$$r_{min,ss} = -\frac{\mu g}{V_x} \tag{3.3}$$

$$\beta_{\alpha_f,max} = -\frac{ar}{V_x} + tan(\alpha_{sl,f} + \delta) \tag{3.4}$$

$$\beta_{\alpha_f,min} = -\frac{ar}{V_x} + tan(-\alpha_{sl,f} + \delta) \tag{3.5}$$

$$\beta_{\alpha_r,max} = \frac{br}{V_x} + tan(\alpha_{sl,r}) \tag{3.6}$$

$$\beta_{\alpha_r,min} = \frac{br}{V_x} - tan(\alpha_{sl,r}) \tag{3.7}$$

From the equations, it is apparent that for a given speed and friction coefficient, the only lines that move are those associated with the extreme front slip angles. These lines change with steering angle, which is evident in Figure 3.4 as steering increases from 0 up to 11 degrees. As the steering angle increases, the overall shape of the isoclines does not change, but their placement in the plane shifts towards values of higher sideslip and yaw rate. This shift is most noticeable by observing the line between points A and B (the intersections of the front and rear slip angle lines). The line between A and B is a linear approximation of the $\dot{r} = 0$ nullcline, and denotes the change from increasing to decreasing yaw rates. This nullcline intersects the origin when $\delta = 0$ and moves upwards and downwards with positive and negative steer angles.

The stable equilibrium, when it exists, is located along the $\dot{r} = 0$ nullcline, and thus moves through the phase plane with the nullcline as the vehicle steers. The isoclines are crowded near the stable equilibrium, suggesting that the change in yaw acceleration near the stable equilibrium is quite high. As the steering angle increases, the maximum yaw rate, rear slip angle, and front slip angle lines will eventually intersect, at which point the bifurcation from stability to instability occurs. This triple intersection is shown in Figure 3.4 Plot (d) at point A. The steering angle corresponding to the bifurcation is the maximum stable steering angle:

$$\delta_{max} = atan\left(\frac{(a+b)\mu g}{V_x^2} - tan(\alpha_{sl,r})\right) + \alpha_{sl,f} \tag{3.8}$$

The remaining saddle equilibria occur at the intersection of the r_{max} and the $\beta_{\alpha_f,min}$ line, and its opposite. These two intersections are marked by diamonds in Figure 3.4 Plots (a-c). A third diamond marks the stable equilibrium in these plots. For Figure 3.4 Plot (d), the dynamics are globally unstable, and only two equilibria exist.

The region of the phase plane where $\dot{r} = 0$ is not restricted to the approximate line between A and B, but also includes the areas outside the extreme front and rear slip lines. This region of front and rear tire saturation corresponds to the darkly shaded area in the figures.

3.2.2 The Sideslip Rate Isoclines

The vehicle equilibria exist at intersections of the $\dot{r}$ and $\dot{\beta}$ nullclines. Figure 3.5 shows the analogous plots to Figure 3.4 for the sideslip rate isoclines. As can be seen between the two figures, for a given steering angle, the equilibria lie on both the yaw acceleration and sideslip rate nullclines at the same position in the phase plane.

The sideslip rate isoclines do not change much with steering, especially in the direction of the turn (for example, positive yaw rate and negative sideslip for a left hand turn). This illustrates why it is difficult to influence the sideslip angle through changes to lateral tire force, and also corroborates Inagaki's observation that the equilibria tend not to move much in the $\beta - \dot{\beta}$ phase plane [29]. The plots point out

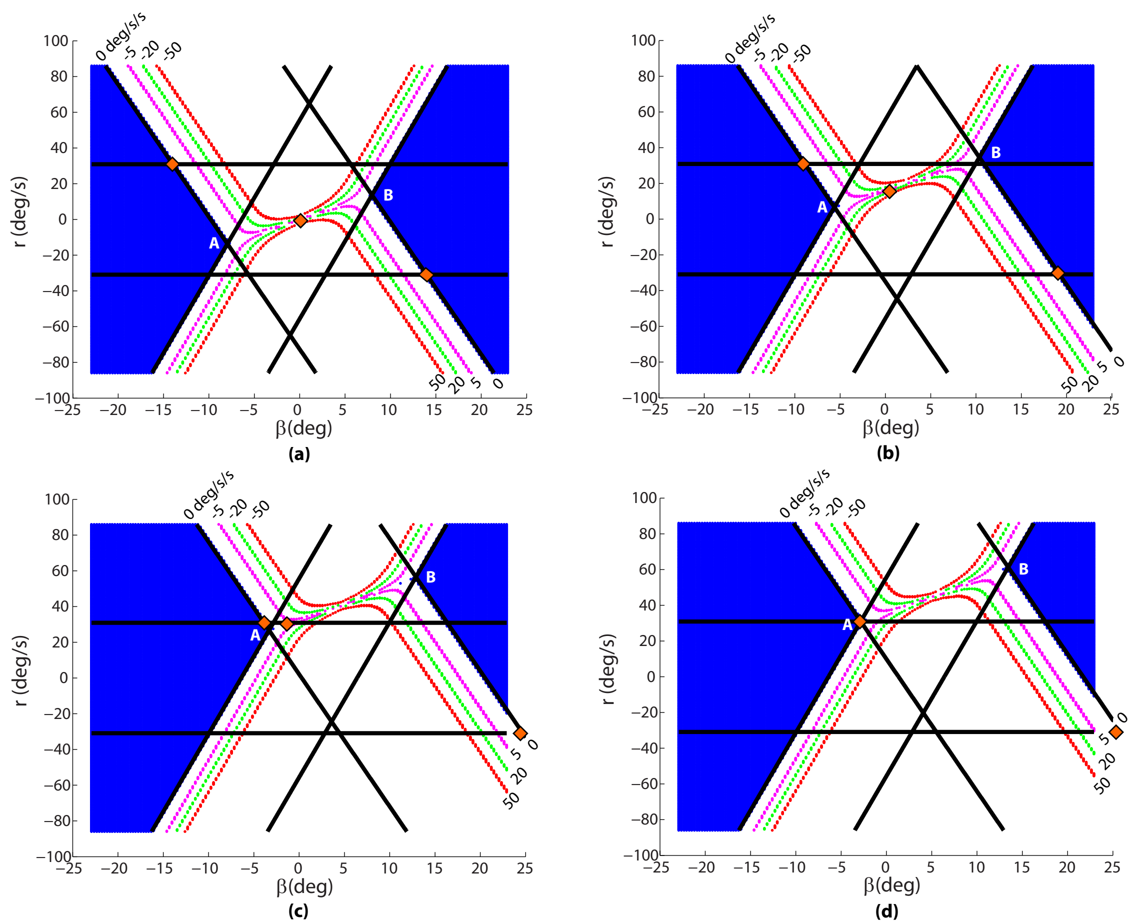

Figure 3.4: *The $\dot{r}$ Isoclines at μ = 0.55, V = 10m/s, and (a) 0° (b) 5° (c) 10° (d) 11° of Steering*

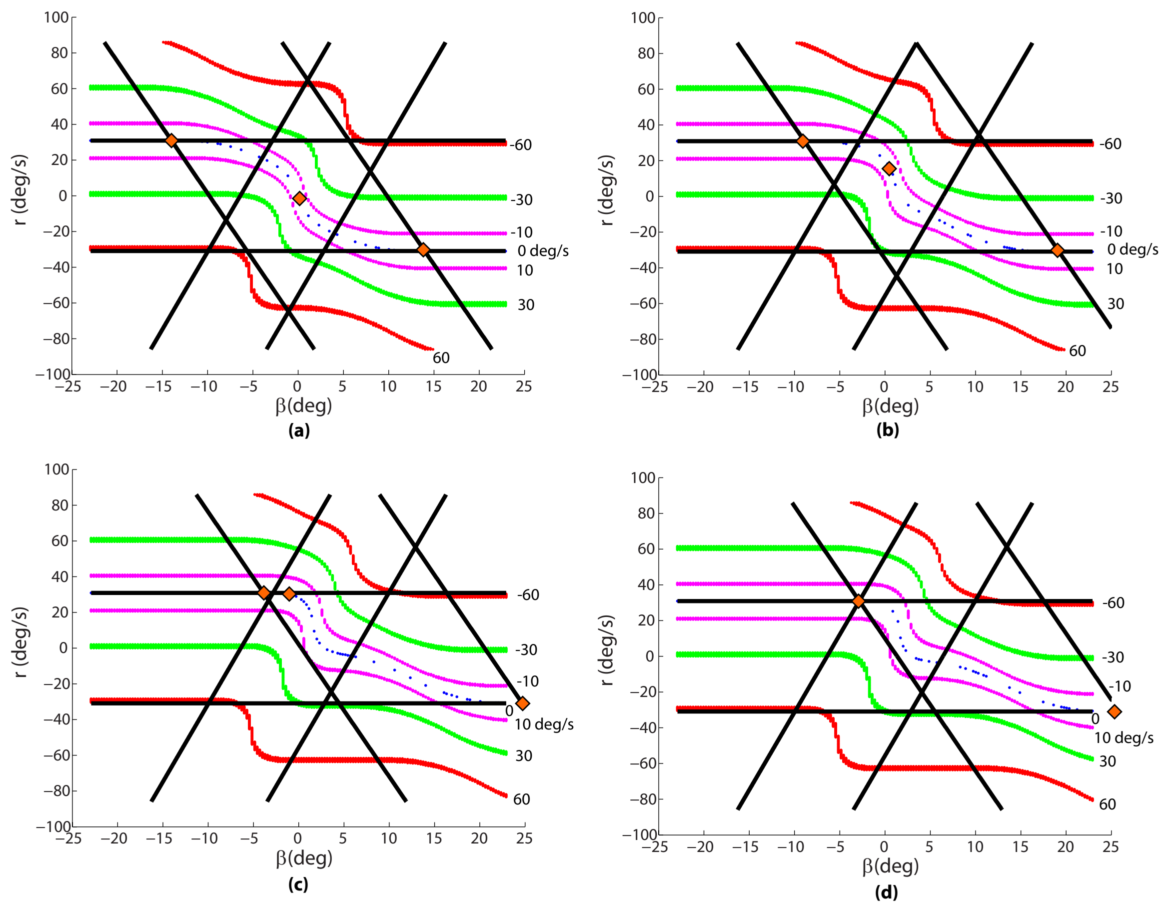

Figure 3.5: *The* $\dot{\beta}$ *Isoclines at* $\mu = 0.55$*,* $V = 10m/s$*, and (a) 0° (a) 5° (c) 10° (d) 11° of Steering*

the danger of the vehicle trajectory reaching high values of yaw rate: the sideslip rate also becomes high, leading to instability if the change in yaw rate is not high enough to counteract the change in sideslip.

3.3 Determining the Possibilities for Control Using the Phase Plane

Any chassis control system is limited by the actuators available on the vehicle. Different types of actuators can exert control over different forces on the vehicle: for example, front steering actuators control the value of front lateral tire force; front brake actuators control the value of front longitudinal tire force. It is important to understand how the existing actuators on a vehicle can modify the vehicle dynamics. The maximum and minimum control inputs result in a range of possible trajectories for a given set of vehicle states; these ranges are well illustrated by plotting the actuator's capabilities in the phase plane.

3.3.1 Steering Control

P1 and X1 are actuated by front steer-by-wire systems, which control the front lateral tire force through the steering angle, δ. Figure 3.6 shows the possible state trajectories for P1 given maximum and minimum front lateral force inputs at various points in the statespace. These trajectories account for steering actuator limitations as well as tire force generation capability. There are areas where the actuator can exert control effort in several directions, and areas where the vehicle trajectory cannot be changed. For example, the trajectories in the upper right and lower left corners, corresponding to high yaw rate and sideslip of the same sign, cannot be influenced by the front steering. Luckily, these areas are generally stabilizing – the trajectories push the car towards lower sideslip. There is a limit to the stabilizing capability of P1's actuators under the given conditions, which can be seen at extremely high yaw rate and high negative sideslip (and vice-versa): in this area of the statespace the actuator is saturated, and the open loop unstable trajectory cannot be changed. Any envelope control system that will stabilize P1 must keep the vehicle away from these areas in the phase plane that are unstable and uncontrollable.

3.3.2 Braking Control

Steer-by-wire is not necessary to the success of a control scheme– other actuators like differential braking or torque vectoring can be chosen if they meet the requirements for speed and control effort. Many production vehicles today offer Electronic Stability Control that is actuated by a four-wheel Anti-Lock Braking System. As with steering,

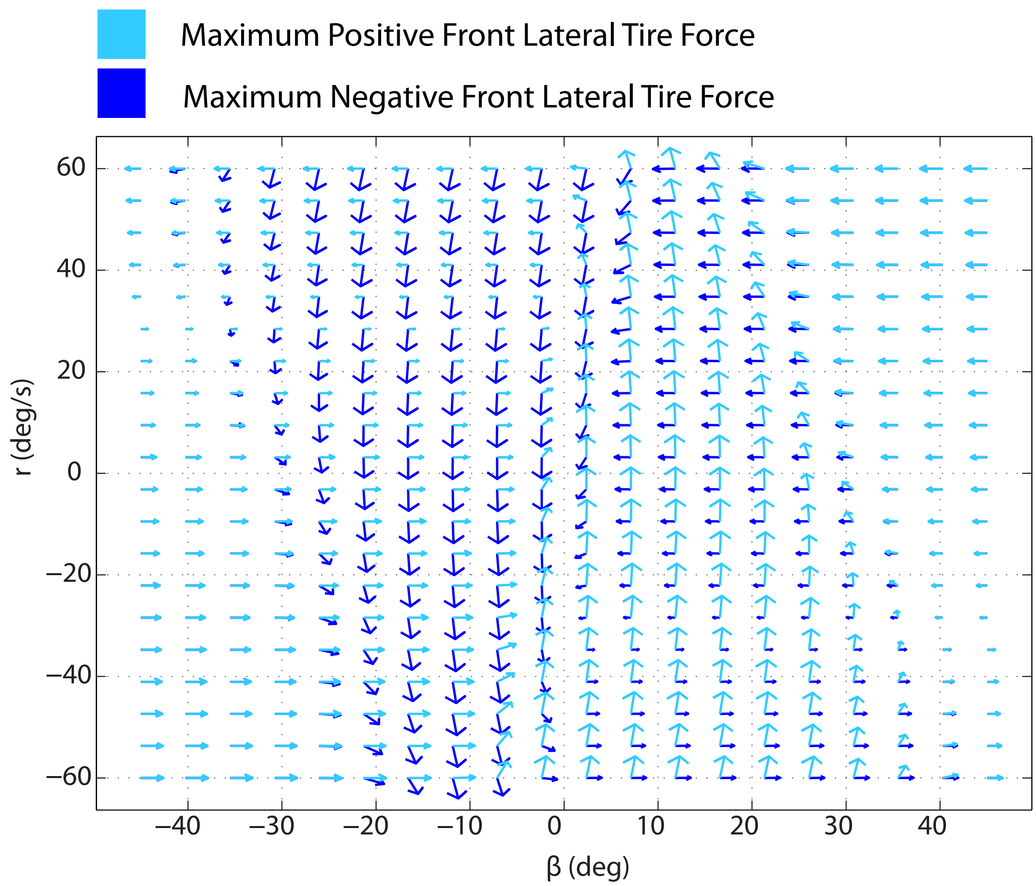

Figure 3.6: *Available State Space Trajectories with Front Steering Control for* $V_x = 10m/s$, $\mu = 0.55$

the effects of braking are also illustrated well in the phase plane. To correct a limit-oversteer maneuver, the front, outside wheel should brake to provide a restoring torque on the yaw acceleration. The range of possible vehicle trajectories provided by front axle braking are illustrated by the difference between maximum braking on the front right wheel, versus maximum braking on the front left wheel.

While the steering control analysis only takes lateral tire forces into account using the lateral brush tire model, this analysis uses the coupled force brush tire model in order to include the longitudinal braking forces. Figure 3.6 illustrates the effect on the vehicle trajectory from braking the front right or left wheel, while allowing the lateral forces to develop naturally. For either wheel, the maximum braking throughout a majority of the phase plane occurs at approximately $20 - 40\%$ slip.

The effect on the vehicle trajectory of braking versus steering is quite different. Braking can effect portions of the phase plane that steering cannot, for example in areas of extremely high magnitude sideslip. For low magnitudes of yaw rate, steering can achieve similar trajectories to braking, but can additionally achieve a much wider range of trajectories. Both front steering and front braking can provide stabilizing trajectories throughout large portions of the phase plane. Ideally, a combination of both actuators could provide a control system with a wider range of possible trajectories.

3.4 Choosing a Safe Envelope in the Phase Plane

It is easiest to choose and understand a safe envelope if it can be defined both mathematically and graphically. Because vehicle stability characteristics are well captured by the two-state planar bicycle model with a nonlinear lateral brush tire model, the sideslip-yaw rate $(\beta - r)$ phase plane provides straightforward visualization of the vehicle dynamics. The phase plane view allows an engineer to quickly determine a safe operating region for the vehicle and design a control scheme that works hand-in-hand with the open loop dynamics.

The simplest choice of boundary is a direct, constant limit on one of the states, which prevents the vehicle from entering a region of instability. For example, a yaw

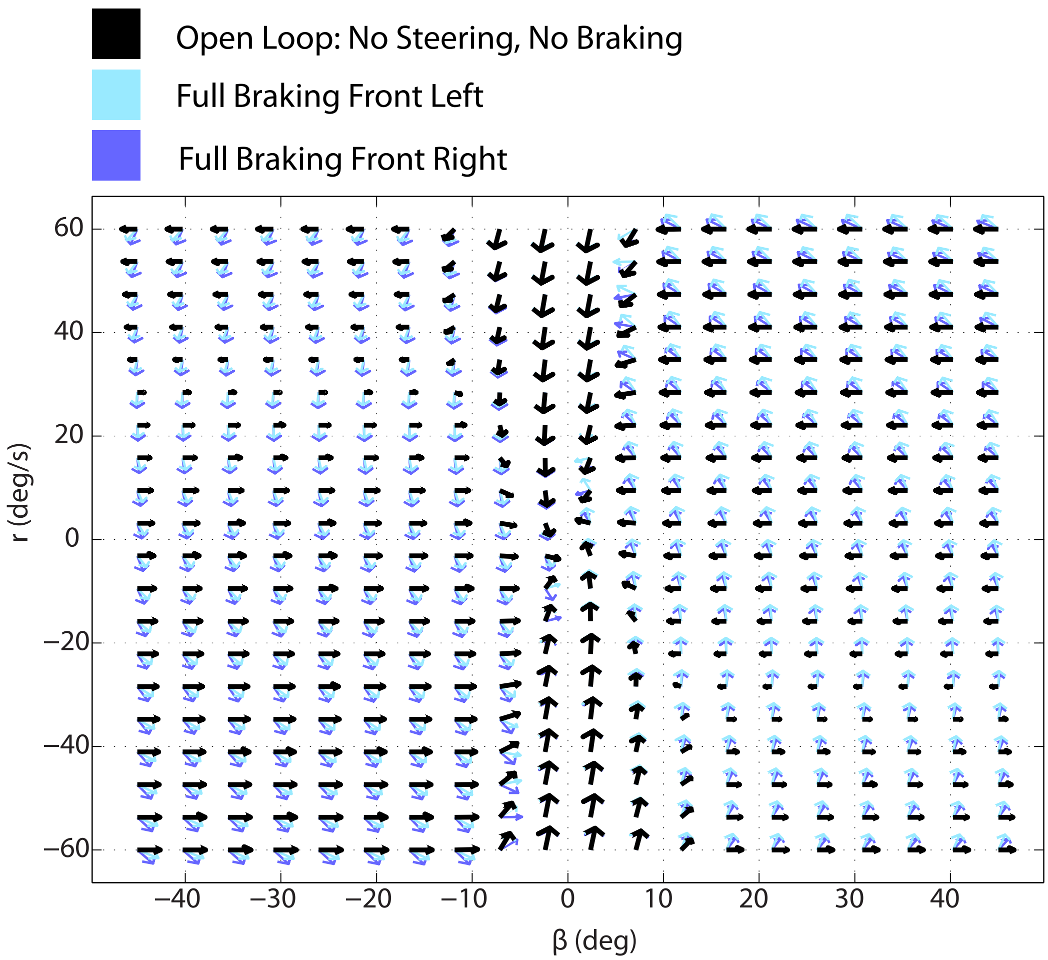

Figure 3.7: *Available State Space Trajectories with Front Braking Control for* $V_x = 10m/s$, $\mu = 0.55$

rate boundary at the maximum steady state yaw rate (which is constant for a given speed and friction) prevents the vehicle from increasing in yaw rate past an unstable equilibrium point. This boundary is illustrated in Figure 3.8 Plot (a), with a high steering angle of $10°$, a speed of $10m/s$ and a friction of 0.55. Similarly, a direct limit on sideslip angle can prevent the sideslip from increasing past the unstable equilibria as well (shown in Plot (b)). Alternately, sloped limits through the saddle equilibria, as in Plot (c), provide a similar bound. In the latter two cases, the bounds must move to stay coincident with the unstable equilibria for all steering angles. While these bounds keep the trajectory away from the unstable regions of the phase plane, they still allow one of the states to grow beyond the normal operating range of the vehicle. With the envelope consisting of maximum steady state yaw rate bounds, for example, the sideslip is unbounded; any unusually large growth in sideslip angle could alarm the driver.

A closed boundary in the state-space prevents growth of any state. Beal et al. suggest an envelope bounded by the lines of maximum rear slip angle and the lines of maximum steady state yaw rate, forming a parallelogram in the state space, as given by Equation 3.9 through Equation 3.12 [7]. While these boundaries encompass a large region of the stable state space and normal operating range, they prevent the vehicle from reaching yaw rates above steady state, which may occur in transient maneuvers. This can result in a degradation of cornering feel, and also causes the controller to fight against the natural, stable, transient dynamics. Figure 3.9 shows the maximum steady state yaw rate limits and maximum rear slip angle limits overlayed on open loop phase portraits at a speed of $10m/s$ and a friction of 0.55; it is apparent that using these boundaries would eliminate the transient portions of the trajectories.

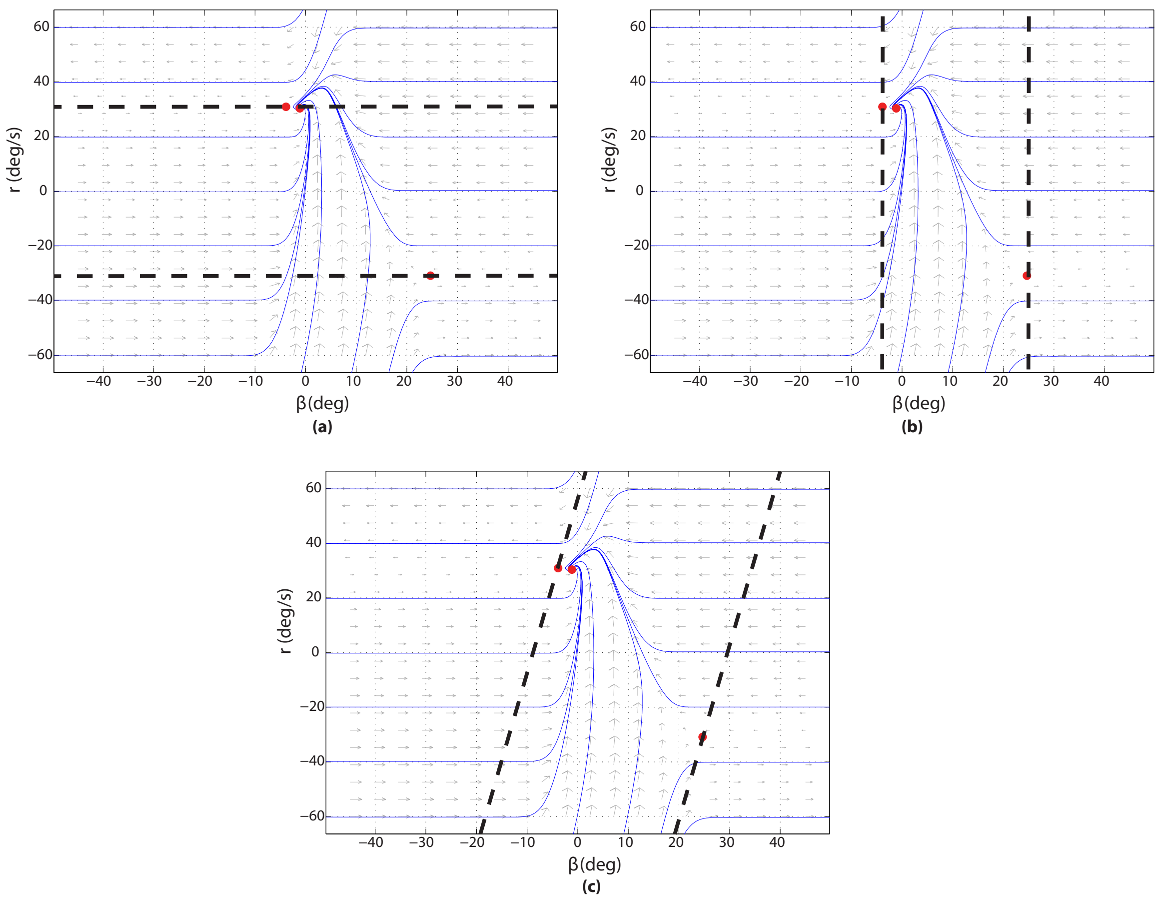

Figure 3.8: *Open Loop Dynamics at 10 Degrees of Steering with (a) Constant Yaw Rate (b) Constant Sideslip (c) Sloped Sideslip Boundaries*

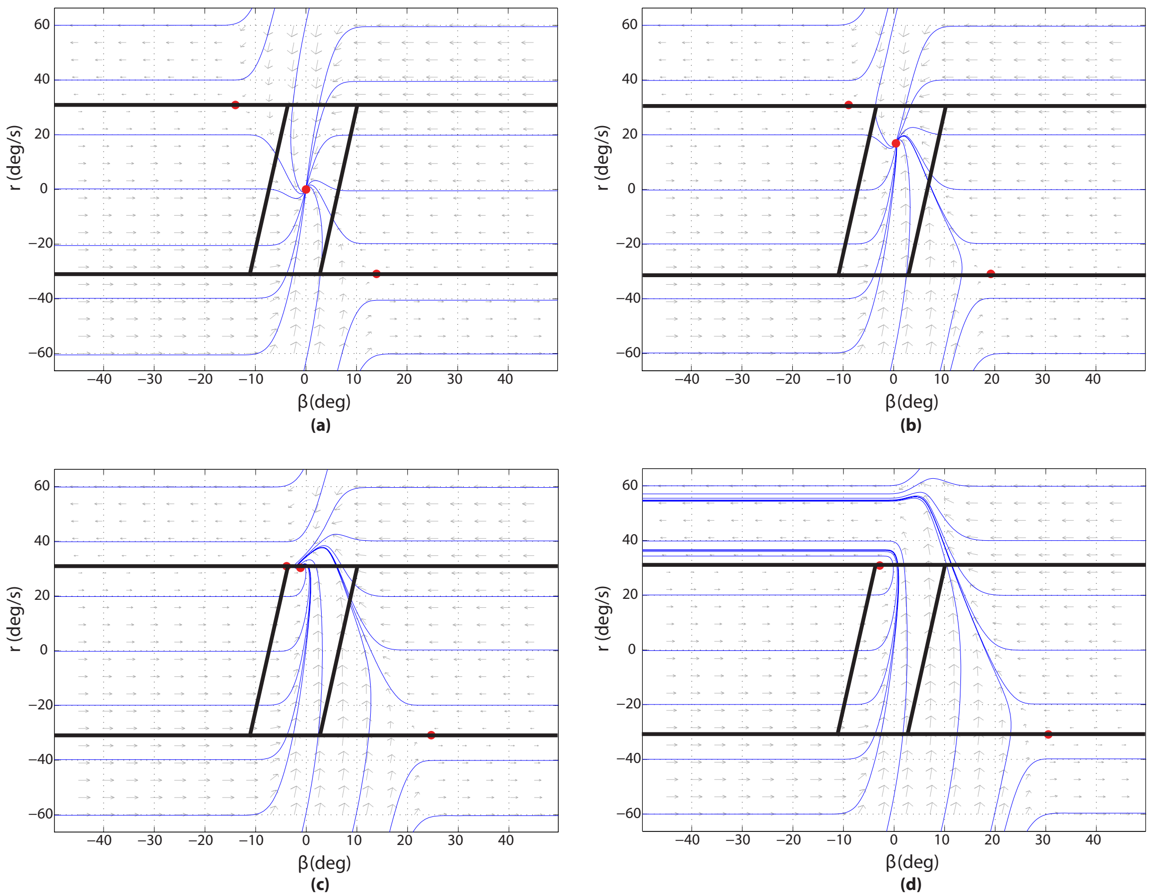

Figure 3.9: *Open Loop Dynamics with Beal's Boundaries at (a) 0 Degrees (b) 5 Degrees (c) 10 Degrees (d) 15 Degrees of Steering*

$$r_{max,ss} = \frac{\mu g}{V_x} \tag{3.9}$$

$$r_{min,ss} = -\frac{\mu g}{V_x} \tag{3.10}$$

$$\beta_{\alpha_r,max} = \frac{br}{V_x} + tan(\alpha_{sl,r}) \tag{3.11}$$

$$\beta_{\alpha_r,min} = \frac{br}{V_x} - tan(\alpha_{sl,r}) \tag{3.12}$$

3.4.1 The Nullcline Boundary

Instead of using the maximum steady state yaw rate as a boundary, another choice is a boundary that limits yaw rate while allowing the transient overshoot dynamics. This boundary should be as consistent with the natural dynamics as possible. The line corresponding to the linearized $\dot{r} = 0$ nullcline at a steering angle of δ_{max} (see Equation 3.8) encapsulates a majority of the stable open loop trajectories of the vehicle in the yaw direction of the phase plane. By choosing this nullcline as the boundary, the yaw rate is allowed to grow to its stable maximum with natural overshoot. Outside the envelope, the open loop dynamics for stable steering angles already serve to push the car back in the direction of the boundary due to the change in sign of the yaw acceleration at the nullcline. This line also follows the angle of the trajectories in the phase plane at a steering angle of δ_{max}, which suggests that any command given by the controller along the boundary will resemble the open loop steer angle. The maximum rear slip angle limits bound the stable trajectories in the sideslip direction; however, skilled drivers may prefer a slightly wider sideslip boundary to allow drifting. Figure 3.10 shows the chosen envelope boundaries in black for several steering angles at a constant speed and friction. This boundary shape is called the Nullcline Boundary, since the yaw rate limit is defined as the linear approximation of the maximum stable yaw acceleration nullcline. The boundary does not change with steering angle if speed and friction are held constant.

The equations for these boundary lines are noted below. The line between F and D is determined by the maximum rear slip angle (see Equation 3.11) and the line between C and D is determined by the linear approximation of the $\dot{r}$ nullcline at δ_{max}. The remaining two lines are their opposites. As the equations suggest, these boundaries will change with speed and friction; Figure 3.11 shows changes in the boundary shape with speed. The width of the boundary in the sideslip direction does not change with speed, but the slope of the sideslip boundary does vary.

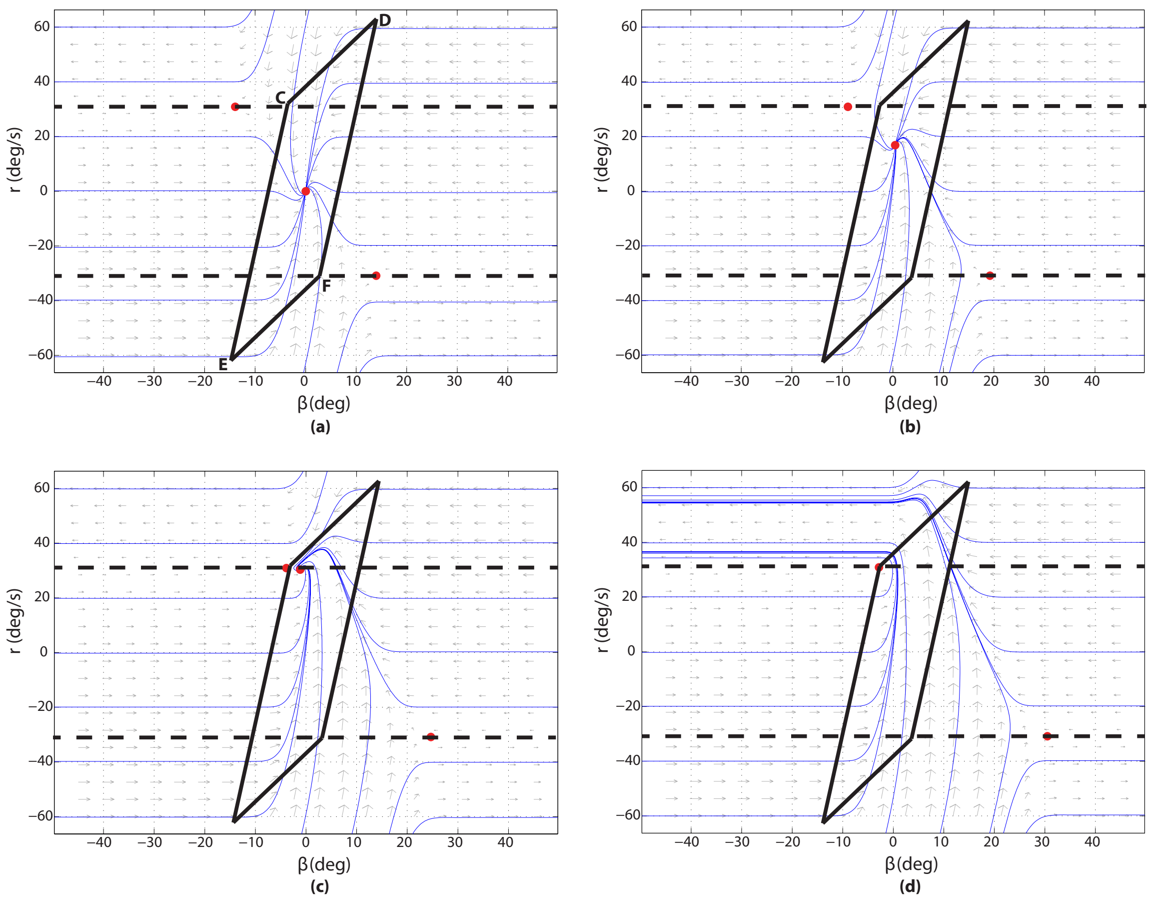

Figure 3.10: *Open Loop Dynamics with Nullcline Boundary at 10 m/s, μ = 0.55, and (a) 0 Degrees (b) 5 Degrees (c) 10 Degrees (d) 15 Degrees of Steering*

$$\overline{FD} : \beta = b_0 r + b_1 \tag{3.13}$$

$$\overline{CD} : r = b_3 \beta + b_4 \tag{3.14}$$

$$\overline{EC} : \beta = b_0 r - b_1 \tag{3.15}$$

$$\overline{EF} : r = b_3 \beta - b_4 \tag{3.16}$$

$$b_0 = \frac{b}{V_x} \tag{3.17}$$

$$b_1 = tan(\alpha_{sl,r}) \tag{3.18}$$

$$b_3 = \frac{r_D - r_C}{\beta_D - \beta_C} \tag{3.19}$$

$$b_4 = r_C - \beta_C \frac{r_D - r_C}{\beta_D - \beta_C} \tag{3.20}$$

$$r_C = \frac{\mu g}{V_x} \tag{3.21}$$

$$r_D = \frac{V_x}{a+b}(tan(\alpha_{sl,f} + \delta_{max}) - tan(\alpha_{sl,r})) \tag{3.22}$$

$$\beta_C = \frac{bg\mu}{V_x^2} - tan(\alpha_{sl,r}) \tag{3.23}$$

$$\beta_D = \frac{b}{a+b}(tan(\alpha_{sl,f} + \delta_{max}) - tan(\alpha_{sl,r})) + tan(\alpha_{sl,r}) \tag{3.24}$$

The favorable qualities associated with this set of boundaries lead to its use in the subsequent chapter as the safe region for envelope control.

3.5 Accounting for Understeer and Oversteer

The previous analysis in this chapter assumes equal friction on the front and rear axles. In reality, one axle may have less force capability, due to weight transfer or drive and brake torques, for example. In this section, a decrease in force capability on either axle is modeled as a 10 percent loss of friction on that axle (from a maximum of $\mu = 0.55$). A decrease in available force on the rear axle causes the vehicle to tend towards a limit oversteer condition, where the rear axle saturates before the front; likewise, a decrease in available force on the front axle causes the vehicle to tend

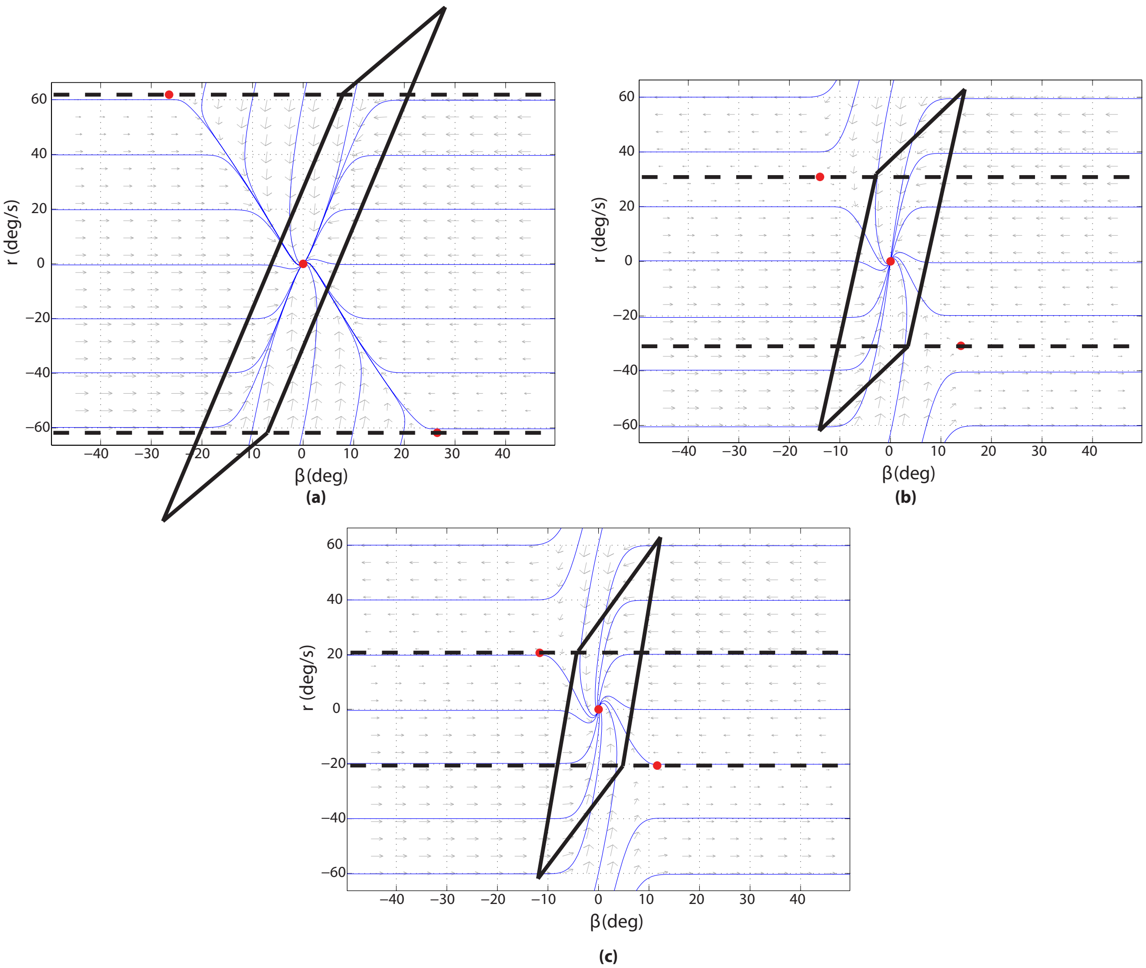

Figure 3.11: *Open Loop Dynamics with Nullcline Boundary at $\mu = 0.55$, $\delta = 0°$, and a Speed of (a) 5 m/s (b) 10 m/s (c) 15 m/s*

towards a limit understeer condition, where the front axle saturates first. Both of these limit situations result in changes to the dynamics of the system.

During limit understeer, the saddle equilibria disappear and there is a single, stable equilibrium point for the vehicle at all speeds and steering angles. Figure 3.12 shows the progression of the dynamics for several steering angles at a speed of $10m/s$. The dotted lines in the figure denote the maximum steady state yaw rate, which is determined by the lower, front axle coefficient of friction:

$$r_{max,ss,understeer} = \frac{\mu_f g}{V_x} \tag{3.25}$$

Solid black lines denote the nullcline envelope as determined for a neutral vehicle. Because the maximum steady state yaw rate for an understeering vehicle is lower than for the neutral vehicle, the stable equilibrium point lies further inside the boundary than it would for the neutral case. Nevertheless, for steering angles close to, but below, the maximum stable steering angle (as calculated for the neutral vehicle), the dynamics still follow the slope of the yaw rate boundary well; this is illustrated best in Plot (c), and is due to the fact that the slope of the yaw acceleration nullcline within the boundary does not change significantly with the drop in friction on the front axle. Although the unstable equilibria do not occur in the understeering case, the dynamics outside the boundary have large deviations in sideslip before returning to the stable equilibrium, which can feel unnatural to the driver and should be avoided.

The case of limit oversteer is also slightly different from the neutral vehicle. Figure 3.13 shows the oversteering dynamics for several steering angles at a speed of $10m/s$. The dotted lines in the figure denote the maximum steady state yaw rate, which is now determined by the lower, rear axle coefficient of friction:

$$r_{max,ss,oversteer} = \frac{\mu_r g}{V_x} \tag{3.26}$$

The saddle equilibria still exist in this case, although the yaw rate tends to grow alongside the sideslip dynamics when the oversteering vehicle reaches instability. At high steering angles, a bifurcation still exists also, but the bifurcation is from one stable focus and two saddle points to only one saddle point. The neutral vehicle has

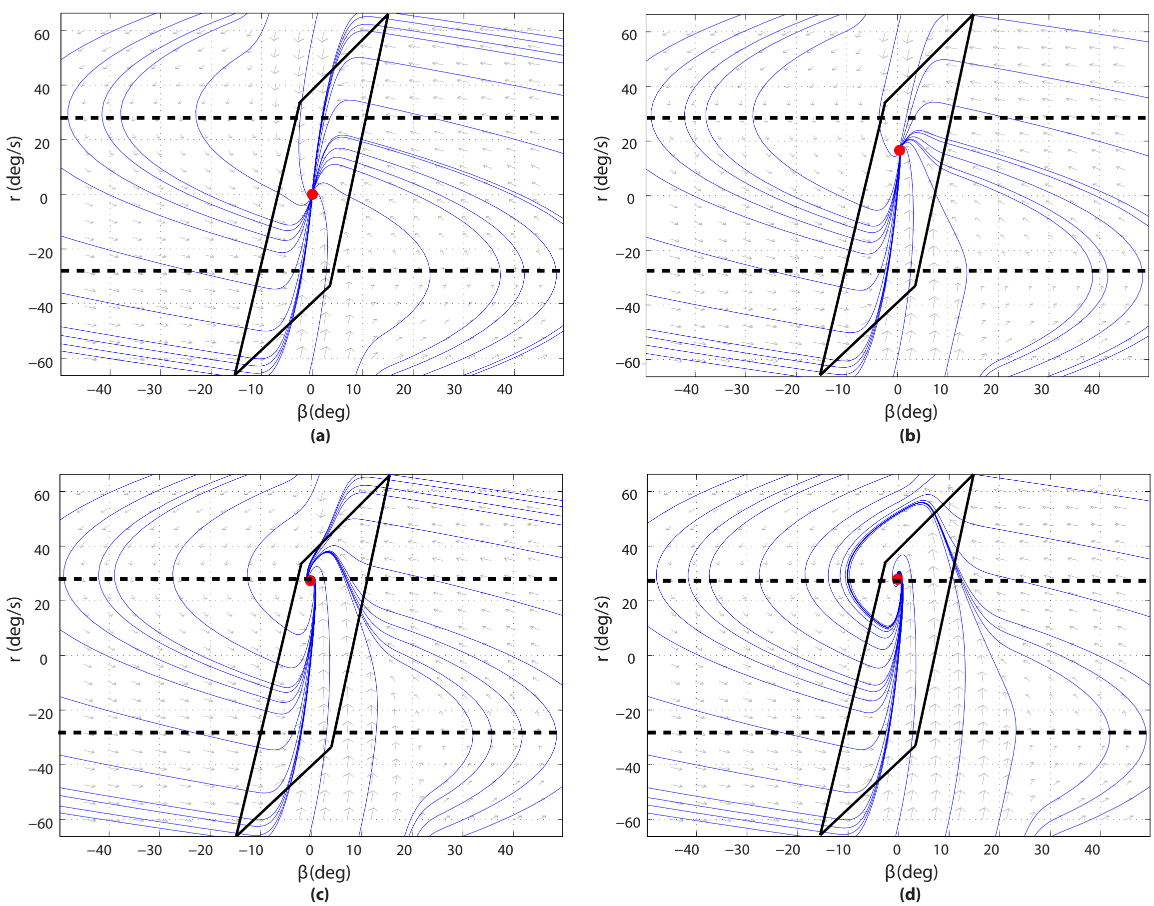

Figure 3.12: *The Phase Portrait of an Understeering Vehicle at V = 10m/s,* μ_r = *0.55,* $\mu_f = 0.9\mu_r$*, and (a) 0° (a) 5° (c) 10° (d) 15° of Steering*

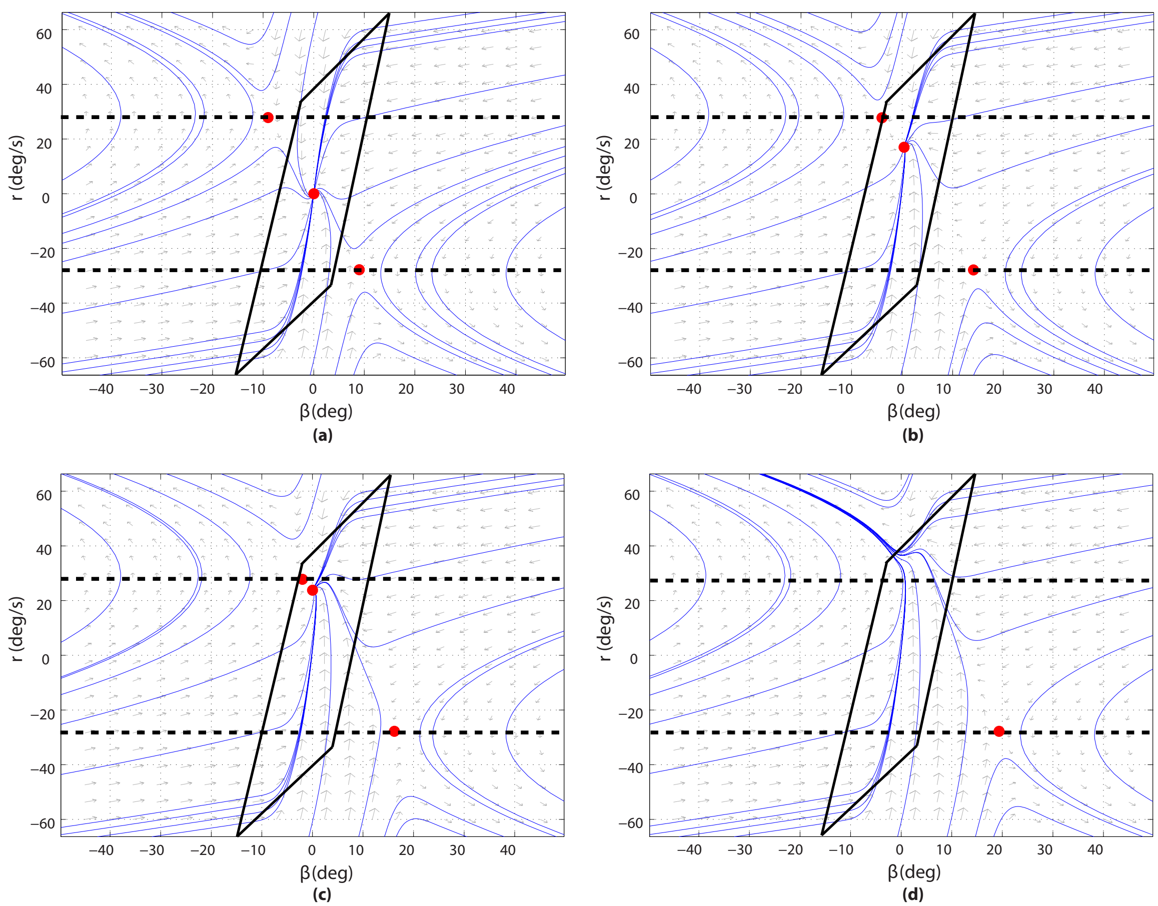

Figure 3.13: *The Phase Portrait of an Oversteering Vehicle at V = 10m/s, μ_f = 0.55, $\mu_r = 0.9\mu_f$, and (a) 0° (a) 5° (c) 7° (d) 10° of Steering*

an additional unstable focus point at high steering angles. Figure 3.13 also shows the nullcline boundary overlayed on each phase portrait. Again, the slope of the yaw acceleration nullcline within the boundary does not change significantly with the drop in friction on the rear axle, so the region of safe operation does not change significantly from the neutral case.

Although there are differences in the dynamics for neutral, limit oversteering, and limit understeering vehicles, in the regions of the phase plane that correspond to typical, stable driving, the dynamics and nullcline geometries are similar. This similarity will allow the choice of stable envelope, detailed in the next chapter, to rely on an analysis of the neutral vehicle alone.

3.5.1 Verifying the Entrance of Trajectories into the Boundary

With a choice of boundary defined in the previous sections, it is important to check that the control actuators on the chosen vehicle testbed can exert a control effort allowing the vehicle to reenter the safe state space after escaping the envelope. P1 is actuated through front steer-by-wire, which controls front lateral force; therefore, at every point along the boundary, there should be a choice of front lateral force (within the range of the actuator) that can redirect the vehicle trajectories to point inside, or at least along, the boundary.

Figure 3.14 shows the possible state trajectories for P1 given maximum and minimum front lateral force inputs at various points in the statespace. Overlaying the boundary on the possible trajectories, it is apparent that at most points along the boundary, there are possible choices of front lateral force that will direct the trajectory into the safe area. The upper right and lower left corners, however, are areas in which the front lateral force has little to no control authority. By cutting the corners of the boundary (shown by the dotted lines in Figure 3.14) to create a hexagonal area, the trajectories in these corners are directed inwards. The corner boundary lines, determined by the points G and H, are defined generally as follows, where the values for ρ_G and ρ_H are chosen for P1 as 0.55 and 0.5, respectively:

$$r_G = \rho_G(r_D - r_C) + r_C \tag{3.27}$$

$$B_G = \frac{1}{b_3}(r_G - b_4) \tag{3.28}$$

$$r_H = \rho_H(r_D - r_C) + r_C \tag{3.29}$$

$$B_H = b_0 r_H + b_1 \tag{3.30}$$

These equations, combined with those describing the yaw rate and sideslip bounds, result in the final, hexagonal incarnation of the nullcline envelope.

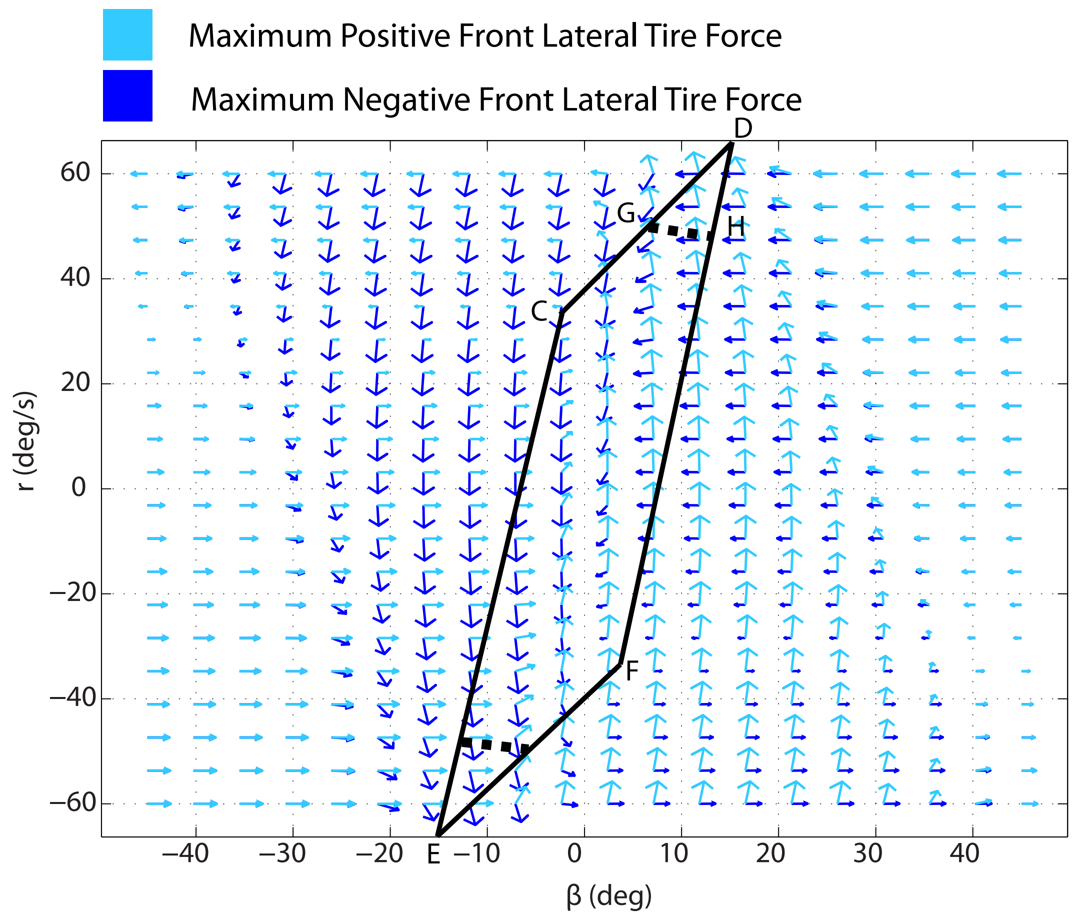

Figure 3.14: *Available State Space Trajectories along the Nullcline Boundary:* $V_x = 10m/s$, $\mu = 0.55$

Chapter 4

Vehicle Envelope Control

4.1 Attractive Envelope Control Structure

In order to afford the driver open loop operation during safe driving conditions, but also provide stabilization in unsafe conditions, the envelope controller presented in this thesis activates only after the vehicle states exit a safe operating envelope. When the vehicle states move outside the envelope, the controller acts to move them back to a boundary defined by a linear combination of the vehicle states (similar to those of Hong and Uematsu [24, 50]). By controlling the car in this way, the dynamics of the vehicle outside the safe envelope are designed to push the car back into the envelope's safety. A lack of state tracking within the envelope affords the driver a more natural driving experience that is not influenced by deviations from the desired model in the instance of parameter and state uncertainty.

4.1.1 Defining the Attractive Dynamics

In sliding surface control, the state dynamics are constrained to a surface defined by some combination of state errors. In a similar way, the attractive envelope controller defines a value S, which is a measure of the distance from the boundary. The boundary should be coincident with $S = 0$, so that as the vehicle trajectories cross outside the envelope boundaries, the controller provides a response to push the vehicle back

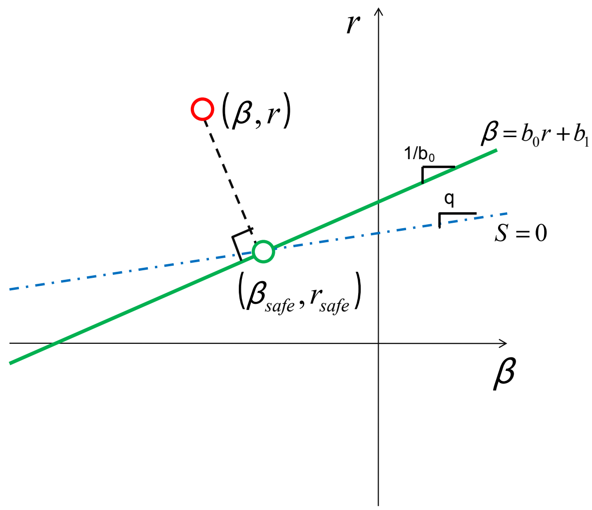

Figure 4.1: *Defining the Safe Point and S*

towards the boundary. Because the value S should reflect the distance of the vehicle states from the safe boundary, it is defined as a linear combination of the state errors from the current states to the closest point on the safe boundary (Equation 4.1). The desired dynamics of S are given by Equation 4.2, where K is the controller gain and q is a positive constant. While S explicitly seems to be a function of only r and β, it is in general a function of the three-dimensional state space that includes vehicle speed V_x due to the boundary's dependence on speed.

$$S = (r - r_{safe}) - q(\beta - \beta_{safe}) \tag{4.1}$$

$$\dot{S} = -KS \tag{4.2}$$

A graphical representation of this construction is shown in Figure 4.1. The point (β, r) denotes the current vehicle state, which is outside the safe boundary. (β_{safe}, r_{safe}) is the closest point on the safe boundary to (β, r). The instantaneous definition of the line $S = 0$ is also shown. This line has a slope q in the $\beta - r$ plane, and intersects the safe boundary at (β_{safe}, r_{safe}). Any value of q such that the instantaneous line of $S = 0$ and the boundary are not perpendicular is acceptable.

When the vehicle state is outside the envelope, the calculation to define the closest boundary point uses a combination of least squares and least norms. The following equations detail this procedure for the rightmost (sideslip) boundary, where b_0 is the slope of the boundary line and b_1 is the β-intercept (Equation 3.13):

$$A = \begin{bmatrix} 1 \\ b_0 \end{bmatrix} \tag{4.3}$$

$$B = \begin{bmatrix} b_0 & -1 \end{bmatrix} \tag{4.4}$$

$$\begin{bmatrix} r_{safe} \\ \beta_{safe} \end{bmatrix} = A(A^T A)^{-1} A^T \begin{bmatrix} r \\ \beta \end{bmatrix} - b_1 B^T (B B^T)^{-1} \tag{4.5}$$

The topmost yaw rate boundary is defined similarly, where b_3 is the slope of the boundary line and b_4 is the yaw rate-intercept:

$$A = \begin{bmatrix} b_3 \\ 1 \end{bmatrix} \tag{4.6}$$

$$B = \begin{bmatrix} -1 & b_3 \end{bmatrix} \tag{4.7}$$

$$\begin{bmatrix} r_{safe} \\ \beta_{safe} \end{bmatrix} = A(A^T A)^{-1} A^T \begin{bmatrix} r \\ \beta \end{bmatrix} - b_4 B^T (B B^T)^{-1} \tag{4.8}$$

The slope and intercept for the corner boundary can be substituted in place of b_3 and b_4 to determine the equations for the safe state when the vehicle is in the corner region of the state space. The remaining boundaries are just reflections of these three examples across the yaw rate or sideslip axes.

4.1.2 Switching Between Boundaries

While the vehicle will most often exit the safe envelope at the yaw rate boundary due to the natural trajectories of the dynamics, it is possible that the car could exit one of the other boundaries. Upon exiting one boundary, the vehicle trajectories could also take it into the region of another boundary (for example, exiting the yaw boundary, and re-entering at the sideslip boundary). These types of transitions would most commonly be seen in the event of an incorrect parameter or state estimation, such as overestimating the friction, where the physical boundary differs from the model.

In the event that the trajectories cross from one boundary to the next while outside the safe envelope, the measure of distance S should be extended to be a continuous function in the state space. Figure 4.2 illustrates a choice of boundary regions that allows for continuity of the magnitude of level curves of S. Here S is signed to enable comparison with previous work in vehicle dynamics using sliding surfaces. The following analysis could be derived equivalently using the magnitude of S in order to avoid sign changes on the magnitude level curves. However, the signed value of S correlates directly with the direction of the steering control action, and thus gives additional physical insight.

With this setup, if the vehicle is outside the envelope ($S \neq 0$), and in the yaw region, the controller will direct it back to the yaw rate boundary. If the vehicle is in the slip region, it will be pushed to the sideslip boundary, and if it is in the corner region, it will move towards the corner boundary. The switching lines between regions are defined as the line between intersections of equal level curves of S for each adjacent region. The distance of the level curves from each boundary is determined by q in the formulation of S. The values of q_r and q_β can be chosen as desired for the yaw and sideslip boundaries; however, q_c for the corner boundary is chosen last to align the corner region level curves with the yaw region level curves, and to keep the yaw rate-corner transition line vertical in the $\beta - r$ plane for convenience. For the experimental work in this thesis, the yaw and sideslip boundary values of q_r and q_β are equal and constant over all speeds. The resulting structure of S over the entire phase plane is as follows:

$$S = \begin{cases} (r - r_{safe}) - q_\beta(\beta - \beta_{safe}) & \text{Slip Region} \\ (r - r_{safe}) - q_r(\beta - \beta_{safe}) & \text{Yaw Region} \\ (r - r_{safe}) - q_c(\beta - \beta_{safe}) & \text{Corner Region} \end{cases} \tag{4.9}$$

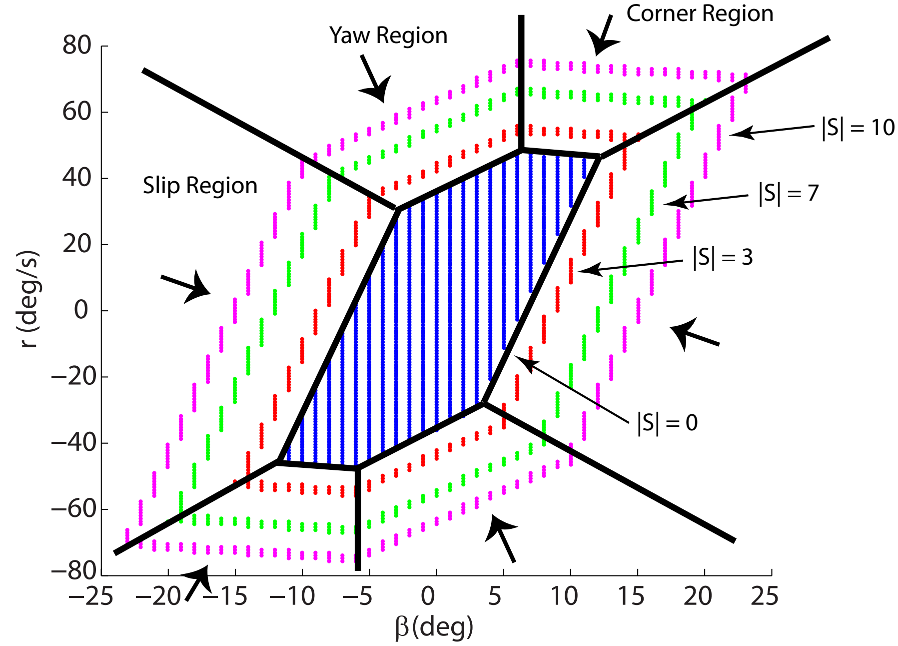

Figure 4.2: *Continuity of Level Curves of S Around the Safe Area*

4.1.3 Applying the Control

With the basic concept of the Envelope Controller defined above, this section describes the remaining details of the controller structure and implementation. Generally, if the states are not within the safe area, the controller must calculate an action to fulfill the desired dynamics of S. The controller output is a modification to the driver's desired steering angle, which is calculated from a desired front lateral tire force.

In order to calculate the desired force, necessary measurements from the vehicle include the driver's commanded steering angle (δ_{driver}), yaw rate (r), vehicle speed (V_x), and sideslip angle (β). Differentiation of the distance S results in an equation relating $\dot{r}$ and $\dot{\beta}$:

$$(\dot{r} - \dot{r}_{safe}) - q(\dot{\beta} - \dot{\beta}_{safe}) = -KS \tag{4.10}$$

Incorporating the bicycle model equations by substituting for $\dot{r}$ and $\dot{\beta}$ (Equation 2.3) and the safe state derivatives (in terms of r and β) leads to an expression for the necessary front lateral tire force ($F_{yf,des}$). For the positive sideslip boundary, the desired front lateral force is as follows:

$$
\begin{aligned}
F_{yf,des}\left(\frac{ab_0^2+aqb_0}{I_z}-\frac{b_0+q}{mV_x}\right) &= -KS(b_0^2+1)\\
&+F_{yr}\left(\frac{bb_0^2+bqb_0}{I_z}+\frac{b_0+q}{mV_x}\right)\\
&-r\left(q\dot{b_0}+q+b_0+\frac{2b_0\dot{b_0}(1-qb_0)}{b_0^2+1}\right)\\
&-\beta\left(2qb_0\dot{b_0}-\dot{b_0}+\frac{2b_0^2\dot{b_0}(1-qb_0)}{b_0^2+1}\right)\\
&-b_1\left(\dot{b_0}-\frac{2b_0\dot{b_0}(b_0+q)}{b_0^2+1}\right)
\end{aligned}
\tag{4.11}
$$

For the positive yaw rate boundary, the desired front lateral force is as follows:

$$
\begin{aligned}
F_{yf,des}\left(\frac{a+aqb_3}{I_z}-\frac{b_3+qb_3^2}{mV_x}\right) &= -KS(b_3^2+1)\\
&+F_{yr}\left(\frac{b+bqb_3}{I_z}+\frac{b_3+qb_3^2}{mV_x}\right)\\
&-r\left(\dot{b_3}(q-2b_3)+b_3+qb_3^2+\frac{2b_3^2\dot{b_3}(b_3-q)}{b_3^2+1}\right)\\
&-\beta\left(-\dot{b_3}+\frac{2b_3\dot{b_3}(b_3-q)}{b_3^2+1}\right)\\
&-b_4\left(-q\dot{b_3}+\frac{2b_3\dot{b_3}(1+qb_3)}{b_3^2+1}\right)\\
&+\dot{b_4}(qb_3+1)
\end{aligned}
\tag{4.12}
$$

Both of these equations assume that velocity can change with time, but friction is constant. The equations for the other yaw rate and sideslip boundary lines are similar to these, except for opposing signs on b_1 and b_4. Forces outside the corner boundary are calculated in the same way as the yaw rate boundary, with b_3 and b_4 replaced by the slope and r-intercept of the boundary line.

In order to solve these equations for the desired front lateral force, we must first determine the rear lateral tire force from the current states by using the tire model of Equation 2.15. After determining the front tire force, we can again use the tire model in reverse to calculate the necessary front slip angle $\alpha_{f,des}$, and from there solve for the desired front steering angle (δ_{des}):

$$\delta_{des} = atan\left(\beta + \frac{ar}{V_x}\right) - \alpha_{f,des} \tag{4.13}$$

Note that in solving for both slip angles and lateral tire forces, a maximum force is assumed based on the friction coefficient. This institutes a limit on force generation, and consequently, on the steer angle.

4.1.4 Attractiveness of the Envelope in the State Space

Because S is a complex function of yaw rate, sideslip, and speed, it is necessary to ensure that even in the presence of tire and steering actuator saturation a control action that decreases the value of $|S|$ exists. An analysis at each point in the phase plane shows the feasibility of the combined envelope and controller. In order to verify attractiveness of the envelope for all yaw rate and sideslip values, the magnitude of S at every point must be decreasing at a non-zero rate for some small, positive η:

$$S\dot{S} \leq -\eta|S| \tag{4.14}$$

Figure 4.3 plots the areas outside the envelope that are attractive, given constraints on maximum available force and steering angles. The areas in dark grey indicate portions of the state space for which S will move towards zero, pushing the trajectory back into the safe area (shown in white). The light grey, hatched areas show the portions of the state space for which attractiveness is not guaranteed due to actuator limitations on the steering angle. The black lines indicate the maximum/minimum rear slip angles and the maximum/minimum steady state yaw rates. There is a large area outside the safe envelope for which the closed loop dynamics are guaranteed to be attractive.

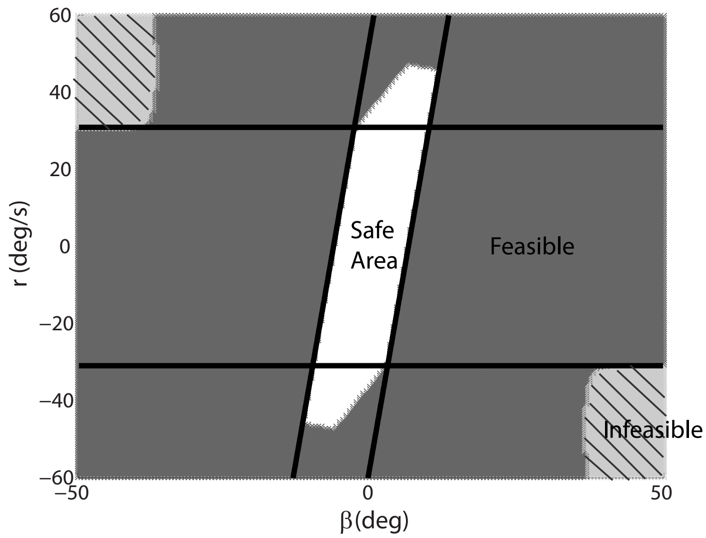

Figure 4.3: *Attractive Region of the Phase Plane at* $V_x = 10m/s$, $\mu = 0.55$

To ensure the attractiveness of the controller during changes in speed V_x, Figure 4.4 gives a similar analysis for nonconstant values of $\dot{V}_x$. Each instance assumes either maximum braking or maximum longitudinal acceleration, which are limited by the friction coefficient to a magnitude of μg. In the case of braking, the envelope size grows, and the region where attractiveness is infeasible shrinks. For acceleration, the envelope size decreases, and the infeasible region grows slightly.

One of the main concerns in regards to this control scheme is whether the controller will still function as desired in the event of a sudden and undetected change in friction. Imagine that the friction suddenly decreases by 75% from $\mu = 0.55$ to $\mu = 0.15$; this roughly corresponds to a switch from gravel to ice. If the vehicle does not know that the friction has changed, the controller performance will degrade to some degree. In Figure 4.5, Plots (a) and (b) show the open loop dynamics for both levels of friction at zero steering and $V_x = 10m/s$. The area of infeasibility is very large for the lower friction value due to a small steady state yaw rate, and the safe area for the lower friction is also much smaller. If the vehicle incorrectly assumes a higher friction, the controller will engage much later than if the friction is estimated correctly. However, this does not mean the controller cannot stabilize the car. Plots (c) and (d) show the

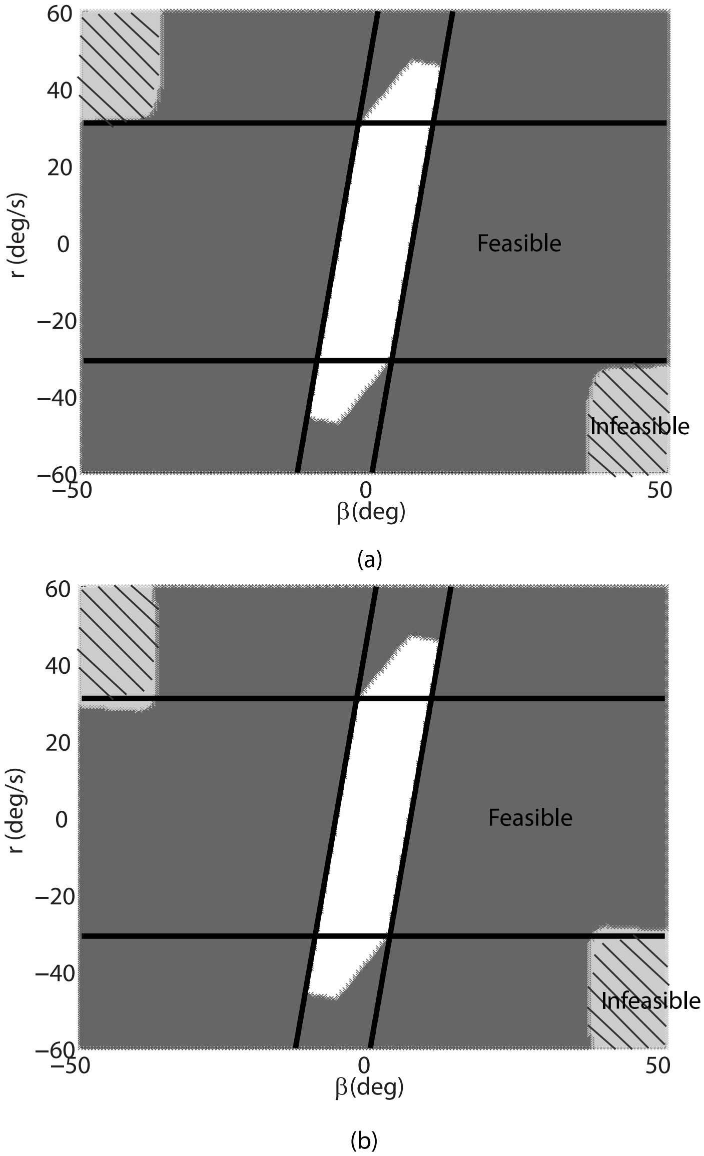

Figure 4.4: *Attractive Region of the Phase Plane at $\mu = 0.55$ and $V_x = 10m/s$ for (a) maximum braking and (b) maximum longitudinal acceleration*

closed loop dynamics and envelope boundaries while correctly estimating $\mu = 0.15$, and while incorrectly estimating $\mu = 0.55$ on a surface of $\mu = 0.15$, respectively. From a visual inspection, the controller successfully stabilizes the vehicle in both cases over a large region of the phase plane. The main difference between the two cases is a larger region of open loop operation when the friction is overestimated.

The ability of the controller to attract the vehicle to the envelope while assuming an incorrect friction depends on the fulfillment of the requirement of Equation 4.14, while recalculating $\dot{S}$ with the correct friction after the control action is determined. Plot (e) shows the attractive region of the state space if the friction is known to be $\mu = 0.15$. Plot (f) shows the feasibility if the controller incorrectly assumes the higher value for friction ($\mu = 0.55$). By comparing Figure 4.3 and Figure 4.5 Plots (e) and (f), it is apparent that the infeasible portions of the phase plane have grown due to the lower friction, and thus lower force capabilities. In regions where attraction is not guaranteed if the friction is estimated correctly, it is also not guaranteed for misestimated friction. This becomes problematic when the safe area defined by the overestimated friction becomes close or coincident with the portions of the phase plane where the stability is not guaranteed. Although the safe area defined by the actual friction may be very far from any infeasible regions, this is not necessarily true of the safe area defined by the overestimated friction.

Large portions of the phase plane directly outside the yaw rate and sideslip boundaries are guaranteed to be attractive, even when the friction is grossly overestimated. When overestimating friction, the envelope boundaries are much looser than they would be at the correct friction, but the controller will still function to stabilize the car. The trajectories for low friction will destabilize in open loop inside the limits of the higher friction envelope, so trajectories will tend to exit the overestimated safe area at the sideslip boundary (see open loop trajectories in Figure 3.1 and Figure 4.5). Trajectories exiting the sideslip boundary instead of the yaw rate boundary are a good indicator of overestimated friction.

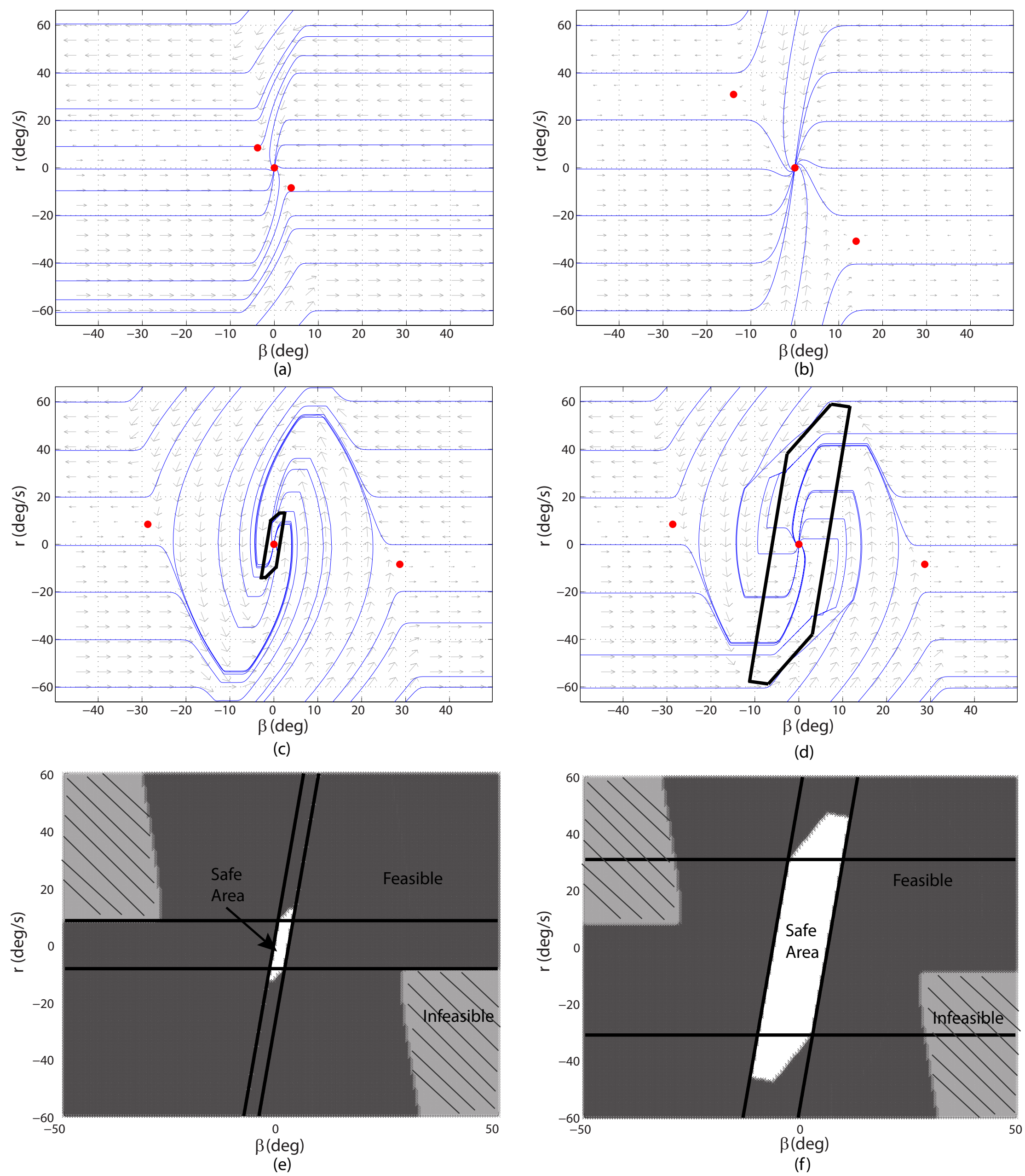

Figure 4.5: *At $V_x = 10m/s$, (a) Open Loop Phase Portrait for $\mu = 0.15$ and $\delta = 0°$, (b) Open Loop Phase Portrait for $\mu = 0.55$ and $\delta = 0°$,(c) Closed Loop Phase Portrait for $\mu = 0.15$ and $\delta = 0°$,(d) Closed Loop Phase Portrait for $\mu = 0.15$ and $\delta = 0°$ when μ is Estimated as 0.55, (e) Feasibility of S Corresponding to Plot(c), and (f) Feasibility of S Corresponding to Plot(d)*

4.1.5 Inner Boundary Proportional Control

While the envelope boundaries, especially the yaw rate boundary, were chosen to be in line with the open loop dynamics, any difference between the open loop trajectory and that specified by the envelope controller will be felt by the driver as the controller switches on. In order to ensure a smooth landing at the yaw rate boundaries, the addition of some control within the boundary is necessary. Because the sideslip boundaries are rarely reached first in practice, inner boundary control leading up to the yaw rate limits is sufficient. Ideally, the inner boundary control should have little effect on the driver's input when that input is safe, and should have little effect on state trajectories well inside the boundaries.

From the isocline analysis, it is known that a maximum steering angle exists to ensure open loop stability. Therefore, as the yaw boundaries are approached, the steering angle should be limited to this value. A solution for inner boundary control is then to provide a proportional limit on the steering angle that decreases it from the driver's large commanded steer angle to the maximum stable steer angle based on some measure of distance from the boundary.

Figure 4.6 illustrates the chosen geometry for proportional control, and Equations 4.15 to 4.17 give the control law. Only if the vehicle state is above the maximum steady state yaw rate (indicated by the black dotted lines), and the driver's steering angle is larger than the maximum stable steering angle (δ_{max}), does the controller begin to decrease the steering angle in proportion to the angle ϕ_c versus ϕ_s. This results in a controller action that does not affect the trajectories at low yaw rates, and does not modify the driver's steering angle unless it will result in an open loop instability. Effectively, this control law is changing the damping characteristics of the yaw response.

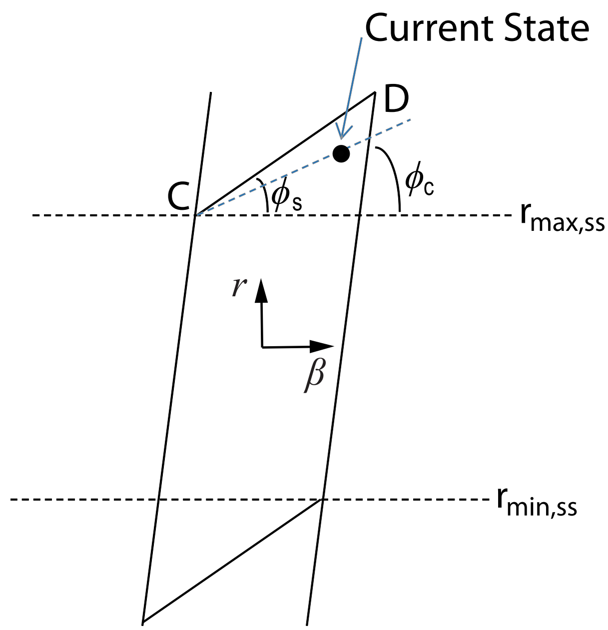

Figure 4.6: *Inner Boundary Proportional Control Geometry*

$$\delta_{control} = \delta_{driver} + \frac{\phi_c}{\phi_s}(\delta_{max} - \delta_{driver}) \tag{4.15}$$

$$\phi_s = arccos\left(\frac{\beta_D - \beta_C}{\sqrt{(\beta_D - \beta_C)^2 + (r_D - r_C)^2}}\right) \tag{4.16}$$

$$\phi_c = arccos\left(\frac{\beta - \beta_C}{\sqrt{(\beta_D - \beta_C)^2 + (r_D - r_C)^2}}\right) \tag{4.17}$$

The combined envelope control and inner boundary proportional controller trajectories are shown for several steering angles in Figure 4.7. In comparing these plots to the open loop trajectories in Figure 3.10, it is readily noticeable that the unstable saddle points have moved much further from the origin. They would in fact be stabilized completely in an ideal case; however, the physical limits of the steer-by-wire system prevent the trajectories in the far corners from stabilizing. The dynamics (and stable equilibria) within the safe area are unchanged, which can be seen by comparing the open and closed loop plots. The case that is most dissimilar between open and

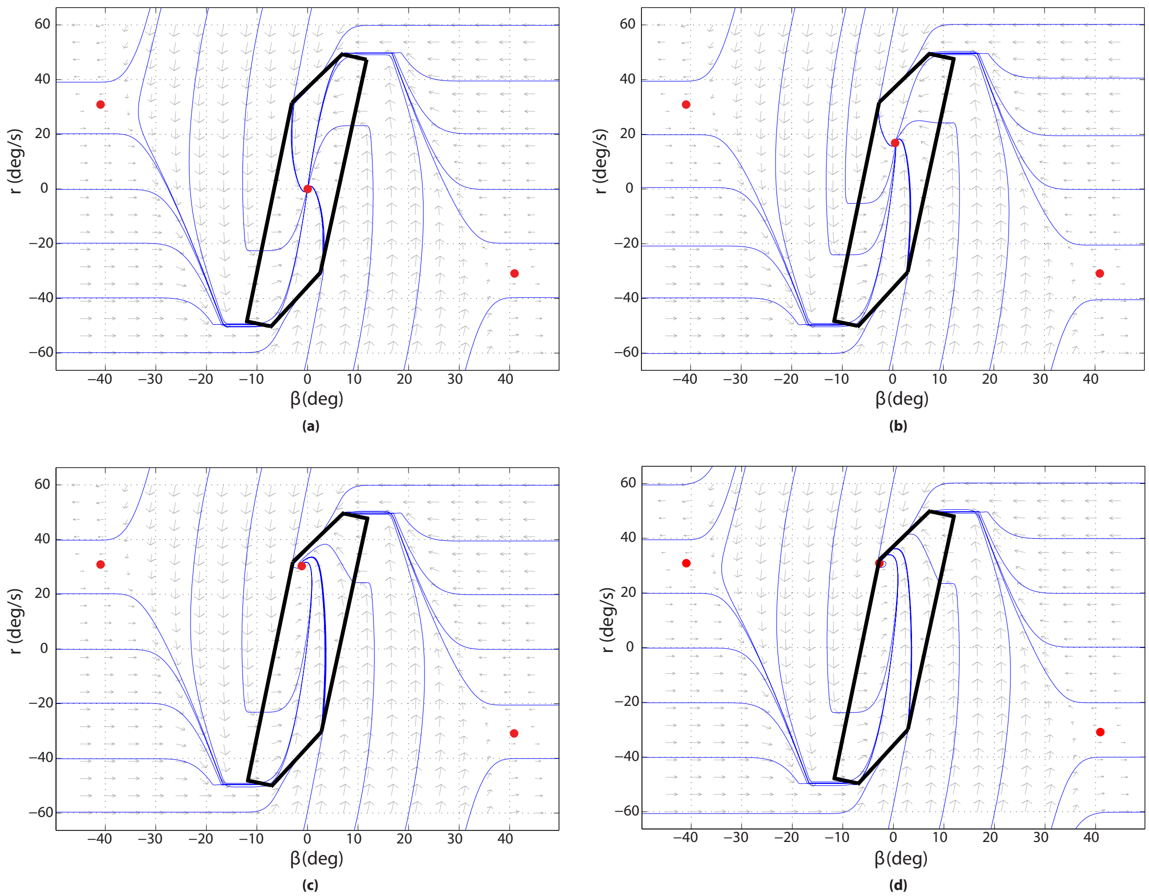

Figure 4.7: *Closed Loop Dynamics at (a) 0 Degrees (b) 5 Degrees (c) 10 Degrees (d) 15 Degrees of Steering*

closed loop is at high steering angles (15°), as the envelope controller successfully stabilizes the vehicle at the corner of the yaw rate and sideslip boundaries. The effects of the inner-boundary proportional controller are also seen, as the trajectories smoothly transition along the yaw rate boundary. The shape of the trajectories (especially those outside the sideslip boundaries) can be modified by the choice of controller gain K: the value of K for the plots shown is 20.

4.2 Experimental Results for Attractive Envelope Control

The following experiments detail the reaction of this envelope controller with inner boundary proportional control on the vehicle P1. The driving surface is gravel over concrete, with the friction coefficient widely varying between $0.4 - 0.7$. For the following tests, the controller assumes an average friction coefficient of 0.55. The gain and weighting for the distance S are set as $K = 20$ and $q = 0.3$. These values were chosen through experimentation to provide a good feel to the driver.

Figure 4.8 and Figure 4.9 represent data from a lift-off oversteer maneuver. P1 is a rear wheel drive electric vehicle that utilizes regenerative braking upon accelerator pedal lift-off. It is very easy to destabilize the vehicle using this type of maneuver, as the vehicle pitches forward with lift-off, and the remaining rear tire force goes towards regenerative braking. The goal of the controller, therefore, is to react quickly enough to stop the vehicle from spinning out. At $76.5s$ the driver completes a step steer of $20°$ at 10m/s, quickly followed by pedal lift-off. The plots of the two vehicle states show when each controller activates: light blue lines indicate that the vehicle is running in open loop; medium blue squares indicates that the proportional controller is active; dark blue squares indicates that Envelope Control is active, and the vehicle states are therefore outside the safe envelope. The action of the combined controller successfully holds the vehicle at the limits of handling by countersteering. The fact that the lateral acceleration is smooth (although noisy due to the widely varying friction) during the intervention indicates that the control action is not jarring to the driver, even though the maneuver requires a sudden, large control action. Figure 4.8 shows the value for S as the controller activates; S is limited to small values up to 1.5deg/s, which is equivalent to about four percent of the total yaw rate. Figure 4.9 gives the trajectory of the maneuver in the state space, with the vehicle envelope safe points denoted in black. The proportional controller keeps the vehicle within the safe area well; the Envelope Control only activates for a short time period.

Figure 4.10 and Figure 4.11 show the results for a slalom maneuver at 12m/s. The motion of the vehicle in the phase plane makes apparent the fact that the yaw rate

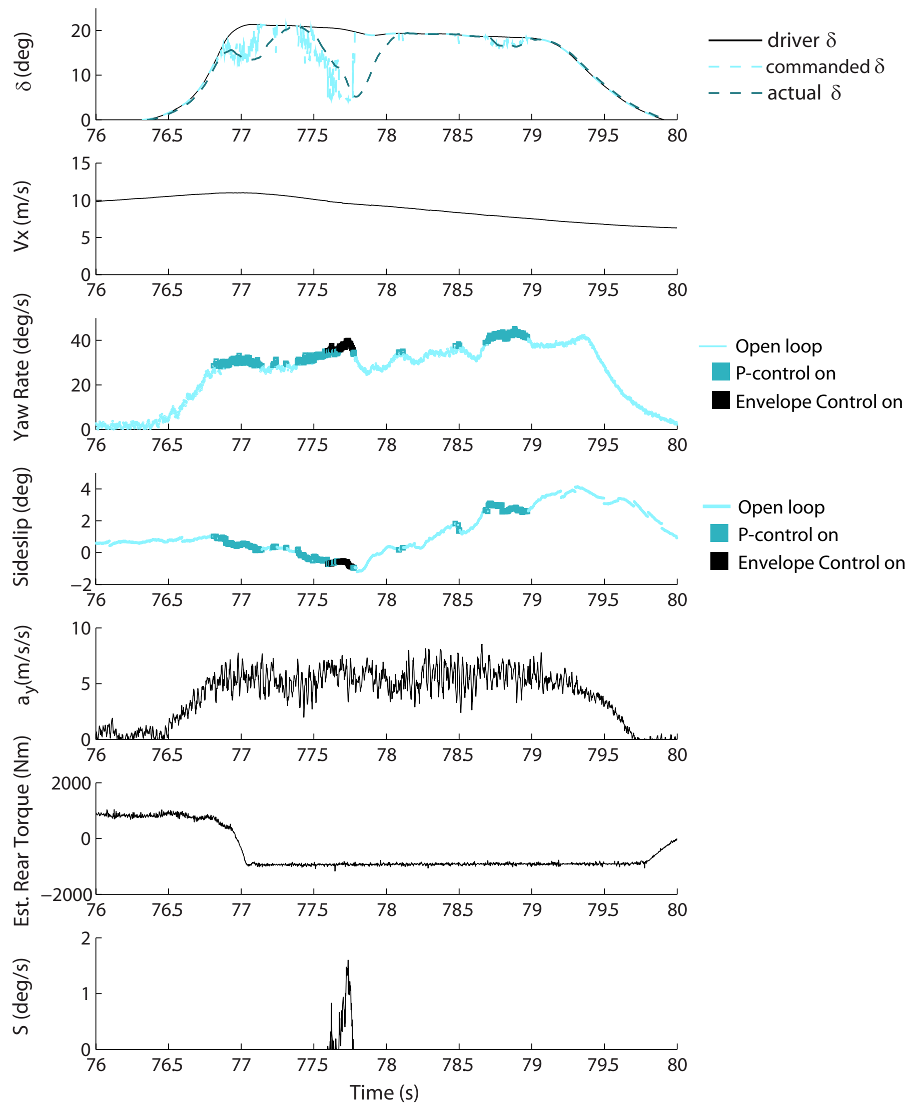

Figure 4.8: *Vehicle States for a Lift-Off Oversteer Maneuver Using Envelope Control*

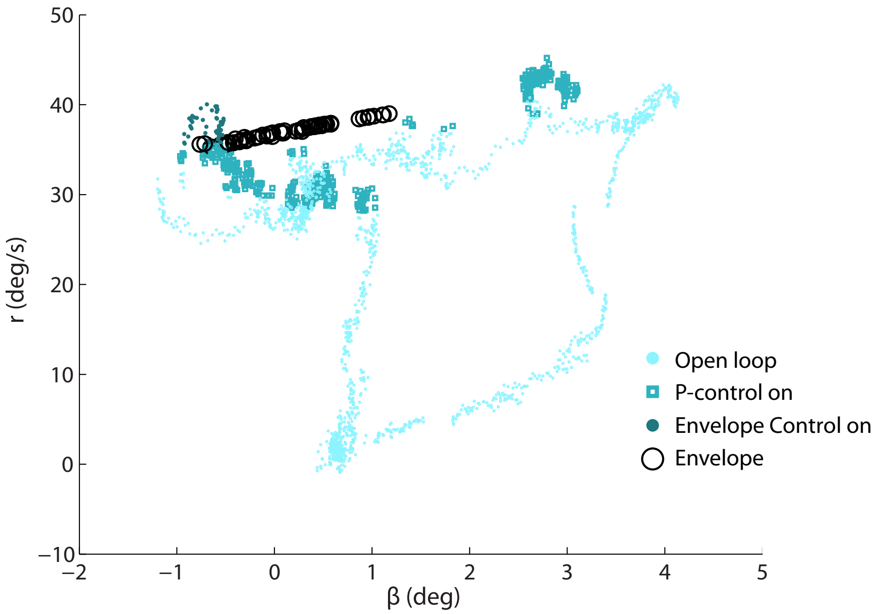

Figure 4.9: *Phase Plane View for a Lift-Off Oversteer Maneuver Using Envelope Control*

boundaries are reached first, with the vehicle largely staying away from the sideslip boundaries as a result. The controller activates small countersteers at the peak and trough of each sinusoid as the driver steers slightly past the maximum stable steering angle in each case. The resulting action of the vehicle is a smooth slalom, evidenced by the sinusoidal lateral acceleration, which reaches the limits at each peak and trough. S is again stable and limited to 2.5deg/s.

Finally, Figure 4.12 and Figure 4.13 show the results for a constant radius, increasing speed maneuver. In this experiment the driver holds a constant steering angle of approximately 16°. As the driver increases speed slowly, starting from 7m/s, the vehicle reaches the limits of handling, as evidenced by the near constant lateral acceleration. There are a few instances of the vehicle exiting the safe area between $49-51$s. In these cases, the steering angle is below the maximum stable steering angle for the given speed, so the proportional controller does not initiate. As the speed increases after 51s, the maximum stable steering angle is passed, and the proportional controller begins intervention before the Envelope Controller. The yaw rate variability during this test is a direct result of friction variation on the gravel surface. The open loop variability of the yaw rate can be seen at the beginning of the maneuver, when the controller is not yet intervening. As in the previous examples S is limited to 2.5deg/s, less than 5% of the maximum yaw rate; however, most of the interventions are well below that level.

There are a few reasons for S to grow slightly away from zero in these tests. Any modeling error (the highly varying friction for example) will result in the controller underreacting or overreacting slightly. The controller also does not take into account the slew rate of the steering motors; even though their reaction is fast compared to a human driver, there is still some lag compared to an instantaneous control command. The proportional controller mitigates this effect by smoothing the controller command near the boundary.

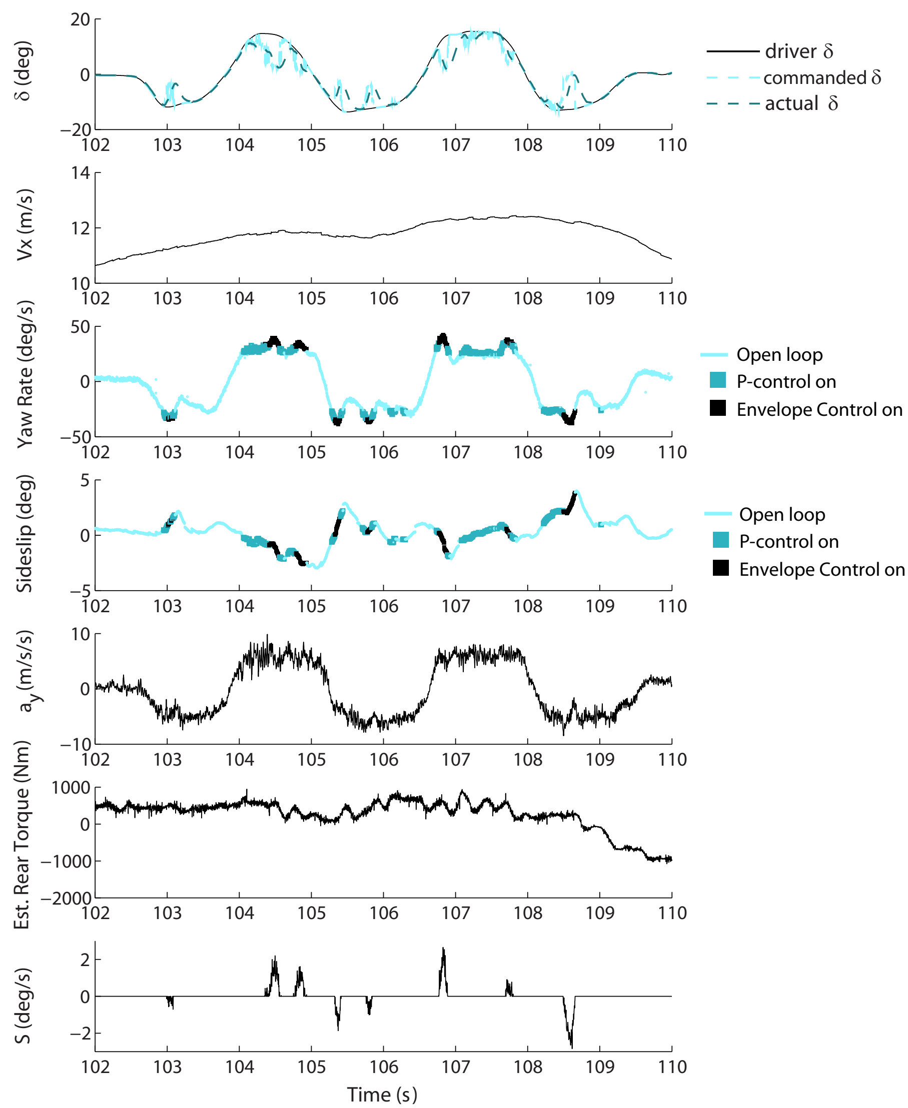

Figure 4.10: *Vehicle States for a Slalom Using Envelope Control*

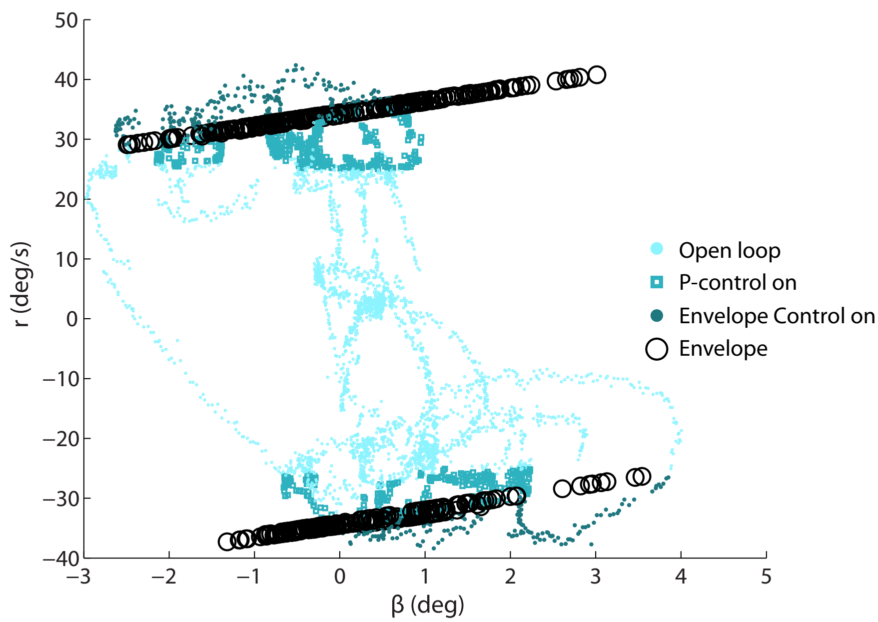

Figure 4.11: *Phase Plane View for a Slalom Using Envelope Control*

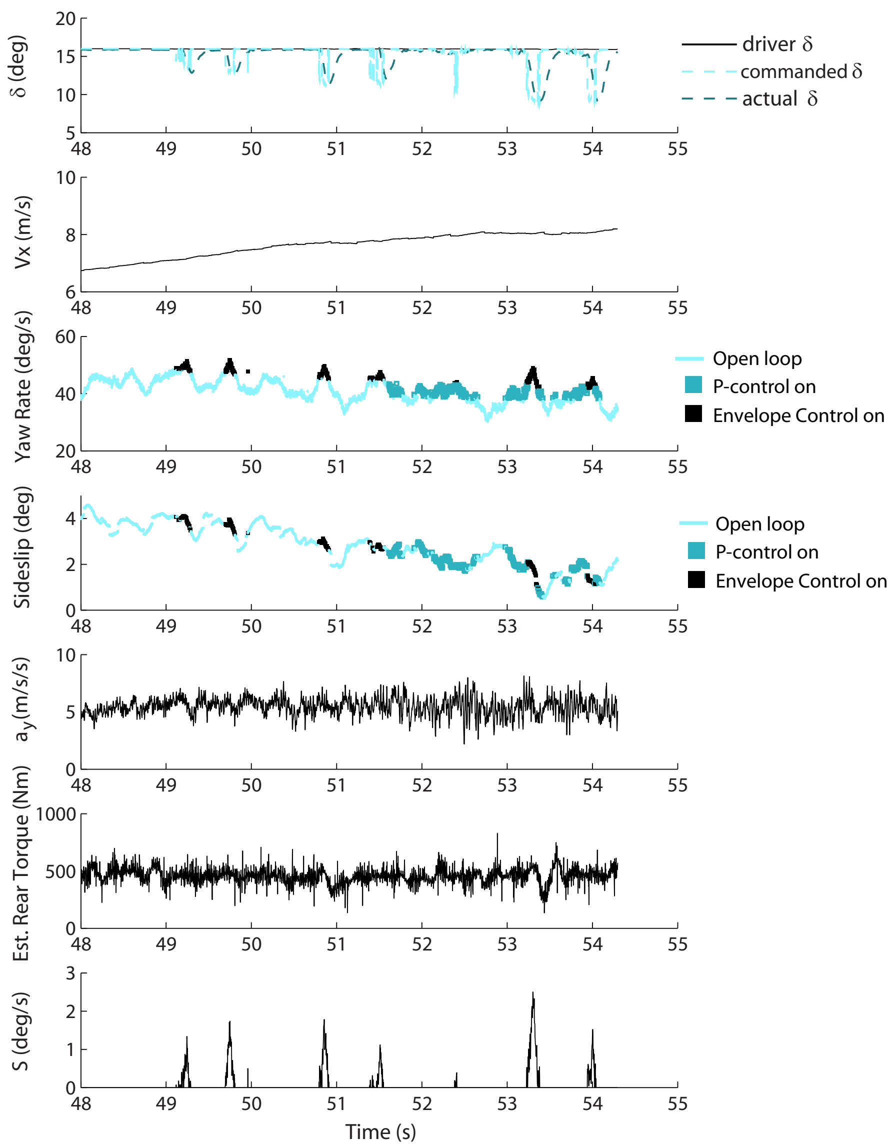

Figure 4.12: *Vehicle States for a Constant Radius Maneuver Using Envelope Control*

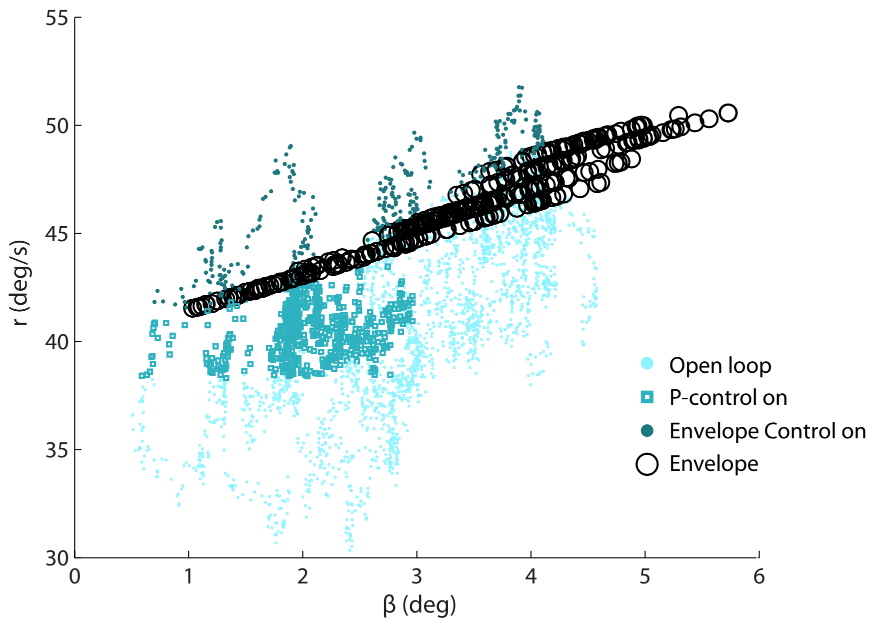

Figure 4.13: *Phase Plane View for a Constant Radius Maneuver Using Envelope Control*

Chapter 5

Suspension Design for Chassis Control

Although the previous chapter has shown that the Envelope Controller is successful for a given friction coefficient, real-time estimation of friction can aid in reassessing the boundaries at each time step. Given today's production sensing capabilities, detecting the limits of handling – determined by the maximum available tire force and the friction between the wheels and the ground – is a difficult problem. An experienced race car driver can estimate these values qualitatively by the feel of the steering torque (the total torque about the vehicle's steering axis): as the vehicle moves towards the limits of handling, the steering torque becomes higher until the tire forces are nearly saturated, at which point the torque decreases again. The race driver can feel this change from heavy to light steering, and thus knows when the front tires have reached the limits of lateral force generation.

Two previous incarnations of envelope control, given by Hsu [25] and Beal [6], have succeeded in integrating the controllers with a friction estimator based on aligning moment, which is one component of the steering torque. While the steering torque can be calculated by measuring the force through a load cell in the steering tierod, or from the motor current in a steer-by-wire or Electronic Power Steering system [60], the aligning moment must be separated out from the total measurement through estimation techniques. For example, Hsu's friction estimator is based on a nonlinear observer of pneumatic trail, a portion of the moment arm that produces aligning moment. In this estimation scheme, the algorithm must separate and discard irrelevant portions of the steering torque to reveal a value for the aligning moment; this manipulation of the measurement adds complexity to the estimation process, resulting in error.

Careful mechanical design of the suspension geometry can mitigate the development of these unwanted torque terms. The steering axis – through which the tire forces are translated – can be oriented to magnify the effects of the steering torque that contribute to friction and peak force estimation, while eliminating the effects that do not. Conventionally, the steering axis is oriented to provide a certain steering feel to the driver; in the case of a suspension designed for control, the suspension geometry is chosen to suit the control system rather than the driver. The driver's feel of the road can then be customized electronically using a separate force feedback module or an Electronic Power Steering system.

5.1 Suspension and Steering Geometry

There exist two major categories of suspension design for automotive applications: solid axle suspensions exhibit a rigid connection between the two wheels on an axle; independent suspensions allow each wheel to move without affecting the others. Solid axle suspensions are commonly used on heavy vehicles, and provide cost savings due to their small parts count. They do not provide much performance in terms of road holding, and the effect of each wheel on its partner makes it difficult to determine the specific reaction of forces at each wheel. Passenger car front suspensions are often independent configurations, like the MacPherson strut and double wishbone, because they provide more room for the engine, and offer more freedom to the designer in terms of kinematics.

5.1.1 Double Wishbone Geometry

In order to hold a large influence over the suspension kinematics at each corner, the presented design will be based on the geometry for a double wishbone configuration (also known as short-long arm). The double wishbone geometry has been present in road vehicles since as early as 1878 [16]. In this configuration, the wheel and knuckle are attached to the chassis by two control arms, forming a 4-bar linkage. As the name "short-long arm" suggests, the upper control arm is generally shorter than the lower to provide a desirable change in camber as the suspension moves in bump or rebound. A coil-over shock is usually attached to the larger and longer lower control arm to provide spring and damping forces between the wheel and the chassis.

The relevant hardpoints for the suspension are shown in Figure 5.1. The upper control arm inner and outer balljoints are designated as UIBJ and UOBJ; the control arms generally take a fork or 'A' shape, resulting in one outer balljoint, and two inner balljoints. The lower control arm inner and outer balljoints are designated as LIBJ and LOBJ. The upper and lower outer balljoints of the control arms determine the steering axis, about which the wheel is free to rotate. The steering tierod inner and outer balljoints are designated as ITRBJ and OTRBJ.

Figure 5.2 shows the geometry of the suspension at the wheel, which is determined by the position of the outer control arm joints. These values are given at nominal ride height and zero steering angle. The suspension design dictates the following relevant parameters: wheel radius (R_w), caster angle (θ_c), kingpin angle (θ_k), scrub radius (d), and mechanical trail (t_m).

Kingpin angle and mechanical trail are normally tuned to give a return-to-center feel to the driver by inducing a restoring torque in response to the development of lateral force on the tire. Caster angle provides directional stability while the vehicle is moving and contributes to road feel through damping of the steering angle. Scrub radius is generally small to limit the amount of braking torque transferred to the driver through the steering wheel; a small or slightly negative scrub radius also contributes to high speed steering stability since there is less sensitivity to brake inputs [37]. While zero scrub radius seems preferable, it can cause steering difficulty at low speed as the contact patch must spin in place instead of scrubbing as the wheel turns. Table 5.1

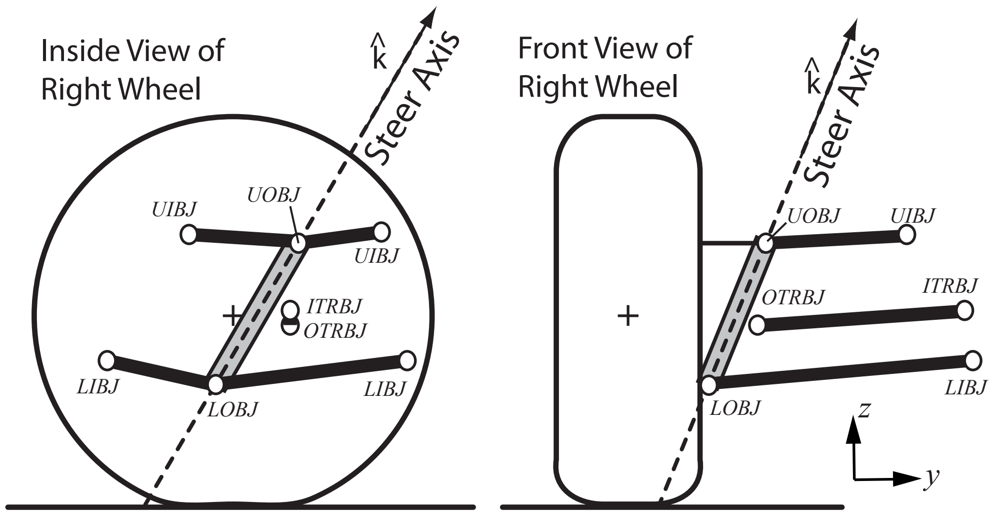

Figure 5.1: *Double Wishbone Suspension Geometry: Right Wheel*

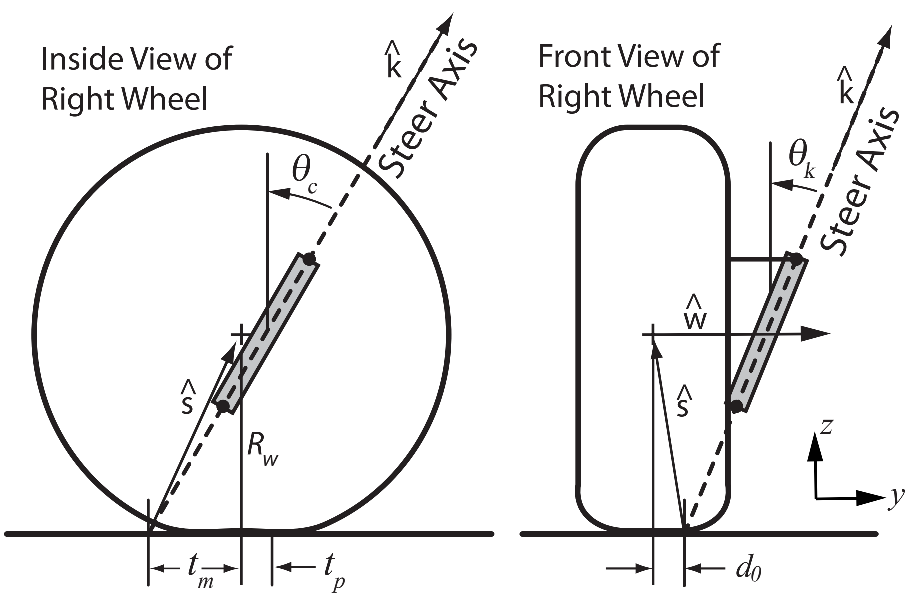

Figure 5.2: *Suspension Geometry Parameters: Right Wheel*

gives typical values for these suspension parameters as seen in passenger cars, along with specific values from the 1997 Corvette C5 and Stanford's P1. P1's parameters fall within the typical ranges for all the given values. Pictures of P1's suspension can be found in Figure 5.3.

Table 5.1: Suspension Parameter Comparison

Parameters at Zero Steer		Typical Values	1997 Corvette C5 [20]	P1 Design
Wheel Radius	mm	300 to 350	325	320
Caster Angle	degrees	4 to 7	6.5	5.5
Kingpin Angle	degrees	7 to 15	8.8	13.2
Scrub Radius	mm	-75 to 75	12	50.5
Mechanical Trail	mm	15 to 50	36	28

5.1.2 Steering Geometry

Most passenger vehicles today operate with a rack and pinion steering system. In this configuration, the handwheel is mechanically linked to a steering gearbox through a series of shafts and universal joints. Within the gearbox, the rack and pinion turn the rotational motion of the handwheel into a translational motion of the steering linkages. The rack connects to steering tierods at either end, which in turn connect to either wheel through a steering arm. The steering arm is rigidly connected to the suspension knuckle and therefore to the wheel. Figure 5.4 illustrates a rack and pinion steering system in a rear-steering configuration, meaning that the steering linkages are located behind the wheel center. On the rear axle of the vehicle, which is typically not steered, the tierod (also known as a toe link for non-steered wheels) inner balljoints are rigidly connected to the chassis instead of a rack.

Figure 5.4 also shows the configuration of a steer-by-wire system in which each wheel is independently controlled, as is the case on P1. For this specific system, there is no connection between the handwheel and either roadwheel. Instead, a motor and harmonic drive pair control the angle of a pitman arm connected to each inner tierod

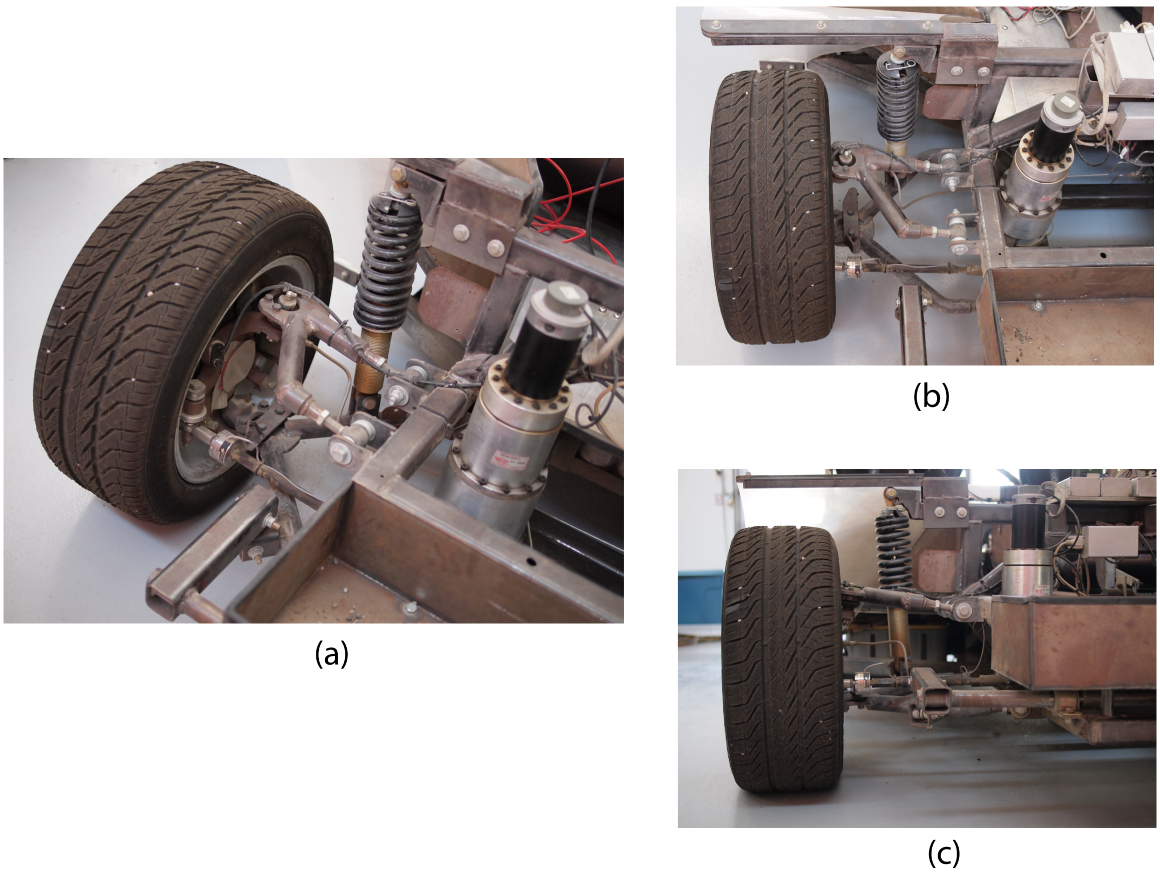

Figure 5.3: *P1's Double Wishbone Suspension, (a) Inside View of the Front Right Wheel, (b) Top View, (c) Front View*

balljoint. At the handwheel, a potentiometer and encoder sense the driver's steering input, and a motor can direct force feedback to the driver. In the case of some newer passenger car models, the Electronic Power Steering system may be able to apply an additional torque to the handwheel to augment what the driver feels; however, the road wheels are still connected by the rack.

For vehicle control, knowing the precise steering angle of the wheels is important in determining both the vehicle dynamics and the tire forces or steering torque. Depending on the design of the steering tierod geometry, vertical movement of the suspension can cause the wheels to turn in or out, even if the driver is not moving the steering wheel. This movement is known as bump or roll steer: bump steer is the change in wheel angle (or toe angle) caused by vertical suspension travel; roll steer is differential bump steer between the wheels on one axle. The elimination of this effect results in a more predictable steering angle, which is desirable for control and estimation purposes. Correct placement of the inner tierod balljoint is critical to achieving the desired bump and roll steer characteristics.

To design the correct placement of the ITRBJ, the OTRBJ placement should be determined based on the packaging constraints of the suspension. As a first iteration, the tierod length can be found by measuring the horizontal distance from the steering axis to the line through the inner control arm balljoints at the height of the outer tie rod ball joint. If this distance is then translated horizontally to begin at the OTRBJ, and rotated to become collinear with the line to the instantaneous center of rotation (I.C.) of the control arms, the ITRBJ is defined by the position of the end of the line. This process is illustrated in Figure 5.5, where the chosen position for the ITRBJ is denoted by a black circle. This method should result in a geometry where the OTRBJ does not move much laterally (thus steering the wheel) when the suspension is in bump or rebound, because the tierod and control arms will move together about the same instantaneous center. Due to the complexity of the geometry, and the need for precision in steering, the exact placement of the inner tierod balljoint can then be adjusted in software; a program like MSC.ADAMS or Lotus Shark can evaluate the kinematics of the system, showing the exact amount of bump and roll steer present for a given tierod position. Even adjustments as small as 1mm in ITRBJ height or

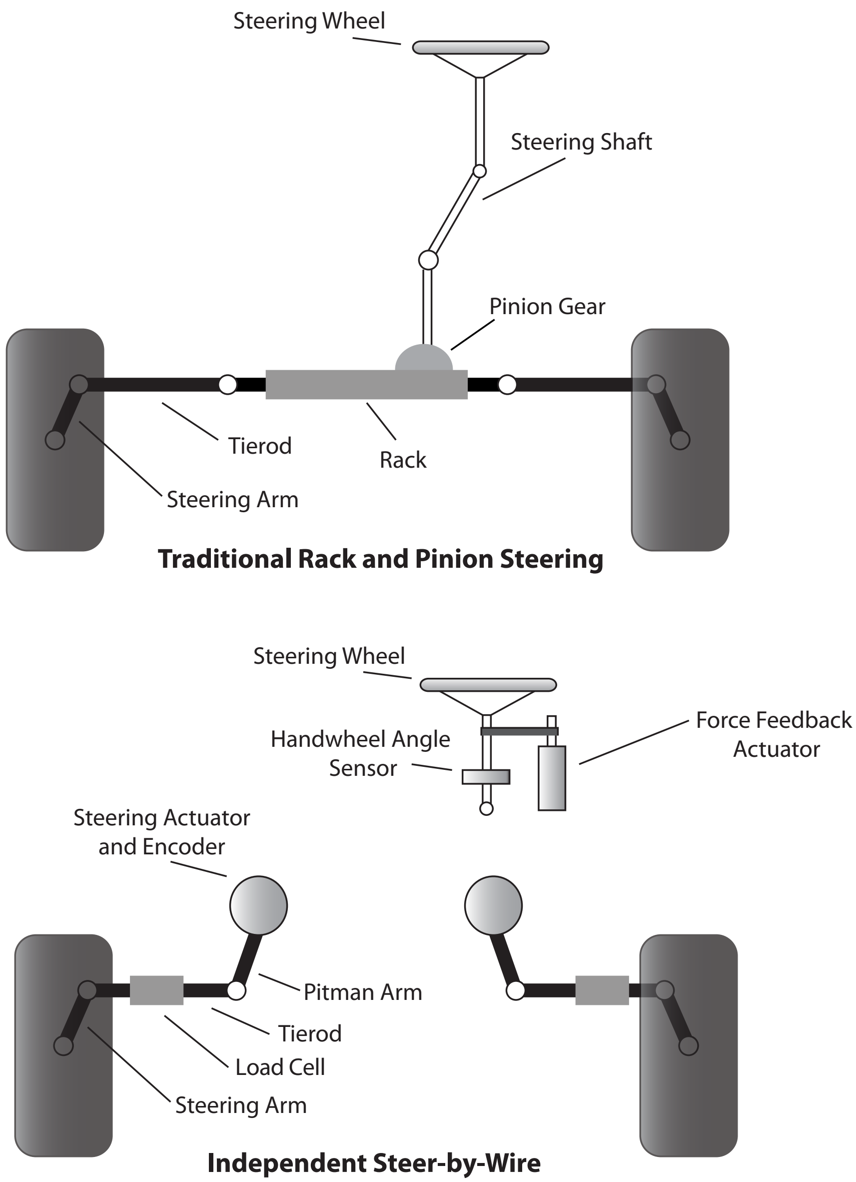

Figure 5.4: *Top View of a Traditional Rack and Pinion versus Steer-by-Wire Configuration*

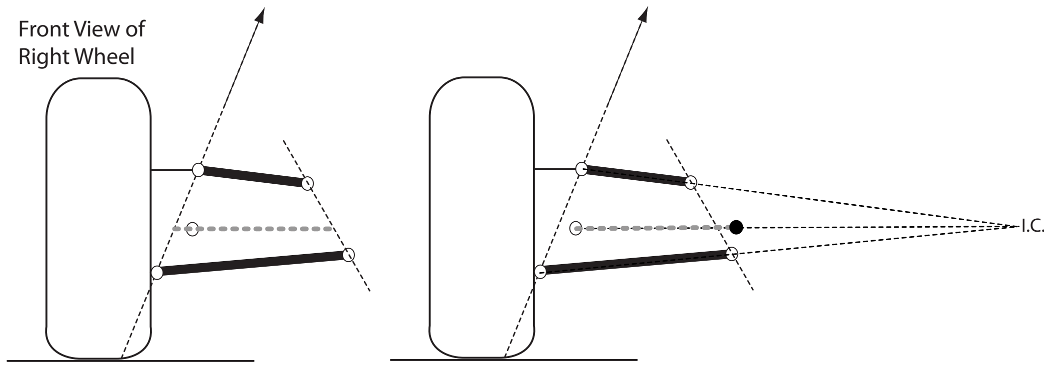

Figure 5.5: *Initial Tierod Placement for Zero Bump and Roll Steer*

5mm in lateral position can have an effect on the steering motion. Adjustments along the longitudinal axis of the vehicle do not have as much impact.

5.2 The Components of Steer-Axis Reaction Torque

The torque about the steering axis, called the steer-axis reaction torque, gives the attentive driver information about the lateral limits of the vehicle. This torque is comprised of three main contributors from the road-wheel interface: jacking torque (τ_j), the moment produced by vertical tire forces; aligning moment (τ_a), the moment produced by lateral tire forces through mechanical trail and pneumatic trail; and scrub radius torque, the moment produced by longitudinal tire forces through scrub radius (τ_s). In a typical vehicle, the torque that the driver exerts on the steering wheel is transmitted to the steering axis; however, this torque does not reach the steering axis in a steer-by-wire vehicle since the steering wheel is mechanically isolated. For a steer-by-wire system like P1's, there is instead a torque arising from the actuators (τ_{act}), so the total steer-axis reaction torque is expressed as follows:

$$\tau_{SART} = \tau_a + \tau_j + \tau_s + \tau_{act} \quad (5.1)$$

$$= J_{eff}\ddot{\delta} + b_{eff}\dot{\delta} - sgn(\dot{\delta})F_{coulomb} \quad (5.2)$$

where J_{eff} and b_{eff} represent the effective inertia and damping of the steering system, and $F_{coulomb}$ is the coulomb friction of the steering system. The inertia, damping, and friction of the steering system can be identified a priori using system identification techniques.

5.2.1 Aligning Moment

The aligning moment (τ_a) is the component of the steer axis reaction torque due to lateral tire forces. The lateral tire forces are reacted through two moment arms: mechanical trail, which is defined by the suspension geometry, and pneumatic trail, the distance between the resultant point of lateral force application and the center of the tire (Figure 5.2). The addition of pneumatic and mechanical trail results in a quantity called the total trail. In traditional steering systems, total trail induces restoring torque as the wheel is steered, producing a 'return-to-center' feel for the driver. In a steer-by-wire system, this feel must be given to the driver through force-feedback; however, the restoring torque on the road wheel remains to help the wheels return to center as the steering is zeroed.

The pneumatic trail is a function of slip angle. For the parabolic force distribution and single coefficient of friction assumed by the lateral brush tire model, the pneumatic trail is defined as follows, where α_{sl} is the slip angle corresponding to peak tire force, and l is the length of the tire contact patch:

$$t_p = \begin{cases} \frac{l}{6}\frac{1-3|\theta_y\sigma_y|+3(\theta_y\sigma_y)^2-|\theta_y\sigma_y|^3}{1-|\theta_y\sigma_y|+\frac{1}{3}(\theta_y\sigma_y)^2} & |\alpha| \leq \alpha_{sl} \\ 0 & |\alpha| > \alpha_{sl} \end{cases} \tag{5.3}$$

$$\theta_y = \frac{C_\alpha}{3\mu F_z} \tag{5.4}$$

$$\sigma_y = \tan(\alpha) \tag{5.5}$$

This relationship gives the initial value of pneumatic trail to be $\frac{l}{6}$; however, in practice the initial pneumatic trail is closer to $\frac{l}{4}$ due to the elasticity of the tire material [42].

A simpler, linear representation of the pneumatic trail captures the main trend of the above model, starting with an initial length t_{po}, and vanishing to zero with total tire saturation. The calculations of pneumatic trail in this chapter use this linear model.

$$t_p = \begin{cases} t_{po} - \frac{t_{po} C_\alpha}{3\mu F_z} |\tan(\alpha)| & |\alpha| \leq \alpha_{sl} \\ 0 & |\alpha| > \alpha_{sl} \end{cases} \tag{5.6}$$

Determining the mechanical trail relies on an understanding of the suspension kinematics. Two reference frames are required to define the suspension geometry as the wheel is steered. The first reference frame, $\mathcal{N}$, is centered at the wheel center and aligned with the chassis, so that the $\hat{\mathbf{n_x}}$ axis points forward along the longitudinal axis of the car, $\hat{\mathbf{n_y}}$ points left along the lateral axis of the car, and the $\hat{\mathbf{n_z}}$ axis points upwards. The second reference frame, $\mathcal{R}$, is also centered at the wheel center, but is aligned with the wheel as it steers and cambers. Here the $\hat{\mathbf{r_x}}$ axis points forward along the longitudinal axis of the tire and $\hat{\mathbf{r_y}}$ points left along the lateral axis of the tire. The steering (kingpin) axis, shown in Figure 5.2 as $\hat{\mathbf{k}}$, is defined by the kingpin angle and caster angle at zero steering. $P(\delta)$ gives the rotation of the wheel about the steering axis due to steering angle, from $\mathcal{N}$ to $\mathcal{R}$. Note that the calculations in this derivation pertain to the left wheel.

$$\hat{\mathbf{k}} = \frac{1}{\sqrt{\tan^2\theta_c + \tan^2\theta_k + 1}} \begin{bmatrix} -\tan\theta_c \\ -\tan\theta_k \\ 1 \end{bmatrix} \tag{5.7}$$

$$= \begin{bmatrix} k_x \\ k_y \\ k_z \end{bmatrix} \tag{5.8}$$

$$P(\delta) = (1-\cos\delta)\hat{\mathbf{k}}\hat{\mathbf{k}}^T + \begin{bmatrix} \cos\delta & -k_z\sin\delta & k_y\sin\delta \\ k_z\sin\delta & \cos\delta & -k_x\sin\delta \\ -k_y\sin\delta & k_x\sin\delta & \cos\delta \end{bmatrix} \tag{5.9}$$

Also shown in Figure 5.2 is $\hat{\mathbf{w}}$, the unit vector which defines the lateral orientation of the wheel as a function of camber and steering angle; this vector is directed in line with the wheel axle. $\hat{\mathbf{x_g}}$ and $\hat{\mathbf{y_g}}$ are the longitudinal and lateral unit vectors of the rotated wheel in the ground plane.

$$\hat{\mathbf{w}} = P(\delta)\hat{\mathbf{n_y}} \tag{5.10}$$

$$\hat{\mathbf{y_g}} = \frac{\hat{\mathbf{w}} - (\hat{\mathbf{w}}^T\hat{\mathbf{n_z}})\hat{\mathbf{n_z}}}{\|\hat{\mathbf{w}} - (\hat{\mathbf{w}}^T\hat{\mathbf{n_z}})\hat{\mathbf{n_z}}\|} \tag{5.11}$$

$$\hat{\mathbf{x_g}} = \hat{\mathbf{y_g}} \times \hat{\mathbf{n_z}} \tag{5.12}$$

Equation 5.13 and Figure 5.2 define $\vec{\mathbf{s}}$ in $\mathcal{R}$, the location of the wheel center with respect to the steering axis intersection with the ground. For this calculation, d_o is the scrub radius at zero steering and nominal ride height. $\vec{\mathbf{l}}$ in $\mathcal{R}$ defines the location of the contact patch center with respect to the steering axis intersection with the ground; this vector lies in the ground plane. The mechanical trail is defined as the component of $\vec{\mathbf{l}}$ that lies in the direction of $\hat{\mathbf{x_g}}$.

$$\vec{\mathbf{s}} = P(\delta)\left[-R_w \tan\theta_c \quad d_o \quad R_w\right]^T \tag{5.13}$$

$$\vec{\mathbf{l}} = \vec{\mathbf{s}} - R_w(\hat{\mathbf{x_g}} \times \hat{\mathbf{w}}) \tag{5.14}$$

$$t_m(\delta) = \vec{\mathbf{l}} \cdot \hat{\mathbf{x_g}} \tag{5.15}$$

Finally, Equation 5.16 gives the torque component resulting from a lateral tire force and total trail that is felt about the steering axis.

$$\tau_a = \hat{\mathbf{k}} \cdot (-(t_p + t_m(\delta))\hat{\mathbf{x_g}} \times F_y\hat{\mathbf{y_g}}) \tag{5.16}$$

In this equation, both pneumatic trail and lateral force are functions of the vehicle's lateral limits of handling, defined by the peak lateral tire force. As discussed by Hsu [26], a tire's aligning moment reaches its peak at a slip angle corresponding to approximately half of the peak lateral force; thus, the aligning moment can indicate the limits of the tires well before peak force is reached. Figure 5.6 illustrates this characteristic of the aligning moment, in comparison to the lateral force and pneumatic trail as they change with slip angle.

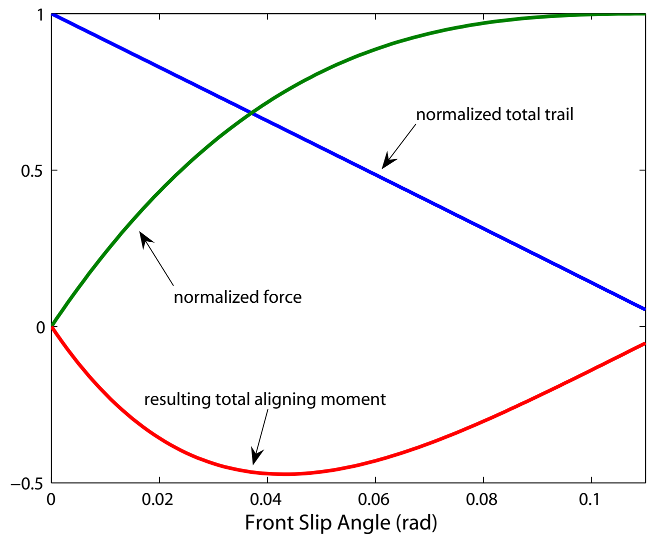

Figure 5.6: *Normalized Aligning Moment, Total Trail, and Lateral Force with Respect to Slip Angle (with $t_m = 0$)*

5.2.2 Jacking Torque

Jacking torque is the torque resulting from normal force about the steering axis, which manifests as a change in ride height as the wheels turn in or out. τ_j is thus a function of steer angle (δ) and tire normal force (F_z), given by Equations 5.8, 5.9, 5.14, and the equation below:

$$\tau_j = \hat{\mathbf{k}} \cdot (\vec{\mathbf{l}} \times F_z \hat{\mathbf{n_z}}) \tag{5.17}$$

At high steering angles and low speed, this effect can dominate the steer-axis reaction torque. The vertical jacking of the suspension is most noticeable while parking, since the vehicle is moving very slowly and making large wheel movements. If the left and right wheels of the vehicle are linked through a steering rack, the jacking torques of each wheel counteract each other for small steering angles. This counteraction does not exist in steer-by-wire vehicles like P1.

5.2.3 Scrub Radius Torque

Scrub radius torque is the component of torque about the steering axis resulting from longitudinal tire forces acting through the scrub radius:

$$d = \vec{\mathbf{l}} \cdot \hat{\mathbf{y}}_{\mathbf{g}} \tag{5.18}$$

$$\tau_s = \hat{\mathbf{k}} \cdot (d\hat{\mathbf{y}}_{\mathbf{g}} \times F_x\hat{\mathbf{x}}_{\mathbf{g}}) \tag{5.19}$$

where τ_s is scrub radius torque, and d is the scrub radius. The kingpin axis $\hat{\mathbf{k}}$, the longitudinal axis of the wheel $\hat{\mathbf{x}}_{\mathbf{g}}$, and the contact patch location $\vec{\mathbf{l}}$ are given in Equation 5.8, Equation 5.11, and Equation 5.14, respectively.

In a traditional steering system where both wheels are linked through the rack, the contributions of the scrub radius torque from the left and right sides cancel each other. Scrub radius is designed into a suspension system to reduce tire wear and reduce actuator (or human) effort to steer at low speeds; the scrub radius provides a radius about which the wheel can rotate to steer.

5.2.4 Actuator Torque

The source of actuator torque about the steering axis varies with the steering system design. In current production vehicles, the actuator is most often the human driver exerting a torque on the steering wheel, which is translated through the steering system. Electronic Power Steering systems can add or subtract from the driver's input torque as well. In an independent steer-by-wire system, the torque from each steering actuation motor contributes to the steer-axis reaction torque; however, the driver's input torque is completely decoupled. Because of this decoupling, the actuator torque in a steer-by-wire system can be measured through the steering motor current. A more general approach to measuring actuator torque (usable even without EPS or steer-by-wire) is to measure the force through the steering tierod with a load cell. The general placement of the load cell on P1 is shown in Figure 5.4. The actuator torque, as measured through the load cell, is given by the following equation, where $\vec{\mathbf{r}}_{\mathbf{motor,loadcell}}$ is the moment arm from the steering motor to the loadcell, $\vec{\mathbf{r}}_{\mathbf{KPA,motor}}$

is the moment arm from the kingpin axis to the steering motor, and $\vec{\mathbf{F}}_{\mathbf{loadcell}}$ is the measured force in the loadcell:

$$\tau_{act} = (\vec{\mathbf{r}}_{\mathbf{motor,loadcell}} + \vec{\mathbf{r}}_{\mathbf{KPA,motor}}) \times \vec{\mathbf{F}}_{\mathbf{loadcell}} \tag{5.20}$$

An alternative version of this equation uses the linkage ratio n_l between the pitman arm angle θ and the steer angle of the wheel δ to determine the transmission of torque from the motor axis to the steering axis:

$$n_l(\delta) = \frac{d\theta(\delta)}{d\delta} \tag{5.21}$$

$$\tau_{act} = n_l(\vec{\mathbf{r}}_{\mathbf{motor,loadcell}} \times \vec{\mathbf{F}}_{\mathbf{loadcell}}) \tag{5.22}$$

5.3 Using Aligning Moment to Estimate Friction and Peak Tire Forces

Early estimation of friction and peak tire force, before the limits are reached, allows a chassis control system to work more reliably and proactively. In the case of vehicle envelope control, as presented in the previous chapter, real-time friction estimation permits updates to the boundary size at every timestep, and results in a more accurate calculation of lateral tire force. Because aligning moment decreases well before tire force saturation (due to its dependence on pneumatic trail), several approaches have been taken to improve vehicle stability by limiting driver steering input once algorithms detect a noticeable decrease in aligning moment [58, 40, 18].

The pneumatic trail also gives early indication of the friction coefficient. Figure 5.7 compares the normalized lateral tire force and the normalized pneumatic trail versus slip angle for several friction coefficients. No matter which friction coefficient is chosen, the lateral tire forces for low slip angles are indistinguishable from one another; however, the pneumatic trail curves are unique to a given friction, even at the lowest slip angles. This property of the pneumatic trail allows the control system to estimate the friction coefficient with little lateral excitation.

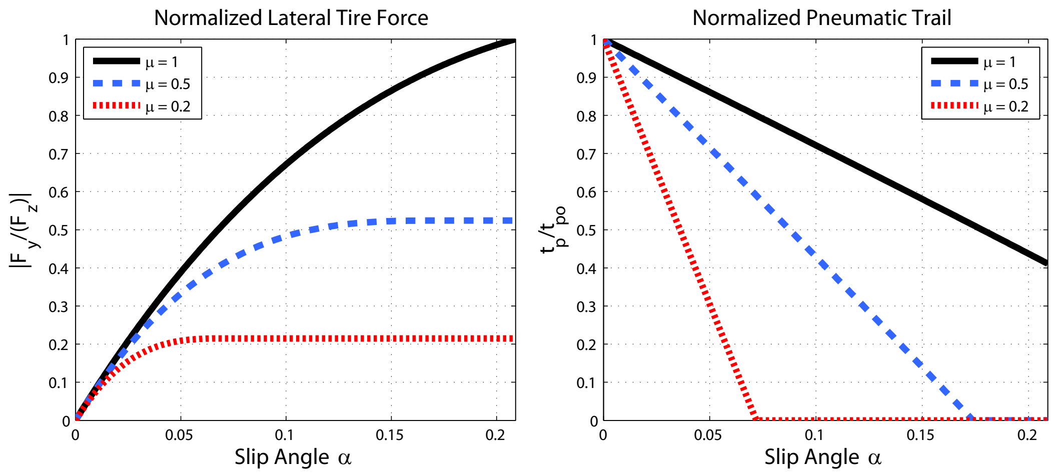

Figure 5.7: *Normalized Pneumatic Trail and Lateral Tire Force for Varying Frictions*

Hsu and Beal, who have successfully integrated friction estimation with envelope control algorithms on P1, both take advantage of the properties of pneumatic trail to gain friction information at low slip angles [25, 6]. To do so, they measure the total steer-axis reaction torque using a load cell located in each steering tierod, then subtract out the steering dynamics, jacking torque, and scrub radius torque to obtain the aligning moment, and thus the pneumatic trail. While their estimation schemes work well in experiment, they require robust models of the vehicle's jacking characteristics and longitudinal tire forces. The process can be simplified by slightly changing the mechanical design of the suspension.

5.4 Suspension Design Requirements for Enhanced Friction Estimation

P1's successor, called X1, exhibits a suspension designed specially for the purpose of enhanced friction estimation. X1, like P1, has an independent steer-by-wire system and a double-wishbone suspension. Figure 5.8 gives several views of the front right corner of the car. The upper and lower control arm are easily spotted in red, with the steering tierod between them in silver.

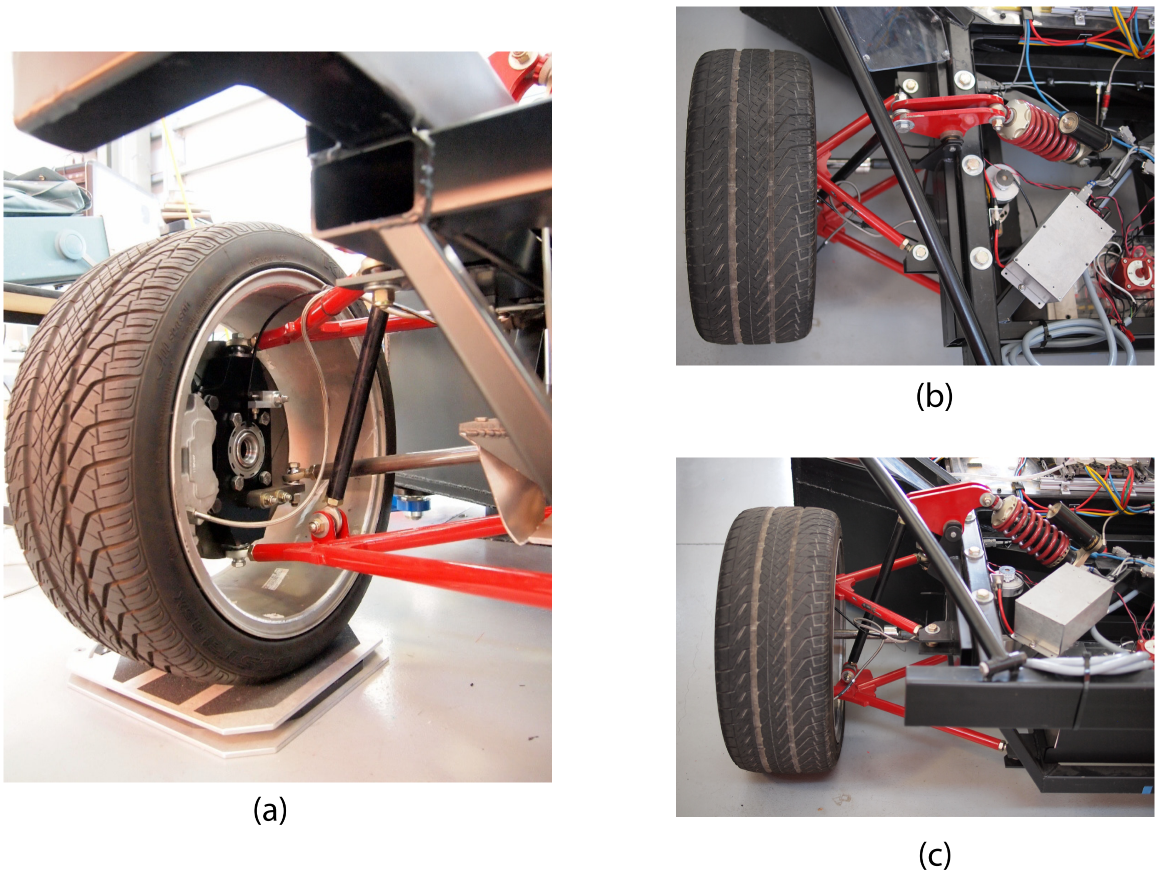

Figure 5.8: *X1's Double Wishbone Suspension, (a) Inside View of the Front Right Wheel, (b) Top View, (c) Front View*

The first goal in X1's suspension design is to simplify the measurement of aligning moment by eliminating the contributions of jacking torque and scrub radius torque to the steer-axis reaction torque. The fourth contributor to steer-axis reaction torque, the steering dynamics, cannot be eliminated, but can be well characterized with system identification techniques. As indicated by Equation 5.17, a smaller kingpin angle significantly reduces the effects of suspension jacking on the steer-axis reaction torque. For this reason, X1 has a nominal kingpin angle of 0°. Ideally, a kingpin angle of zero should eliminate the effects of jacking torque from the steer-axis reaction torque; however, the kingpin angle can change with suspension travel due to the control arm geometry, so some small amount of jacking torque may be introduced in bump. X1's control arms are as long as possible given packaging constraints to minimize this effect, with their proportional lengths determined to provide favorable camber change and decrease lateral roll center motion. A comparison of the jacking torque characteristics on P1 and X1 is shown in Figure 5.9. With a maximum steer-axis reaction torque of approximately 300Nm per wheel, the jacking torque on P1 can contribute significantly to the measured torque, while X1's is basically zero.

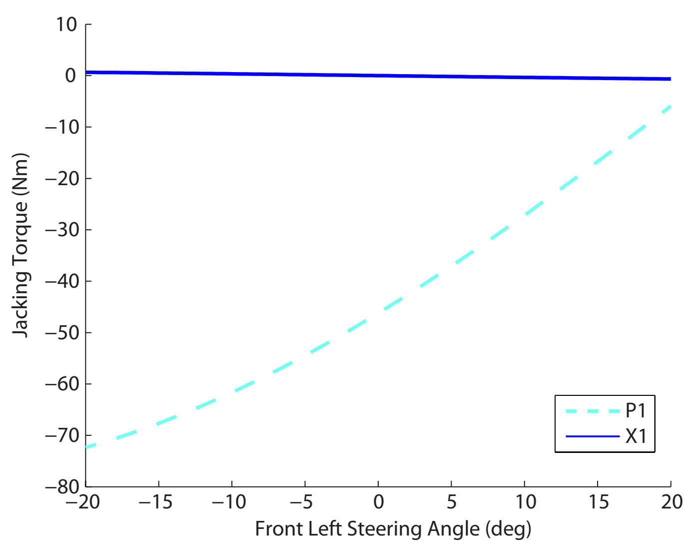

Figure 5.9: *Jacking Torque for the Front Left Wheel at Nominal Vertical Load*

The contribution of longitudinal tire forces to the steer-axis reaction torque is reduced by decreasing the scrub radius. X1's nominal scrub radius is 0mm, thereby eliminating the scrub radius torque. While decreasing the kingpin angle and scrub radius to zero seems ideal, this does lead to difficulties in packaging, as both outer control arm balljoints must lie on the centerline of the tire. Both balljoints fit within the wheel to fulfill the design on X1; however, a tall knuckle design, where the upper outer balljoint sits high above the wheel, is also highly practical.

After significantly decreasing the contributions of jacking torque and scrub radius torque, the steer-axis reaction torque only reflects contributions from the aligning moment and the steering dynamics, making it simple to determine the aligning moment from the torque measurement. From aligning moment, the pneumatic trail is more easily determined if the mechanical trail is constant. X1's low kingpin angle induces very little mechanical trail change. Figure 5.10 shows the drastic difference in mechanical trail change with steering between P1 and X1. At nominal ride height, P1, with a kingpin angle of 13.2°, has a mechanical trail variance with steering between -15mm and 60mm. As the mechanical trail passes through zero, the vehicle states are rendered unobservable from the perspective of aligning moment, so this trait should be avoided [32]. For this reason, X1's mechanical trail only varies between 10mm and 13mm over the full range of steering, avoiding zero, and remaining within a few millimeters of the nominal value.

Figure 5.11 further highlights the advantages of a low kingpin angle by comparing the mechanical trail change of P1 and X1 in bump for a variety of steering angles. X1's mechanical trail has a highly decreased range in terms of absolute value over all steering angles and all levels of suspension travel. Packaging limitations on the control arm lengths do lead to minor changes in the kingpin angle during suspension travel, which prevents X1's mechanical trail change from decreasing further. The nominal size of the mechanical trail is a tradeoff: a small mechanical trail like X1's makes the change in pneumatic trail more apparent; a large mechanical trail provides more stabilizing force to return the wheel to center in the event of an actuator failure.

The last requirement for X1's design (and P1's as well) is elimination of bump and roll steer by correct placement of the steering tierod. The desired specification limits

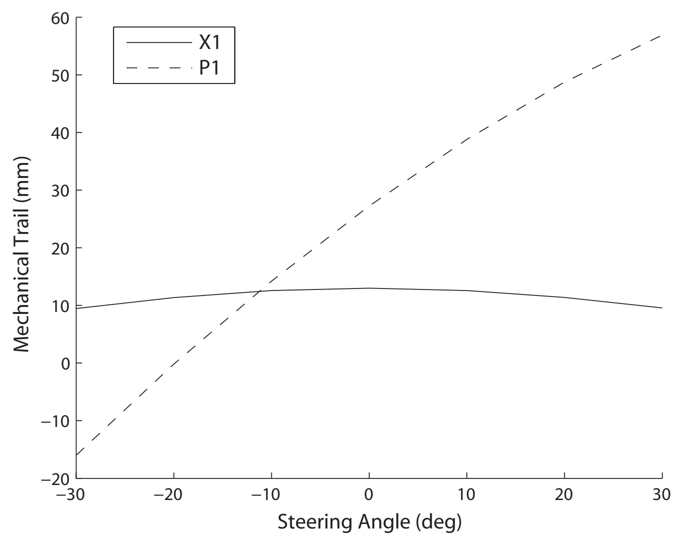

Figure 5.10: *Mechanical Trail Change with Steering at Nominal Ride Height*

the toe angle change to 0.25° over the travel of the suspension from nominal to either extreme. Figure 5.12 shows theoretical results (from Lotus Shark) versus experimental data gathered from a laser measuring system. Both wheels on the front axle exhibit the desired characteristics, and match the theoretical results well; the disparities are likely due to small manufacturing errors within the suspension linkages.

Unlike P1, X1 has four wheel independent steer-by-wire. The rear suspension for X1 meets the same design requirements as the front, so that each wheel can be steered, and each wheel can sense friction through the aligning moment measurements. Because the rear axle is driven, however, the packaging constraints are more difficult to fulfill. On both axles, the coil-over shock, normally attached to the lower control arm, is instead mounted at the center of the vehicle (above and inboard of the suspension) and driven by a pushrod attached to the lower control arm. The rear axle pushrods have a forked design to accommodate the drive axle. Additionally, the rear pitman arms are oriented differently than the front to provide space for the drive motor. Figure 5.13 compares the front and rear suspensions, focusing on the outboard portion of the assembly.

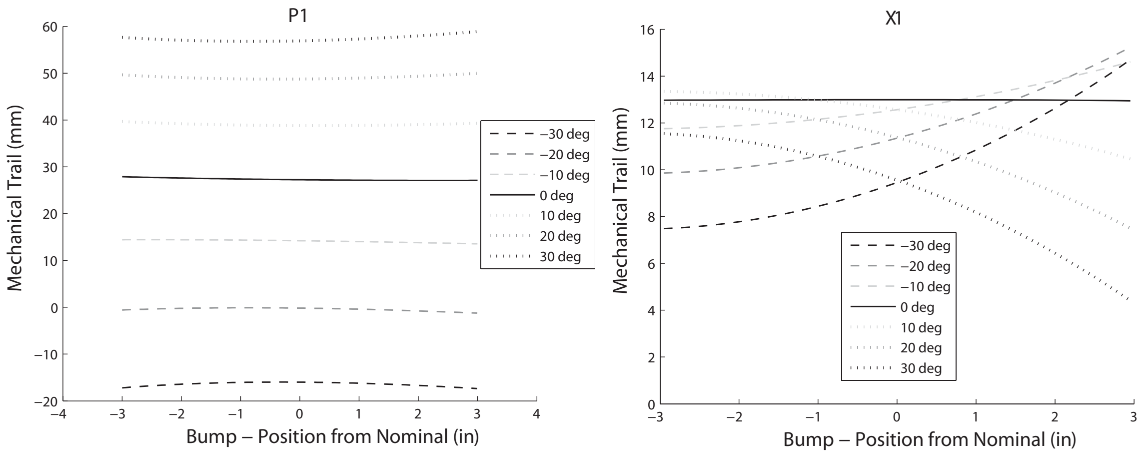

Figure 5.11: *Mechanical Trail Change in Bump for Various Steering Angles*

Table 5.2 tabulates the final values for X1's suspension parameters along with values from the 1997 Corvette C5, and P1. While X1's parameters differ from the other specific examples, and are outside the typical ranges, none of the values fall outside the full range of what is seen in production cars.

Table 5.2: X1 Suspension Parameter Comparison

Parameters at Zero Steer		Typical Values	1997 Corvette C5 [20]	P1 Design	X1 Design
Wheel Radius	mm	300 to 350	325	320	330
Caster Angle	degrees	4 to 7	6.5	5.5	2.2
Kingpin Angle	degrees	7 to 15	8.8	13.2	0
Scrub Radius	mm	-75 to 75	12	50.5	0
Mechanical Trail	mm	15 to 50	36	28	13

5.5 Verifying the Suspension Design with Experimental Data

The following data from X1 serves as a proof of concept for the suggested suspension geometry. If the suspension is eliminating extraneous torques from the steer-axis

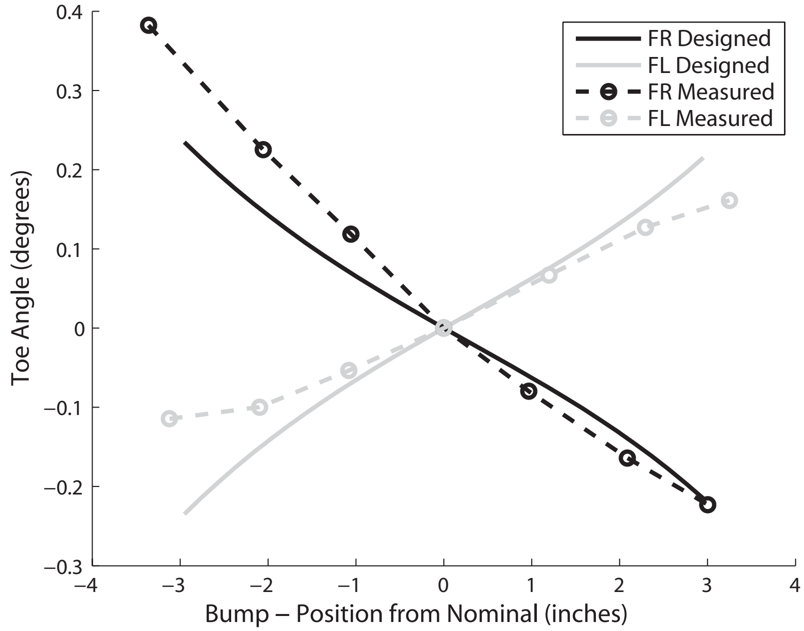

Figure 5.12: *Experimental Bumpsteer Results for X1*

reaction torque properly, reading data from the load cells in the tierod should give a nearly direct estimate of the aligning moment. In order to test the success of the suspension design, the data from each front load cell (converted into a torque about the steering axis) should match an estimated aligning moment for a quasi-steady-state maneuver with no steering dynamics.

5.5.1 Calculating the Aligning Torque for Design Validation

While the models of Chapter 2 are detailed enough to capture the dynamics for the envelope controller, there are a few necessary additions when considering the torques acting on each individual wheel. Equation 5.16 gives the estimated aligning moment, which should match the load cell measurements for the purposes of validation. The mechanical trail, pneumatic trail, and lateral force for each specific wheel are needed to solve this equation. The mechanical trail for X1 is nearly constant with steering, modeled as in Figure 5.10. The linear model of pneumatic trail from Equation 5.6

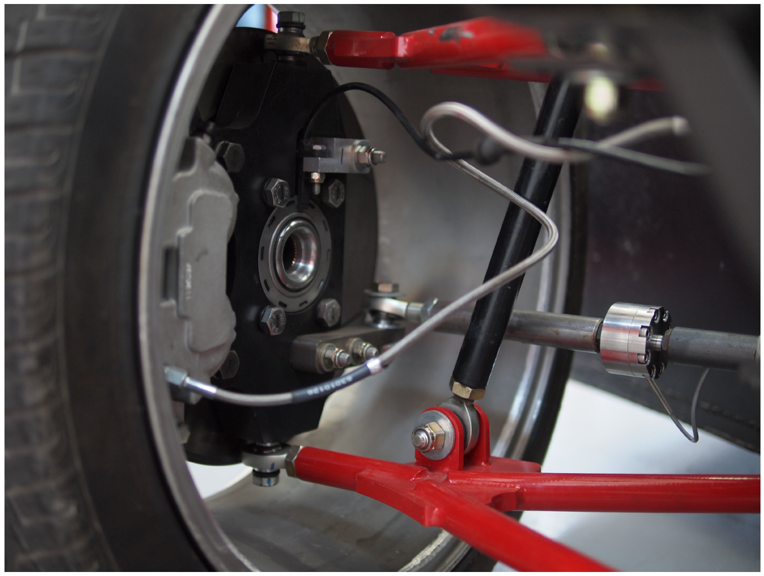

(a)

(b)

Figure 5.13: *X1's Double Wishbone Suspension, (a) Inside View of the Front Right Wheel, (b) Inside View of the Rear Right Wheel*

shows how the pneumatic trail changes with slip angle, assuming the friction coefficient is known. The lateral brush tire model determines the lateral force on a given wheel; however, for large steering angles it is not precise enough to assume the left and right slip angles are equal, or that there is no lateral weight transfer. The equations for separate left and right front slip angles are as follows, where t_f is the front track width from Figure 2.1:

$$\alpha_{fl} = \arctan\left(\frac{\beta V_x + ar}{V_x - r\frac{t_f}{2}}\right) - \delta_{fl} \tag{5.23}$$

$$\alpha_{fr} = \arctan\left(\frac{\beta V_x + ar}{V_x + r\frac{t_f}{2}}\right) - \delta_{fr} \tag{5.24}$$

The tire force for each wheel is found using the brush model of Equation 2.15, assuming half of the axle cornering stiffness C_α for each wheel, and a normal force F_z that takes into account lateral weight transfer. A simple, steady-state model for weight transfer on the front axle is determined by the nominal weight on each wheel, the vehicle roll angle ϕ (measured here using the GPS-INS system), and the steady-state lateral acceleration $V_x r$, where $K_{\phi F}$ is the front axle roll stiffness, and h_f is the front roll center height (determined by the suspension geometry):

$$F_{zfl} = \frac{bmg}{2(a+b)} - \frac{1}{t_f}\left(K_{\phi F}\phi + \frac{bmgh_f}{L}\left(\frac{V_x r}{g}\right)\right) \tag{5.25}$$

$$F_{zfr} = \frac{bmg}{2(a+b)} + \frac{1}{t_f}\left(K_{\phi F}\phi + \frac{bmgh_f}{L}\left(\frac{V_x r}{g}\right)\right) \tag{5.26}$$

For X1, $t_f = 1.625m$, $K_{\phi F} = 50000 Nm/rad$ and $h_f = 0.086m$.

The last piece of information needed to calculate the expected aligning moment is the friction coefficient. Since this is only needed for validation, the friction can be determined from the validation dataset a posteriori. The driving surface for the validation data is concrete, with an expected coefficient of friction close to 1. A quasi steady-state maneuver, like a constant steer angle, increasing speed test, provides enough lateral excitation to construct an experimental tire curve of slip angle versus lateral force. Fitting the lateral brush tire model to this curve then provides an estimate of the friction and tire cornering stiffness. The experimental estimate of tire force comes from a steady state assumption, where F_{zf} is the nominal front axle normal force:

$$F_{yf} = \frac{V_x r F_{zf}}{g} \tag{5.27}$$

Figure 5.14 gives an example of the experimental tire curve and model fit for a constant steer angle, increasing speed maneuver. The measured friction value is $\mu_f = 1$ with a front axle cornering stiffness of $C_\alpha = 115KN/rad$.

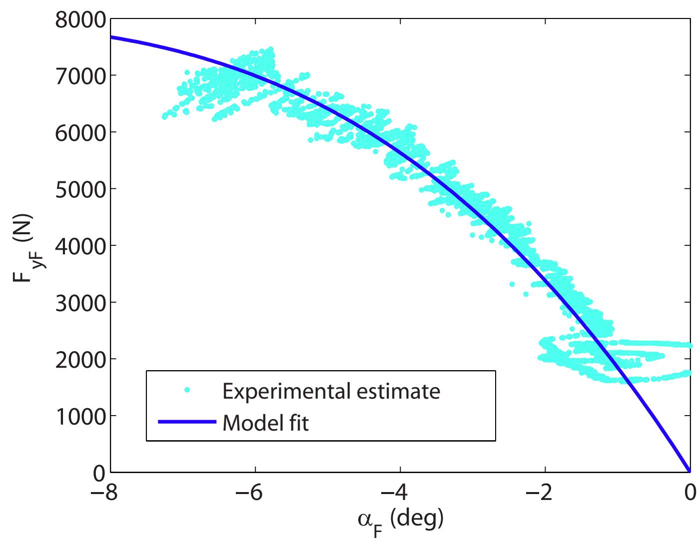

Figure 5.14: *Experimental Tire Curve and Model Fit for the Front Axle*

5.5.2 Validating the Measured Steer-Axis Reaction Torque

The total torque about X1's steering axis (translated from a measured force at the load cell using the analysis of Section 5.2) should match the aligning torque estimate of the previous section if the jacking torque and scrub radius torque have been successfully removed by the suspension kinematics. While normally the steering dynamics must also be taken into account, during the validation test the steering angle is constant, so there are virtually no torques associated with steering dynamics in this case.

Figure 5.15 shows the relevant vehicle states for the maneuver. The steering angle holds constant near $\delta = -17°$. The vehicle speed V_x ramps up slowly to approximate steady-state conditions. The yaw rate r and sideslip β grow as expected until the maximum lateral acceleration a_y is achieved near 0.8g. The plot also shows roll angle ϕ to elucidate the effect of lateral weight transfer.

The measured steering torque and a comparison to the calculated aligning moment for the front, left wheel is shown in Figure 5.16. The two match very closely, indicating that the measurements from the load cell are a good fit to the aligning moment. In this case, the front left wheel is the outside wheel in the turn, which has a higher normal load due to weight transfer. Figure 5.17 illustrates similar data for the front, right wheel, which has a much lower normal load. The decreased load on the inside wheel causes it to saturate much earlier, which is indicated by the pneumatic trail decreasing to zero. Figure 5.18 shows the right pneumatic trail decreasing to zero as the tire saturates, while the left pneumatic trail stays more constant due to the availability of more force as the roll angle increases. The same plot further indicates the constant nature of the mechanical trail on both wheels.

The agreement between the load cell measurements and the modeled aligning moment suggests that the suspension geometry does eliminate the contributions from undesirable torques. The load cell measurements directly provide a real-time estimate of pneumatic trail, and thus the coefficient of friction at each wheel. For a production system, torque or current measurements from the EPS or Active Steering system can supply the same information. With a reorientation of the steering axis, specified through the kingpin angle, scrub radius, caster angle, and mechanical trail, complexity and error in the friction estimation is decreased, allowing the vehicle envelope boundaries to be easily redefined at every time step.

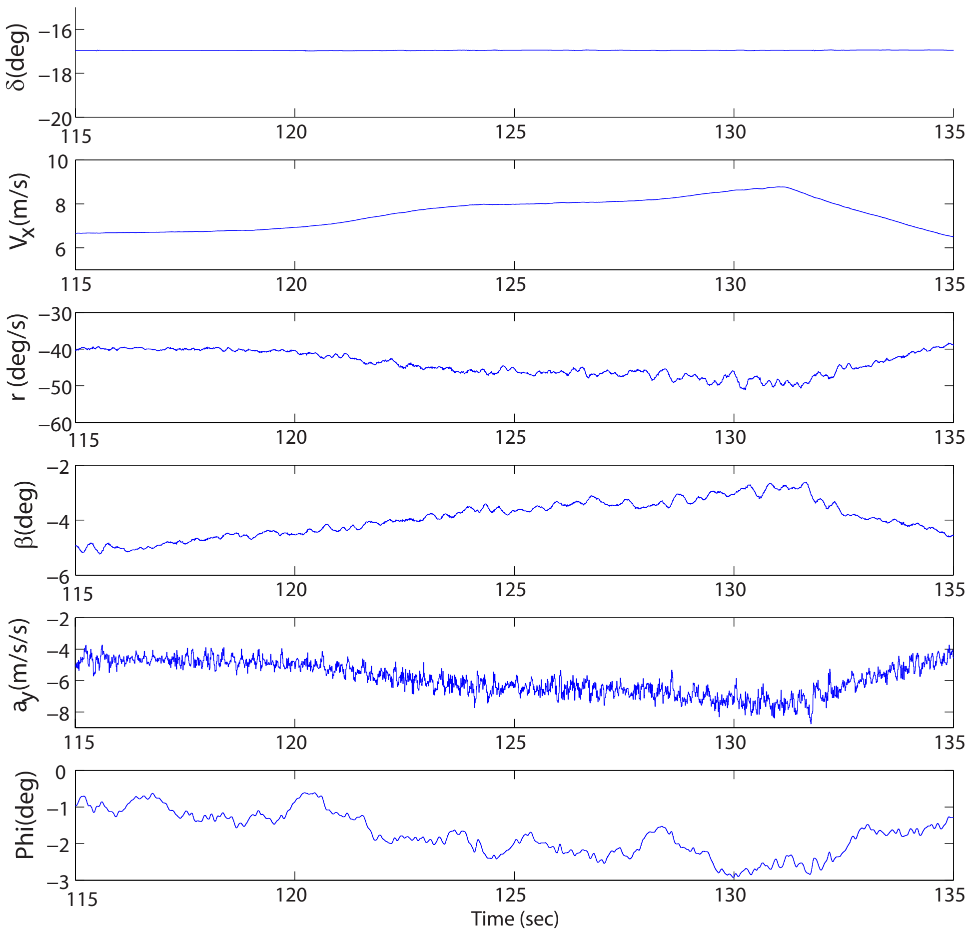

Figure 5.15: *X1 Vehicle States for a Constant Steer, Increasing Speed Test on Concrete*

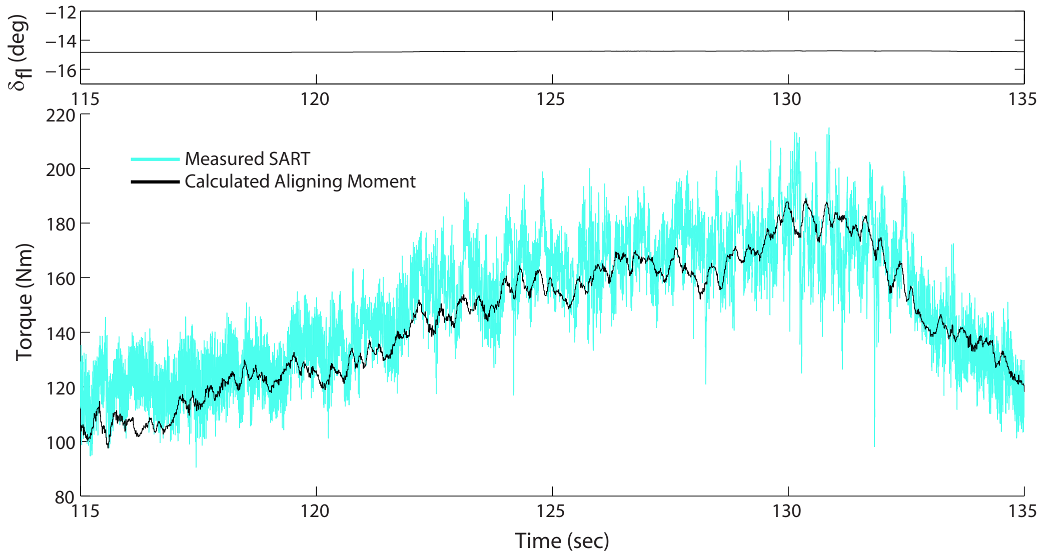

Figure 5.16: *Front Left Steer-Axis Reaction Torque Compared to a Model of Aligning Torque*

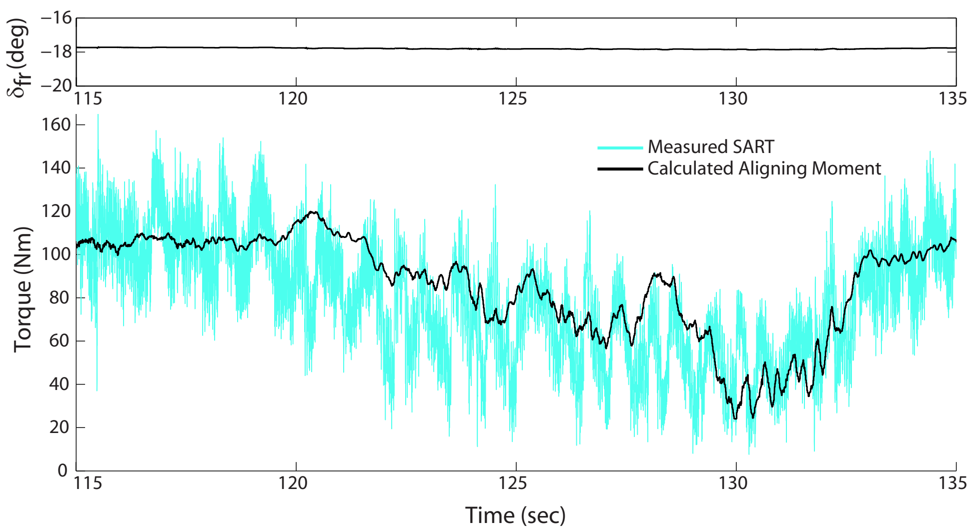

Figure 5.17: *Front Right Steer-Axis Reaction Torque Compared to a Model of Aligning Torque*

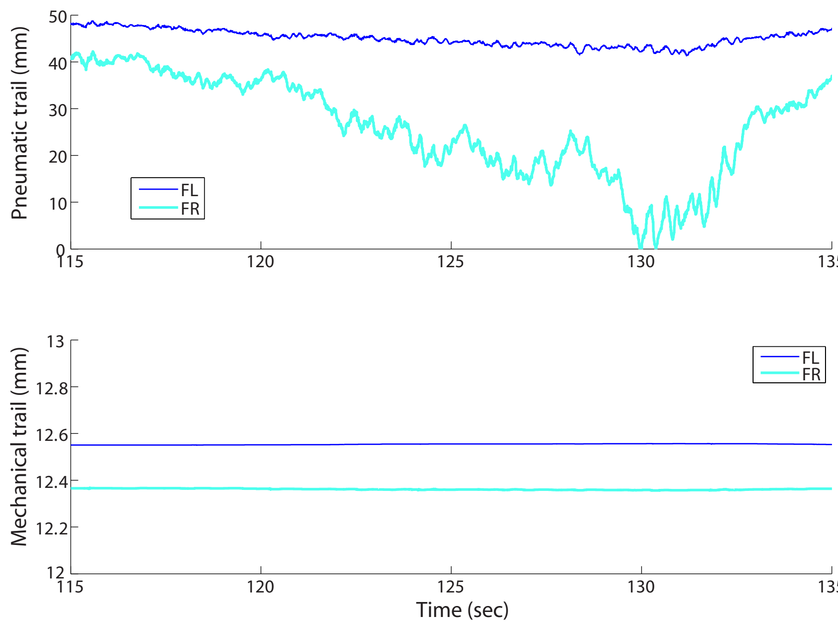

Figure 5.18: *Experimental Pneumatic and Mechanical Trail Estimates for a Constant Steer, Increasing Speed Test on Concrete*

Chapter 6

Conclusion

The future of vehicle control lies in a comprehensive control scheme that includes both consistency in the control design and cooperation between the controller and mechanical systems of the car. This dissertation proposes initial building blocks for such a vehicle. Vehicle envelope control serves as a basis for a full vehicle control system, where the vehicle envelope consists of the vehicle motion states – yaw rate and sideslip – and the purpose of the controller is to limit the vehicle states to a safe and stable envelope within the state space. Additionally, a design for suspension kinematics to enhance tire-road friction estimation serves as an example of the controller's potential interaction with mechanical systems in the vehicle.

Understanding the open loop dynamics related to lateral stability aids in the choice of a safe operating envelope for the vehicle. By studying the yaw rate and sideslip trajectories in the phase plane, it is apparent that there are regions of instability for all combinations of yaw rate and sideslip where the sideslip is larger in magnitude than the saddle equilibria sideslip and the yaw rate lies above the maximum steady state yaw rate. Additionally, for a given friction and speed, a steering angle exists above which the planar dynamics are globally unstable.

The yaw acceleration isoclines, or lines of constant yaw acceleration, define the movement of stable and unstable equilibria in the phase plane. Understanding the motion of these isoclines, especially the nullcline (the line of zero yaw acceleration, on which the equilibria lie), allows for the definition of an envelope shape that is consistent with the natural vehicle dynamics. An envelope bounded by the yaw acceleration nullcline at the maximum stable steering angle and the lines of maximum rear slip angle is one such choice. These bounds prevent saturation of the rear tires and growth of the yaw rate above what remains stable in open loop.

An attractive envelope control scheme enforces the vehicle envelope, and activates as the vehicle states exit the envelope boundaries. The controller limits the vehicle trajectory to dynamics comprised of a linear combination of the vehicle state errors in relation to the closest point on the envelope boundary. An inner boundary proportional controller that limits the driver's steering angle to the maximum stable steering angle enforces a soft landing at the boundary. This controller concept has proven successful through experiments on a steer-by-wire vehicle testbed.

Clever mechanical design can increase the effectiveness of a full vehicle control scheme like envelope control; suspension design to enhance friction estimation is one example. Many friction estimation schemes utilize the information encoded in aligning torque, the torque about the steering axis due to lateral tire forces. With typical suspensions, the steering axis also sees torque components from longitudinal and normal forces; however, these components can be eliminated through suspension geometry design. By decreasing the scrub radius and kingpin angle to zero, and reducing mechanical trail change with steering, the ability to measure aligning torque directly becomes more feasible. The suggested changes to suspension geometry do not lie outside the parameters currently seen in production vehicles today, making the design practical.

6.1 Future Work

The simplicity and success of the envelope control scheme presented in this thesis lends itself to further expansion in a variety of ways. The first is in the combination of the controller with friction estimation using X1's suspension design. Additional suggestions, explained in detail below, heighten the capabilities and effectiveness of the envelope control structure.

6.1.1 Integration of Envelope Control with Mechanically-Enhanced Friction Estimation

The ability to estimate friction in real-time is one of the most practical improvements to the envelope control scheme. By utilizing the suspension design paradigm suggested in this thesis to mechanically enhance the estimation of friction coefficient, that improvement becomes less cumbersome. Real-time friction estimation allows for constant updates to the shape of the yaw rate and sideslip envelope, increasing the ability of the controller to take timely action for stabilization.

6.1.2 Vehicle Envelope Control with Multiple Actuators

Although the envelope controller was designed for use with steer-by-wire as actuation, the control scheme is general enough to work with a variety of actuators, as long as they provide enough authority to drive the attractive manifold to zero. Modern production cars are all equipped with electronic braking capability through the ABS and ESC systems, so braking actuation is an obvious possible choice. The ability to control torque vectoring at the wheels could also provide advantages for stabilization.

Flexibility for control comes with the use of multiple actuators, such as combined braking and steering. Since each actuator contributes differently to the state trajectories, each may excel in distinct regions of the state space. Using multiple actuators does require thought as to how the controller should delegate authority.

6.1.3 Communication Between the Driver and Controller

As presented, the envelope controller does not have direct communication with the driver in the event that it takes over control of the car. Because of this, a situation could arise in which the vehicle does something that the driver does not expect. Although it is difficult to fully predict the effect of additional human-machine interaction, there are possibilities that hold promise. P1 and X1, alongside some vehicles equipped with Electronic Power Steering, have the capability of feeding back torque to the driver through the steering wheel. By providing the driver a torque that prevents him or her from steering in a way that will cause the envelope control to activate (by limiting the driver to the maximum stable steering angle, perhaps), or a torque that gets heavier the further the vehicle gets outside the boundaries, the vehicle can communicate what it is attempting to achieve through control activation.

6.1.4 Expanding the Number of States in the Vehicle Envelope

The use of attractive control to enforce the vehicle envelope makes it fairly simple to increase the number of states in the envelope without significantly increasing the computational complexity of the controller. From a controls standpoint, additional state errors could be added to the original construct of S (which includes errors in yaw rate and sideslip), or could be controlled through a separate surface. One of the most intriguing possibilities for expansion is the inclusion of an environmental envelope, whose purpose would be to prevent the vehicle from colliding with moving or stationary obstacles. With this addition, the vehicle would provide both stabilization and accident avoidance capabilities. Other potential envelope states include the roll angle and roll rate, which would aid in the prevention of rollover, and tire slip, to prevent the saturation of any individual wheel.

Bibliography

[1] Federal Motor Vehicle Safety Standards: Electronic Stability Control Systems, Controls and Displays.

[2] Masato Abe, Yoshio Kano, Kazuasa Suzuki, Yasuji Shibahata, and Yoshimi Furukawa. Side-slip Control to Stabilize Vehicle Lateral Motion by Direct Yaw Moment. *JSAE Review*, 2001.

[3] Juergen Ackermann. Robust control prevents car skidding. *IEEE Control Systems Magazine*, 17, Issue 3:23–31, 1997.

[4] Changsun Ahn, Huei Peng, and H. Eric Tseng. Estimation of Road Friction for Enhanced Active Safety Systems: Algebraic Approach. In *Proceedings of the 2009 American Control Conference, St. Louis*, 2009.

[5] Changsun Ahn, Huei Peng, and H. Eric Tseng. Robust Estimation of Road Friction Coefficient. In *Proceedings of the 2011 American Control Conference, San Francisco*, 2011.

[6] Craig E. Beal. *Applications of Model Predictive Control to Vehicle Dynamics for Active Safety and Stability*. PhD thesis, Stanford University, 2011.

[7] Craig E. Beal, Carrie G. Bobier, and J. Christian Gerdes. Controlling Vehicle Instability Through Stable Handling Envelopes. In *Proceedings of the 2011 Dynamic Systems and Control Conference, Arlington*, 2011.

[8] Andre Benine-Neto, Stefano Scalzi, Mariana Netto, Said Mammar, and William Pasillas-Lepine. Vehicle Yaw Rate Control Based on Piecewise Affine Regions. In *Proceedings of the 2010 IEEE Intelligent Vehicles Symposium, San Diego*, 2010.

[9] David M. Bevly, Robert Sheridan, and J. Christian Gerdes. Integrating INS Sensors with GPS Velocity Measurements for Continuous Estimation of Vehicle Sideslip and Tire Comering Stiffness. In *Proceedings of the 2001 American Control Conference (ACC), Arlington*, 2001.

[10] John Thomas Cameron. *Vehicle Dynamic Modeling for the Prediction and Prevention of Vehicle Rollover*. PhD thesis, Pennsylvania State University, 2005.

[11] Wanki Cho, Jangyeol Yoon, Jeongtae Kim, Jaewoong Hur, and Kyongsu Yi. An Investigation into Unified Chassis Control Scheme for Optimised Vehicle Stability and Manoeuvrability. *Vehicle System Dynamics: International Journal of Vehicle Mechanics and Mobility*, 46:S1:87–105, 2008.

[12] Taeyoung Chung and Kyongsu Yi. Design and Evaluation of Side Slip Angle-Based Vehicle Stability Control Scheme on a Virtual Test Track. *IEEE Transactions on Control Systems Technology*, 14, No. 2:224–234, 2006.

[13] Jennifer N. Dang. Statistical Analysis of the Effectiveness of Electronic Stability Control Systems. Technical report, National Highway Traffic Safety Administration (NHTSA), July 2007. DOT HS 810 794.

[14] Development Data Group. 2007 World Development Indicators. Technical report, The World Bank, 2007.

[15] Development Data Group. 2008 World Development Indicators. Technical report, The World Bank, 2008.

[16] John C. Dixon. *Tires, Suspension and Handling.* Society of Automotive Engineers, Warrendale, PA, 1996.

[17] Howard Dugoff, P. S. Fancher, and Leonard Segel. An analysis of tire traction properties and their influence on vehicle dynamic performance. 1970. SAE Paper No. 700377.

[18] Masaya Endo, Kenji Ogawa, and Masahiko Kurishige. Cooperative Control of Active Front Steering and Electric Power Steering Based on Self-Aligning Torque. In *Proceedings of the International Symposium on Advanced Vehicle Control (AVEC), Taipei, Taiwan*, 2006.

[19] Insurance Institute for Highway Safety. www.iihs.org. ESC and how it helps drivers maintain control, 2012.

[20] Steven P. Fuja, Henry A. Schmid, and Joseph P. Ryan. Synthesis of Chassis Parameters for Ride and Handling on the 1997 Chevrolet Corvette. In *Racing Chassis and Suspension Design*. Carroll Smith, SAE, Warrendale, PA, 2004.

[21] Michael Gipser. FTire: A Physically Based Application-oriented Tyre Model for Use with Detailed MBS and Finite-element Suspension Models. *Vehicle System Dynamics*, 43:76–91, 2005.

[22] Junjie He, David A. Crolla, Martin C. Levesley, and Warren J. Manning. Integrated Active Steering and Variable Torque Distribution Control for Improving Vehicle Handling and Stability. Technical report, SAE Technical Paper 2004-01-1071, 2004.

[23] Robert C. Hoffman, Jeffrey L. Stein, Loucas S. Louca, and Kunsoo Huh. Using the Milliken Moment Method and Dynamic Simulation to Evaluate Vehicle Stability and Controllability. *International Journal of Vehicle Design*, 48:132–148, 2008.

[24] Daegun Hong, Inyong Hwang, Paljoo Yoon, and Kunsoo Huh. Development of a Vehicle Stability Control System Using Brake-by-Wire Actuators. *ASME Journal of Dynamic Systems, Measurement, and Control*, 130, 2008.

[25] Y.H. Judy Hsu. *Estimation and Control of Lateral Tire Forces Using Steering Torque*. PhD thesis, Stanford University, 2009.

[26] Y.H. Judy Hsu and J. Christian Gerdes. The Predictive Nature of Pneumatic Trail: Tire Slip Angle and Peak Force Estimation using Steering Torque. In *Proceedings of the International Symposium on Advanced Vehicle Control, Kobe*, 2008.

[27] Y.H. Judy Hsu and J. Christian Gerdes. Envelope Control: Keeping the Vehicle Within its Handling Limits Using Front Steering. In *Proceedings of the 21st International Symposium on Dynamics of Vehicles on Roads and Tracks*, 2009.

[28] Y.H. Judy Hsu, S.M. Laws, and J.C. Gerdes. Estimation of Tire Slip Angle and Friction Limits Using Steering Torque. *IEEE Transactions on Control Systems Technology*, 18, Issue 4:896–907, 2010.

[29] S. Inagaki, I. Kshiro, and M. Yamamoto. Analysis on Vehicle Stability in Critical Cornering Using Phase-Plane Method. In *Proceedings of the International Symposium on Advanced Vehicle Control, Tsukuba-shi*, 1994.

[30] Matthijs Klomp. *Longitudinal Force Distribution and Road Vehicle Handling.* PhD thesis, Chalmers University of Technology, 2010.

[31] W. Kramer and M. Hackl. Potential functions and benefits of electronic steering assistance. In *Proceedings of FISITA96 World Congress, Prague*, 1996.

[32] Shad Laws, Christopher Gadda, Scott Kohn, Paul Yih, J. Christian Gerdes, and J. Craig Milroy. Steer-By-Wire Suspension and Steering Design for Controllability and Observability. In *IFAC World Congress, Prague, Czech Republic*, 2005.

[33] Shad Laws and J. Christian Gerdes. High-Frequency Vehicle Characteristics: Modeling and Experimental Validation of Yaw, Sideslip, and Roll Modes. In *Proceedings of the International Symposium on Advanced Vehicle Control, Taiwan*, 2006.

[34] Heinz Leffler, Reinhard Auffhammer, Reent Heyken, and Harald Roeth. New Driving Stability Control System with Reduced Technical Effort for Compact and Medium Class Passenger Cars. Technical report, SAE Technical Paper 980234, 1998.

[35] E. K. Liebemann, K. Meder, J. Schuh, and G. Nenninger. Safety and Performance Enhancement: The Bosch Electronic Stability Control (ESP). Technical report, SAE Technical Paper No. 2004-21-0060, 2004.

[36] W.J. Manning and D.A. Crolla. A Review of Yaw Rate and Sideslip Controllers for Passenger Vehicles. *Transactions of the Institute of Measurement and Control*, 29(2):117–135, 2007.

[37] William F. Milliken and Douglas L. Milliken. *Race Car Vehicle Dynamics*. SAE International No. R-146, 1995.

[38] NHTSA. Traffic Safety Facts 2009: A Compilation of Motor Vehicle Crash Data from the Fatality Analysis Reporting System and the General Estimates System. Technical report, U.S. Department of Transportation, 2009.

[39] David M. North. Finding Common Ground In Envelope Protection Systems. *Aviation Week & Space Technology*, 153(9):66, August 2000.

[40] Eiichi Ono, Kenji Asano, and Ken Koibuchi. Estimation of Tire Grip Margin Using Electric Power Steering System. In *Proceedings of the 18th International Association for Vehicle System Dynamics (IAVSD) Symposium, Kanagawa, Japan*, 2003.

[41] Eiichi Ono, Shigeyuki Hosoe, Hoang Tuan, and Shun'ichi Doi. Bifurcation in vehicle dynamics and robust front wheel steering control. *IEEE Transactions on Control Systems Technology*, 6:412–420, 1998.

[42] Hans B. Pacejka. *Tire and Vehicle Dynamics*. Society of Automotive Engineers, Inc, Warrendale, PA, 2002.

[43] Hans B. Pacejka and Egbert Bakker. The Magic Formula Tyre Model. *Vehicle System Dynamics*, 21:1–18, 1992.

[44] Wim R. Pasterkamp and Hans B. Pacejka. Application of Neural Networks in the Estimation of Tire/Road Friction Using the Tire as Sensor. *SAE Paper No. 971122*, 1997.

[45] Eric J. Rossetter, Joshua P. Switkes, and J. Christian Gerdes. Experimental Validation of the Potential Field Lanekeeping System. *International Journal of Automotive Technology*, 5(2):95–108, 2004.

[46] Hiroki Sato, Hiroyuki Kawai, Masaru Isikawa, Hitosi Iwata, and Shin Koike. Development of Four Wheel Steering System Using Yaw Rate Feedback Control. Technical report, SAE Technical Paper 911922, 1991.

[47] Hendrikus Theodoras Smakman. *Functional Integration of Slip Control with Active Suspension for Improved Lateral Vehicle Dynamics*. PhD thesis, Technische Universiteit Delft, 2000.

[48] Henk Smakman. Functional Integration of Active Suspension with Slip Control for Improved Lateral Vehicle Dynamics. In *Proceedings of the 5th International Symposium on Advanced Vehicle Control, Ann Arbor*, 2000.

[49] Hongtei Eric Tseng, Behrouz Ashrafi, Dinu Madau, Todd Allen Brown, and Darrel Recker. The Development of Vehicle Stability Control at Ford. *IEEE/ASME Transactions on Mechatronics*, 4, No. 3:223–234, 1999.

[50] Koji Uematsu and J. Christian Gerdes. A Comparison of Several Sliding Surfaces for Stability Control. In *Proceedings of the International Symposium on Advanced Vehicle Control, Japan*, number 20024578, 2002.

[51] Anton T. van Zanten, Rainer Erhardt, and Georg Pfaff. VDC, The Vehicle Dynamics Control System of Bosch. Technical report, SAE Technical Paper 950759, 1995.

[52] Anton T. van Zanten, Rainer Erhardt, Georg Pfaff, Friedrich Kost, Uwe Hartmann, and Thomas Ehret. Control Aspects of the Bosch-VDC. In *International Symposium on Advanced Vehicle Control (AVEC), Aachen University of Technology, Germany*, pages 573–608, 1996.

[53] Miguel A. Vilaplana, Douglas J. Leith, William E. Leithead, and Jens Kalkkuhl. Control of Sideslip and Yaw Rate in Cars Equipped with 4-Wheel Steer-by-Wire. Technical report, SAE Technical Paper 2004-01-2076, 2004.

[54] M. Mitchell Waldrop. Flying the Electric Skies. *Science*, 244, No. 4912:1532–1534, 1989.

[55] Junmin Wang and Raul G. Longoria. Coordinated Vehicle Dynamics Control with Control Distribution. In *Proceedings of the 2006 American Control Conference, Minneapolis, Minnesota*, 2006.

[56] Klaus H. Well. Aircraft Control Laws for Envelope Protection. In *AIAA Guidance, Navigation, and Control Conference*, 2006. AIAA 2006-6055.

[57] J.C. Whitehead. Four Wheel Steering: Maneuverability and High Speed Stabilization. Technical report, SAE Technical Paper 880642, 1988. Detroit, MI.

[58] Yoshiyuki Yasui, Wataru Tanaka, Yuji Muragishi, Eiichi Ono, Minekazu Momiyama, Hiroaki Katoh, Hiroaki Aizawa, and Yuzo Imoto. Estimation of Lateral Grip Margin Based on Self-Aligning Torque for Vehicle Dynamics Enhancement. Technical report, SAE Paper No. 2004-01-1070, 2004.

[59] Yoshiyuki Yasui, Kenji Tozu, Noriaki Hattori, and Masakazu Sugisawa. Improvement of Vehicle Directional Stability for Transient Steering Maneuvers Using Active Brake Control. Technical report, SAE Technical Paper Series No. 960485, 1996.

[60] Paul Yih. *Steer-by-Wire: Implications for Vehicle Handling and Safety*. PhD thesis, Stanford University, 2005.

[61] Tohru Yoshioka, Tomohiko Adachi, Tetsuro Butsuen, Haruki Okazaki, and Hirotaka Mochizuki. Application of sliding-mode theory to direct yaw-moment control. *JSAE Review*, 20:523–529, 1999.